Doctoral Thesis

In Situ Transmission Electron Microscopy Study for Electrical, Thermal and Mechanical Behaviors of Low Dimensional Materials

Kangsik Kim

Department of Materials Science and Engineering

Graduate School of UNIST

2019

In Situ Transmission Electron Microscopy Study for Electrical, Thermal and Mechanical Behaviors of Low Dimensional Materials

Kangsik Kim

Department of Materials Science and Engineering

Graduate School of UNIST

In Situ Transmission Electron Microscopy Study for Electrical, Thermal and Mechanical Behaviors of Low Dimensional Materials

A thesis/dissertation
submitted to the Graduate School of UNIST
in partial fulfillment of the
requirements for the degree of
Doctor of Philosophy

Kangsik Kim

12. 10. 2018
Approved by

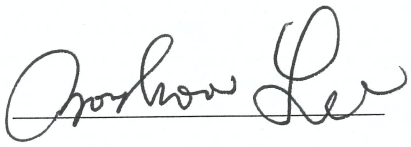

Advisor
Zonghoon Lee

In Situ Transmission Electron Microscopy Study for Electrical, Thermal and Mechanical Behaviors of Low Dimensional Materials

Kangsik Kim

This certifies that the thesis/dissertation of Kangsik Kim is approved.

12. 10. 2018

signature

Advisor: Zonghoon Lee

signature

Hyung-Joon Shin: Thesis Committee Member #1

signature

Jung-Woo Yoo: Thesis Committee Member #2

signature

Soon-Young Kwon: Thesis Committee Member #3

signature

Eui-Tae Kim: Thesis Committee Member #4

Abstract

Transmission electron microscopy (TEM) is one of microscopy techniques in which a beam of electrons is transmitted through a specimen having thin thickness to form an image and get information. TEM is a major analytical method in the physical, chemical and biological science and is additionally utilized in nanotechnology and semiconductor research. When we carried out TEM analysis, it is important to understand how and why materials change in various parameters. Beginning of understanding is the observation for behaviors of the atoms. In situ TEM can analyze the behavior of atoms and provide information about structure and properties of the materials. Due to the development for in situ TEM holders by many commercial companies, a variety of environments and variables can be controlled into TEM with high vacuum levels and TEM eventually become a very powerful tool for observing reactions at the atomic level.

Discovery of low dimensional materials is contributing to attracting special features in research filed. For example, the surface properties dominate the bulk properties, and quantum size effects are observed due to spatial constraints. Those features have shown extraordinary electronic, optical, thermal, mechanical and chemical properties, which may result in their use in wide range of nanotechnology. However, there is still lacking understanding of these various characteristics, leaving only the potential possibilities. Based on these issues, research on low dimensional materials through TEM would be essential.

In this work, in situ TEM research conducted to investigate the potential possibilities of low dimensional materials such as nanostructures, two-dimensional material through electrical, thermal and mechanical TEM holders. In the case of the electrical holder, leakage current increased in metal-insulator-metal capacitor at nanoscale due to Joule heating and induced crystallization of insulator in the capacitor when the voltage was applied. In the case of heating holder, silicon nanomembrane was used to study for the heteroepitaxial growth of beta silicon carbide due to the crystallization of hydrocarbons as a contamination. Lastly, mechanical holder utilized to study mechanical properties of exfoliated graphene and molybdenum disulfide by uniaxial tensile test in TEM. In addition, we also conducted several simulation studies to understand the behavior of these low dimensional materials in TEM. Ultimately, I will discuss how the results of in situ TEM could contribute.

Contents

List of Figures

diffractions from the nanocrystalline YSZ are very weak. But we can predict d-spacing of YSZ (111) phase through Figure 10(d). We confirm that the d-spacing of YSZ (111) phase indicated by yellow dashed line appears between the (200) and (11-1) d-spacings of Si substrate. Like the orange circle in (a), we put an objective aperture into the predicted YSZ (111) d-spacing and rotate around the central axis. (c) It is the result from the precession electron diffraction (PED), which is formed by integration over a collection of diffractions from tilted incident beams. (c) Nanocrystalline YSZ thin film, which did not appear in DP, appear here in the image. The bright regions correspond to the crystallized YSZ thin film, and ratio of the crystallized region corresponds to 46.16 % by calculation.

Figure 12. (a) A time–current graph of a bulk sample obtained using a four-point probe. At 100 s on the I–V curve, we can see that the measured current rapidly increases and we could speculate that there is a transformation in the YSZ thin film compared to the in-situ TEM results. Inset (a) shows the Ru top electrode deposited using a masking pattern in a round shape. Mask patterning deposition was performed at diameters of 100 μm. Panel (b) shows the XRD result before and after applying voltage to the MIM capacitor. We can clearly identify the difference between the before and after reflection peaks. After the voltage is applied, it is confirmed via the XRD and previous TEM results that the amorphous YSZ thin film is transformed to crystallized YSZ having cubic (111) and cubic (200) structures.

Figure 13. (a) Temperature dependence on the applied voltage and degree of crystallization of the YSZ thin films. A value of f closer to 1 indicates crystallization rather than amorphous conditions. (b) A schematic illustrating YSZ thin film biphasic crystallization. The bottom and top orange layers correspond to Ru, and the transparent middle layer corresponds to the YSZ thin film. In the YSZ thin film, the green hemispheres indicate crystallized grains.

Figure 14. (a) Schematic of steps for fabricating the Si NM and transferring to the heating device. (b-c) Optical microscope images of free-standing Si NM on SOI substrate and in situ heating device. Scale bars are 100 μm. (d) TEM and (e) DP images of free-standing Si NM. Scale bar is 1 μm.

Figure 15 (a) Cross-section TEM image of Si NM capped with SiOx. The sample is before HF vapor etching and corresponds to III in Figure 14(a). Scale bar is 2 nm. (b) Intensity profile acquired from cross-section TEM image as indicated by a red dotted line in Figure 15(a). (c) EELS results obtained from Si NM and capping oxidation. Colors of graph correspond to the cross color in Figure 15(a).

Figure 16. (a) TEM image shows the free-standing Si NM with wrinkles. Defects begin to grow around wrinkles. The scale bar is 1 μm. (d-f) As the silicon diffuses, thickness contrast appears, and it is confirmed that there is a nanostructure with specific orientation in aggregation region. The scale bars are 200 nm.

Figure 17. (a) Graph of depression for melting temperature with thickness and material constant. (b) Graph of sublimation temperature for silicon with degree of vacuum. (c-e) Ex-situ heating experiment setting under the OM. OM images of (d) before and (e) after heating Si NMs in atmosphere. The scalebar is 200μm.

Figure 18. (a) TEM image of 100 Si NM, and the lower left direction is the same as the orientation of Si NM. (b) Defects begins to progress, and outer layer peel off. (c-e) The outer layer is getting more peeled off, and that the 1D structure also grows continuously. (f) As the hole defect grows, Si evaporates but the 1D structure remains in the vacuum. The scale bar is 200 nm.

Scale bar is 2 μm. (d) HRTEM image of the edge of fractured MoS_2. Scale bar is 5 nm. (e-f) Strain mapping results for (b) through GPA method. These resulting image is taken from (b).

Figure 42. (a) SEM image of bending MoS_2 for Repetitive uniaxial testing. Controlled displacement is 600 nm. (b) The result of load-displacement for repetitive uniaxial testing. Mechanical weakening is observed as the tensile testing conducted continuously.

List of Table

Table 1. The values of thermal and electrical conductivities depend on the degrees of crystallization of the YSZ thin film. A value of f closer to 1 indicates crystallization.

Chapter 1: Introduction

It goes without saying that analysis equipment is used to investigate characterization of material. Especially, transmission electron microscopy (TEM) is one of the major microscopy techniques in which a beam of electrons is interacted with several kinds of materials. In ranges from nanomaterials to low dimensional materials, the realization of characterization is important and they often have properties differing from bulk materials has led to enormous interest to interpret physical, chemical and structural results in TEM characterization. Simply conducting the imaging and analyzing only the before and after responses to any external stimuli is not the main work in TEM anymore. For that reason, the potential for research in real time is inevitably high. Since the development of in situ TEM holder, controlling parameters have become available such as electrical, thermal and mechanical environment, and these holders have also played a major role in understanding the characteristics of nanostructure in various field of research. Thus, in situ TEM experiment is in the spotlight as a small laboratory with atomic resolution in high vacuum environment, requiring a lot of experimental design for atomic behaviors in nanostructure.

In this thesis, among many other things, I will discuss three types of in situ TEM experiments for low dimensional materials. The three types are electrical, thermal and mechanical properties, respectively. Firstly, in the case of electronic properties, there are many semiconductor devices such as metal-insulator-metal (MIM) capacitor, metal-oxide-semiconductor field-effect transistor (MOS FET), nanobattery and random access memory (RAM). Using the in situ TEM electrical testing, many articles covered with reliability and stability for the devices. For example, domain propagation and relaxation have been observed in processes of ferroelectric domain switching in $BiFeO_3$.[2] Oxygen evolution reactions at high voltage related to interfacial issues have been revealed in nanobatteries during in situ charging.[3] The switching mechanism of set and reset processes in resistive random access memory (ReRAM) stacks has also been observed under TEM analysis.[4] Even though multiple factors might contribute to the transport properties of flowing electricity to nanostructures with conductivity, the Joule heating effect at the nanoscale is one of main factors in in situ TEM for electrical characterization.[5] In contrast to typical thermal heating, Joule heating raises the temperature only in a localized region for sufficiently small cross-sectional areas, leading to large current densities.[6] In general, phase transformations of materials occur during Joule heating. For example, there has been a study on material changes in nano structures intentionally using the voltage and Joule heating was found to induce crystallization even in the bulk state.[7, 8] I will discuss the local crystallization in the MIM capacitor via Joule heating and the leakage current induced during in situ TEM biasing tests. In situ TEM experiments for electrical properties of bulk structures require very detailed experimental conditions because of these various factors. Therefore, I confirmed the effects of Joule heating which can occur in electrical experiment for TEM specimen milled by focused ion beam (FIB) milling through finite element

modeling (FEM).

The second part of this thesis is in situ TEM for thermal behavior. Long ago, through the electron beam-induced specimen heating was used, it has already been used in many fields since the past. Since the development of heating holder for TEM, many nanostructures were utilized to study growth and defect mechanism. And, the environment in TEM is similar to the thin film deposition carried in chamber because degrees of vacuum in TEM is also about 10^{-7} torr. The heating holder can control heating and quantitative analysis of heat-induced phase transformations, sublimation, melting, sintering, diffusion, recrystallization and annealing for low dimensional material. The heating holder is classified roughly into three types such as crucible, filament wire and microelectromechanical systems (MEMS) heating stage. Many pioneering researches have already proposed the growth mechanism of nanomaterials using these various heating holders. For example, Stig et al. has confirmed that reshaping of nickel nanocrystals is induced by the formation of carbon nanofibers from the decomposition of methane in nickel nanocrystals.[9] This led to the discovery of the restructuring of mono-atomic step edges on the nickel surface in graphene growth. Hong et al. also demonstrates atom-by-atom growth of Zn and O at the preferential zigzag edge of a ZnO monolayer on graphene through in situ observation.[10] It has shown that the thinnest ZnO monolayer has a wide band gap up to 4.0 eV, due to quantum confinement and graphene-like structure. As such, atomic scale research through TEM has reported many achievements in nanostructure and phenomena analysis. Here, I discuss about the deposition of thin film using MEMS heating stage. In fact, it is hard to set up the deposition condition in TEM. I developed specific Si nanomembrane (NM), which was enough to have a transmission for electron beam. The aim of this work is to study the growth mechanism of thin films deposited on Si substrate usually utilized in nanotechnology. I studied the heteroepitaxial grown (001) 3C-SiC on (001) Si NM at atomic scale in TEM. Not only experimental results, but also simulation shows the heteroepitaxial growth about (100) 3C-SiC on (100) Si NM. This work is to be a way to experiment with various heteroepitaxy techniques on Si NM in in situ TEM.

Finally, I will discuss about in situ TEM for mechanical behavior. Graphene composed of carbon and molybdenum disulfide (MoS_2) composed of molybdenum and sulfur, one kind of transition metal dichalcogenide (TMD) material, including the two-dimensional material are considered. Both are layered structures and have van der Waals (vdW) interactions between two adjacent layers. Currently, quantitative mechanical testing of various two-dimensional materials in nanoscale is conducted using atomic force microscopy (AFM) and nanoindentation.[11, 12] However, this approach, which results in highly non-uniform local strain fields in the two-dimensional membrane, has critical errors in extracting the intrinsic mechanical properties of the two-dimensional materials.[13] In order to obtain the most reliable and quantitative mechanical properties, a simple uniaxial tensile test must be performed. Several uniaxial tests in TEM have been already proposed, but they don`t show the completely clean solution to the problem for the issue in contamination during transferring the specimen. I will suggest

how to proceed by applying two innovative transfer methods, and discuss the mechanical properties depending on the structure of two dimensional materials through in situ TEM uniaxial testing.

As I mentioned above, in situ TEM experiments have the several platforms to study structural, physical and chemical changes in materials under a variety of conditions. However, even with the commercial or well-designed platforms, the expected results may vary depending on how the specimen is transferred to the stages or the design of the experiment, and several experimental arguments are considered. Of course, it may be important to get the experimental experience to reduce the mistakes one step at a time, but this would involve a lot of time and money. It takes time and effort to learn an in situ techniques and attention to detail and persistence is the key to success. In this thesis, in situ TEM studies for electrical, thermal and mechanical properties will help reduce the opportunity cost of suffering researchers.

Chapter 2. Research Background

2.1. In Situ Transmission Electron Microscopy

2.1.1. Current status and future directions

Modern TEM techniques are not simple tool depending on interpreting before and after results of imaging or spectrometry anymore. Since the development of in situ TEM techniques now days, we want to understand how and why the nanomaterials change under thermal, electrical or mechanical stimuli. Not assuming the conclusion through the beginning and ending of results, but immediately observing to study kinetics and path ways of such reactions. So, in situ TEM techniques can play a unique role, using careful experimental design of the process. As shown in Figure 1, applying in situ TEM techniques to different sections allows us to study full parameter space. In conclusion, these techniques illustrate the new knowledge that can be gained from such experiments.

Although history of in situ TEM is not long, it has already summarized in many literatures well. Traditionally, there are two environmental issues of how to improve the degrees of vacuum equivalent to 10^{-7} torr and how to envelop the gas or liquid state in TEM while reducing contamination. In addition, what has always been a problem in in situ TEM research is drift, contamination and alteration with straining or heating for irradiation of electron beam. Despite these problems, the researches previously focused on increasing the spatial resolution and maintaining a clean environment. But now that are focusing on how to catch the changes to some external stimulus. We would certainly be able to extract data from whatever about stimulus. Ultimately, our biggest challenge would be to use the aberration correction and become understanding the data to solve problems without loss of resolution.

Currently there are many approaches in the in situ TEM researches, among which one approach is to integrate several variables. We many want to strain the TEM specimen while heating it. In addition to integrating these variables, we will also have to consider how we can quickly get information about our response. To reduce experimental errors, slowing down the reaction while adjusting the various variables freely. We want to get a solution ‘How does the material change over time?’ through post analysis and statics. Meaning of post analysis is what happened during a reaction of process by comparing the initial and final states. Of course, real time observation is the most powerful tool to study some phenomena. But, in some cases, post analysis may be necessary. The reactive experiment in in situ TEM may not be able to give us a complete analysis, so the case of chemical analysis must be done through post-analysis. Other important things are reproducibility and repeatability of in situ TEM experiments. That is so important to spend time with our experimental design so that we don't end up repeating all hard work to confirm interpretation. Repeated efforts will remain legacy. Because the experiments can be carried out with the accumulated knowledge in this way, we don't take a mistake to

introduce artifacts that will affect in situ experiments, otherwise we are only considering artifacts in TEM specimen preparation. There are many blind spots in the TEM specimen preparation, but in the case of FIB or ion milling, there may be effects on the measured results as the ions are implanted. The reasons for this issues is also to be confirmed through TEM analysis, and the control for variable should also be done through statistics.

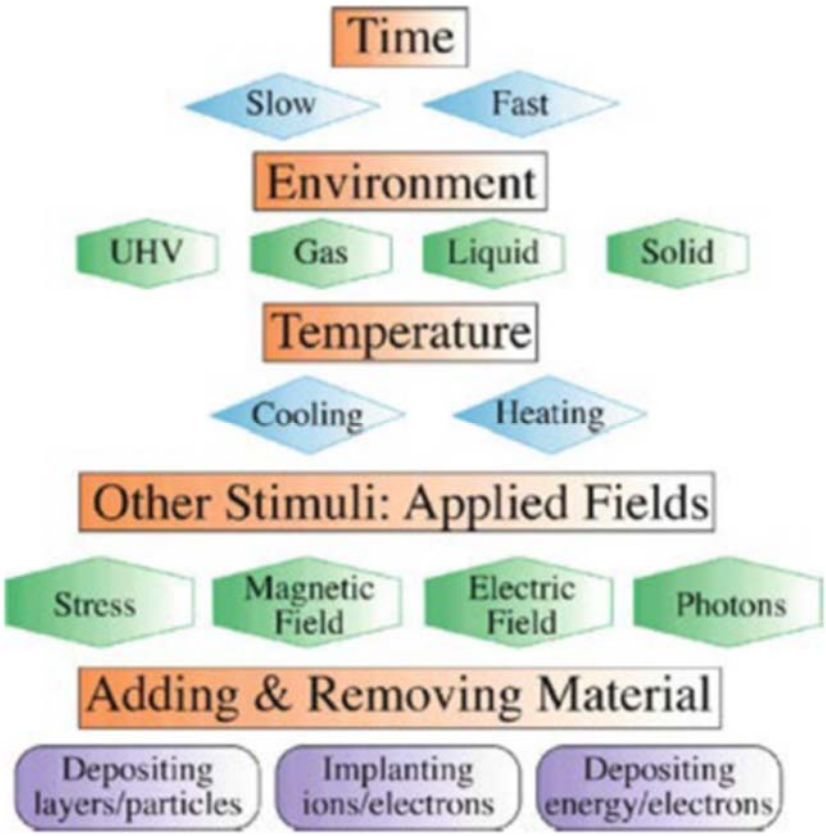

Figure 1. Schematic diagram of different in situ TEM techniques.[1]

2.1.2. In situ TEM holders

Special holders have been developed that allow us to change TEM specimen while we observe it in the TEM. In other words, we do experiments on a specimen in TEM such as heat, cool, strain, twist or compress. Most of the microscope manufactures are producing their own line of holders but there are also dedicated holder manufacturers such as Hummingbird, Protochips, Bruker and DENS solutions.[14-17] The holders made by each company have different forms due to the influence of the patent, but they have common parts in operating experiments. Above I mentioned, I will describe the tree types of in situ TEM experiments for electrical, thermal and mechanical behaviors. Before that, in this chapter, I will briefly introduce the in situ TEM holders.

In situ TEM electrical measurements are divided into two types as shown in Figure 2. Metal tip fabricated by electrochemical etching or commercial MEMS device is utilized to contact to induce electric field. Each type has advantages and disadvantages for users to handle the experiment. Simply considering management, commercial MEMS device is inevitably easy to use. But we should remind that the more we are comfortable, the more expensive it becomes. In case of contacting metal tip or attaching the target to tip before inserting holder, it has an advantage to get the small interested region. Because the very thin tip is utilized, it is chance to directly observe the change in the contact part. That is breakthrough in how we can extend dynamics research to atomic levels. However, we may be comfortable when using a MEMS device, but we may have a relatively large field of view. Also, the specimen is connected through the electrodes on the MEMS device and the contact resistance between the electrode and the target is considered. Nevertheless, it is very important because MEMS device forms a very similar experimental design to the industrial field, which is the main reason for studying electrical characteristics. And, while considering the parameters of not only the holder type but also the nanomaterials, the influence of Joule heating on the current flowing and transmission of electron beam should be considered.

In situ TEM heating holder can be raised temperature up to 1300 ˚C within milliseconds, and the temperature is calibrated by the supplier with a chip-specific calibration file. Heating holder composed of tantalum due to the high melting temperature and structural stability during thermal cycling. Most heating holders utilize MEMS device that resistive heating like an electric fire is the reason of raising the temperature as shown in Figure 3. Otherwise filament wire heating stage is known. When the MEMS device is used in heating experiments, thin films or nanomembranes, which is a two-dimensional material, is utilized, so the tearing or thermal expansion must be considered. If the TEM specimen is in the form of nanoparticles or powders, it may be wise to use the type of filament wire heating stage. It is reported that not only the space efficiency is high but also it can be used up to 2000 ˚C which is very high temperature. Therefore, by setting the gas injector beside filament, not only heating but also the

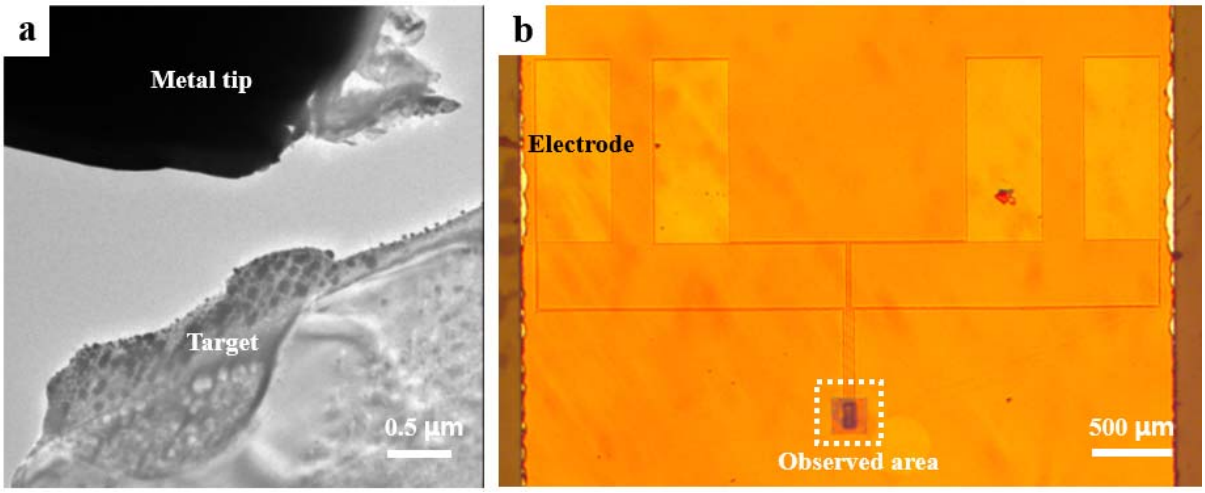

Figure 2. Two types of in situ TEM electrical measurement. (a) Contacting metal tip (b) Commercial MEMS device made in Protochips.

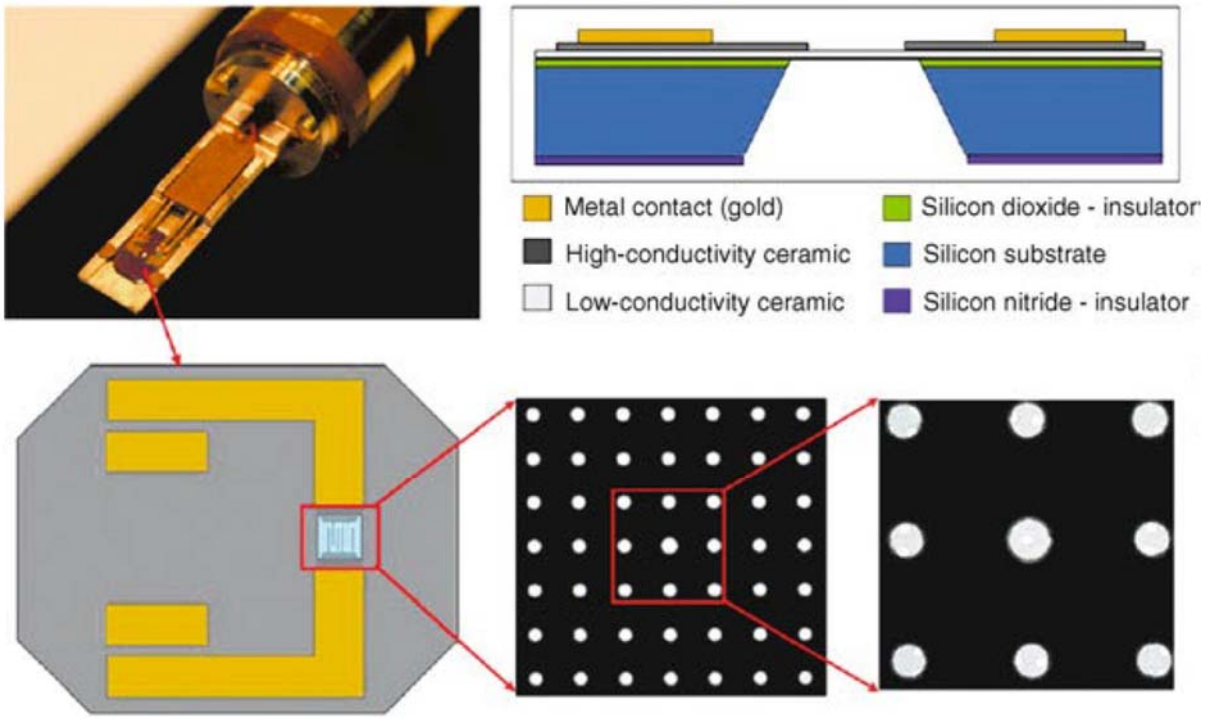

Figure 3. Protochips MEMS heating device composed of Au contacts supported by a silicon substrate.[1]

deposition experiment conducted at the same time. However, the calibration for temperature may be limited through an optical pyrometer under atmospheric pressure, and the direct attachment to filament is also limited in filament wire heating stage. As described above, many in situ TEM heating experiments are conducted through commercial MEMS device. The heating experiment is carried out in the state where there is no deviation through operating calibration of the chip in advance. Additional heating can be induced by the electron beam during the analysis. The different phenomenon of generally known bulk materials, such as the depression of melting point occurred at high vacuum of 10^{-7} torr in TEM, is considered. We can directly observe the atomic behavior, but the confinement effects on the nanomaterials may also happen to non-ideal thermal behavior.

In situ TEM mechanical testing is one of the most effective approaches. Compared with the previous cases, there are many types of mechanical holder such as indentation, bending, tensile, compression or scratch. The three categories are usually considered in studying mechanical properties. First, the elastic deformation corresponds to the reversible deformation including the measurement of the yield stress. The plastic deformation as the permanent deformation and fracture when the final breaking occurred are considered. Larger dynamic range of elastic and plastic phenomena observed in nanostructured materials during in situ TEM mechanical testing. The behavior of dislocations in confined spaces may not match the theory we know. So. what is important is that the deformation mechanism at the nanoscale extend to the case of bulk materials. The mechanical properties of these nanomaterials are crucial factors in designing devices where predictable and reproducible operation is important. The nanomaterials demonstrate many interesting properties that are not studied in bulk materials. It is possible that the piezo-driven setting allows us to do such experiments quantitatively. Furthermore, since the deformation mechanism is difficult to fully understand through post-term analysis, real time observation provides direct imaging of dislocation behavior and characterization of the defects. This mechanical testing was done first in the scanning electron microscope (SEM) as well, because the SEM provide plenty of space to attach additional equipment in the chamber. But many researchers want to characterize lattice defects at atomic scale. Not only this reason, but there are also techniques of diffraction pattern or darkfield imaging for obtaining a more distinguished image of the change in crystals. The coupling of high resolution techniques offers the potential to reveal a transient change in measured force or the displacement. Mechanical testing with difference variables such as total displacement, displacement rate can be controlled. Because of the difficulty of parameter control in mechanical testing for nanoscale materials, mechanical properties have less investigated.

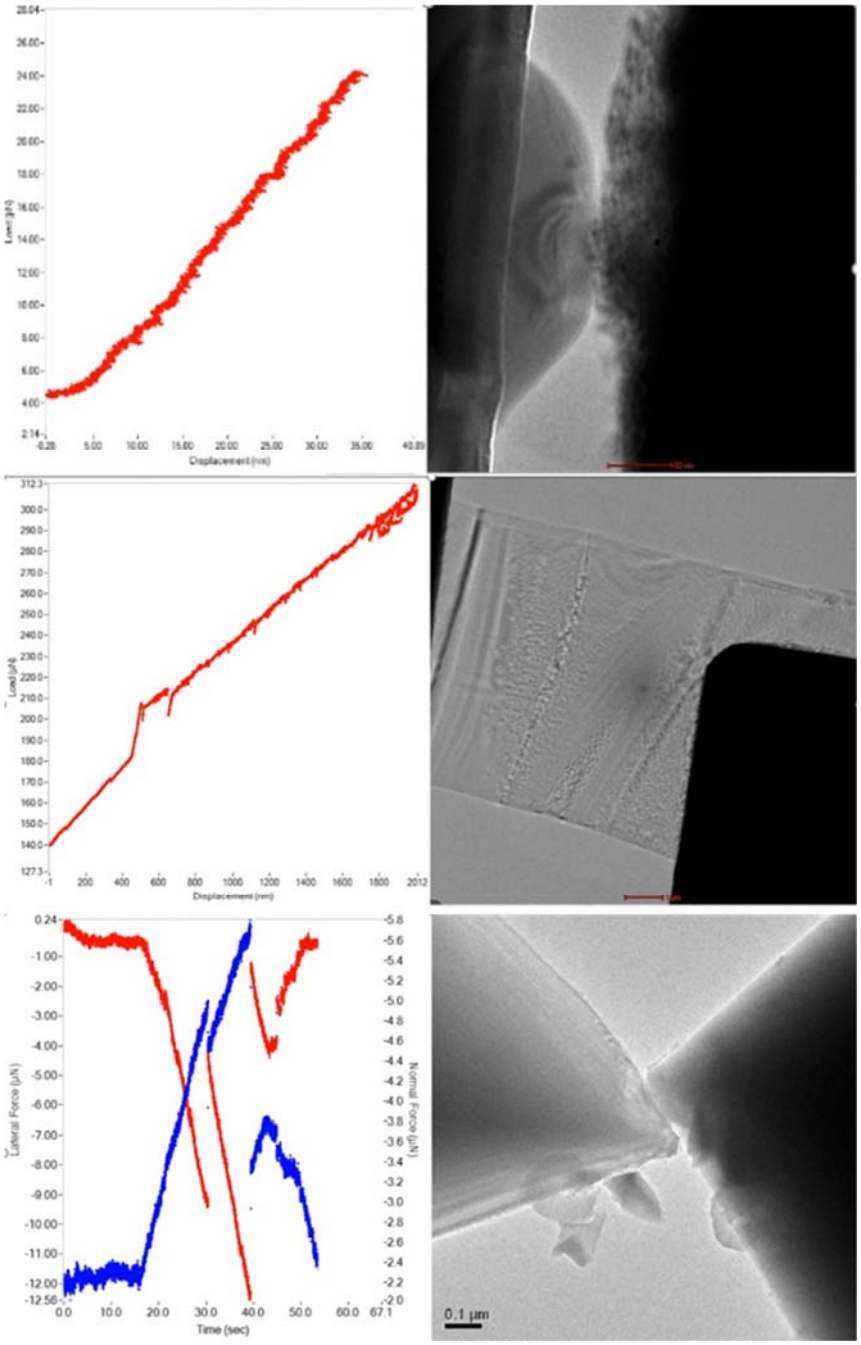

Figure 4. Examples of in situ TEM mechanical testing (a) Compression testing (b) Tensile testing (c) Scratching testing.

Chapter 3. Direct Observation of Leakage Currents in Capacitor using In Situ Transmission Electron Microscopy

3.1. Objective and ideas

The fourth industrial revolution, the so-called "industry 4.0" represented by cyber-physical systems, includes examples such as developing self-driving cars and artificial intelligence. Interoperability between systems is required in next-generation systems. For example, these systems include oscillators, filters, mixers, phase-shift networks, and analog to digital and digital to analog converters, which are applications of MIM capacitors. With the acceleration of the scaling down of integrated circuits, it has become very challenging to fabricate MIM capacitors with high capacitance density and low leakage current for nanoscale dynamic random access memory. Therefore, the reliability and stability of MIM capacitors with stacked thin films are actively being researched. However, MIM capacitors have various characteristics in their dielectric films when a voltage is applied.[18-20] From the various leakage currents in dielectric films, many studies have reported that the origin of the leakage current can be described via several conduction mechanisms, such as Poole–Frenkel (P–F) emission, trap-assisting tunneling processes, and ionic conduction.[21] Yttria-stabilized-zirconia (YSZ) thin film, one of the insulators in MIM capacitors, have been reported as having various crystal structures from the monoclinic phase to the cubic phase according to different Y doping levels,[22, 23] which influence the electrical characteristics of the YSZ thin films. In this work, an YSZ thin film deposited via atomic layer deposition (ALD) was used as an insulator in an MIM capacitor. The local crystallization of the YSZ thin film was investigated during an in-situ TEM biasing test using Joule heating and the induced leakage current. We examined the process of crystallization and the increase in the leakage current via the experimental and simulation results. It is important to understand the relationship between the crystallinity and electrical properties of YSZ thin films in MIM capacitors.

3.2. Experimental procedure

MIM capacitor in this study was fabricated using the same method as in published article.[24] A commercial ALD (SNTEK Co., ALD5008) was used to deposit the YSZ thin films, and the precursors of Zr and Y were Tris(dimethylamino)cyclopentadienyl zirconium $(C_5H_5)Zr[N(CH_3)_2]_3$) and bis(isopropylcyclopentadienyl diisopropylacetamidinate yttrium (Yerba: $Y(iPrCp)_2$(N-iPr-amd)), respectively, with 11% O_3. The YSZ thin films were deposited separately in ZrO_2 and Y_2O_3 thin films. Then, to ensure sufficient Y_2O_3 dopant activation, post deposition annealing (PDA) proceeded in a tube furnace at 527 K. To fabricate the MIM capacitor, Ru was used for the top and bottom electrodes. The top electrode was deposited via DC magnetron sputtering (SNTEK Co., RSP 5003).

A FIB (FEI, Quanta 3D FEG) was used to prepare the in-situ TEM specimens for biasing testing. The voltage was applied through a boron-doped diamond probe in contact with the top Ru electrode. The probe was controlled using x-, y- and z-axis piezo movements. When the probe contacted the electrode, stress was inevitably applied causing undesired results during the biasing experiment. Because the top Ru electrode was not thick enough, we also deposited a 3-um-thick Pt electrode using the gas injection system in the FIB. In addition, we proceeded with the experiment for the biasing test when the probe contacted a thick Pt electrode that was not milled by the FIB. The re-deposition of Ga nanoparticles is also a critical problem as a pathway to conduct current during biasing tests because Ga ions are used in the FIB system.[25] To remove conductive Ga nanoparticles, additional milling with Ar ions was conducted using a NanoMill (Fischione, model 1040).

A Titan Cube (FEI, G2 60–300) equipped with a Cs image aberration corrector was used to perform the in-situ TEM biasing experiments. The Titan Cube is optimized in an operating voltage range of 60–300 kV. We operated with an accelerating voltage of 300 kV to enhance the resolution of the TEM images after we confirmed that no crystallization occurred for an electron-beam at 300 kV. A bias voltage was applied using a Picoindenter 95 (Hysitron, PI95) system with an electrical characterization module. Sweep testing and a constant voltage mode was performed to measure the current–voltage (I–V) curves to observe the process of crystallization in the YSZ thin film. The detailed procedure for the in-situ TEM experiment is described below.

In addition, because the thickness of the TEM specimen was thin for the transmission of electrons, we conducted experiments on the crystallization in a bulk state to examine the effects of size differences. A probe station (MSTECH, MST 4000A) was used to apply a voltage to the top Ru electrode in the form of a rounded shape via a mask pattern.[26] Then, XRD (Bruker, D8 Advance) was used to confirm the crystallization before and after the voltage application in the bulk state and compare it to the in-situ TEM results.

FEM was used to compare our in-situ TEM results and to perform a detailed analysis of the distribution of the temperature when applying the voltage. The calculations were performed using the

Joule heating module of COMSOL Multiphysics (COMSOL Inc., version 5.2) for a stationary study in three dimensions using a non-uniform mesh for the MIM stacked device during the biasing test. When a voltage is applied, Joule heating occurs due to the current flowing in conducting materials such as the Pt and Ru electrodes. The heating equation is referred from published article.[25]

$$\rho C_p \frac{\partial T}{\partial t} - \nabla \cdot (k \nabla T) = Q_e,$$

where ρ is the density, C_P is the specific heat, T is the temperature, t is the time, k is the thermal conductivity, and Q_e is the equation for the electric current called Joule heating, also known as resistive heating or ohmic heating, which is described as $Q_e = j^2/\sigma^2$. The initial values of the voltage and temperature were fixed to 0 V and 298 K, respectively, at the MIM structure. The DC voltage was grounded to the bottom Ru electrode. The geometrical information concerning the MIM capacitor is detailed in Figure 5.

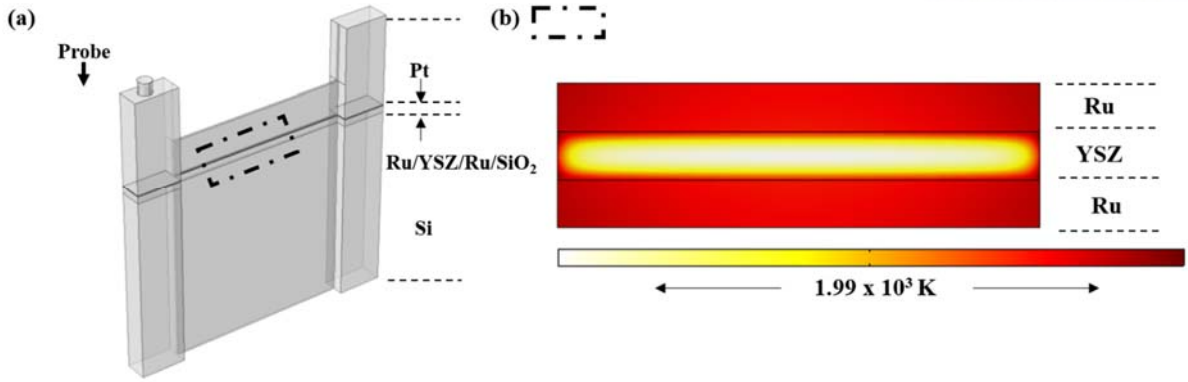

Figure 5. Geometrical information concerning the MIM capacitor model (a) A model of the MIM capacitor and the middle thin region illustrating the area milled by the FIB, which is too thin compared to both pillars. Therefore, we only considered the area in the dashed box in panel (a) to reduce the time required for the physical calculations in the software. The size-reduced model is shown in panel (b) with dimensions of 1000 nm × 100 nm × 20 nm for the width, thickness, and height of the blocks, respectively. The result in panel (b) is for an applied voltage of 2 V in an YSZ thin film with f = 1.

3.3. Results and discussion

To study the crystallization of the YSZ thin film during the in-situ TEM biasing tests, the TEM specimen was composed of an MIM capacitor on an Si substrate with a Pt electrode-coating layer, as shown in Figure 6(a), a voltage is applied to the MIM capacitor, the interest region, via the probe. Because it was geometrically not possible to do a four-point probe test, we conducted a test for a two-contact geometry. This allows straightforward measurements of the voltage versus current characteristics before and after applying a voltage.[27] The MIM capacitor was composed of Ru/YSZ/Ru vertical stacked nanostructures. We have designed for the stacked thin film type to observe the Joule heating influence of the overall region under the top electrode rather than the electrical characterization in the contact area or the local electrode heater.[25, 28] As shown in Figure 6(b), the thicknesses of both Ru electrodes and the YSZ thin film are 10 nm and 20 nm, respectively. Figure 6(c) shows a graph of the displacement versus time for the movement of the probe during the in-situ TEM biasing tests. The overall steps included contacting the Pt electrode, supplying voltage to the MIM capacitor, and pulling away from the specimen. If the probe is contacted too strongly, undesired results could occur such as bending, cracking, or stress, inducing changes in the electrical conductivity.[29] Therefore, Pt is deposited on the top electrode Ru with a thickness of 20 nm as the concept of buffer layer. To obtain ideal I–V results not including undesired effects, we manually approached as close as 100 nm to the sample using a piezo controller.[30] Once the probe was close and touched the Pt electrode, the load force was measured at the transducer connected to the probe. Then, we performed the biasing test to observe the electrical characteristics during the sweep or constant voltage after the probe contacted the Pt electrode as indicated in sections 2–3 in Figure 6(c). After applying the voltage, the probe waited for a moment to stabilize in the YSZ thin film and then pulled away, as indicated in sections 4–5 in Figure 6(c).

First, a sweep test ranging from −2 V to 2 V was conducted to observe the electrical characteristics of the MIM capacitor; there were 1000 points in the sweep test, which was recorded over 17 s. When a repetitive sweep test was performed, the measured currents were gradually increased in the I–V curve, as shown in Figure 7. The order of the numbers from #1 to #4 indicated in the legend of Figure 7 is the same as the order of the experimental procedures. In experiment #1, a current of −0.04 nA was measured when applying 2 V, while a current of 35 nA was measured at 2 V in experiment #4. The current was increased approximately 875 times. The current values at −2 V in experiments #3 and #4 were similar. As the repetitive sweep test was performed on the MIM capacitor, we noticed that a leakage current occurred in the MIM capacitor indicating an increase in the measured currents. We speculate that there were changes in the electrical properties in the YSZ thin films during the in-situ TEM biasing tests.[31, 32]

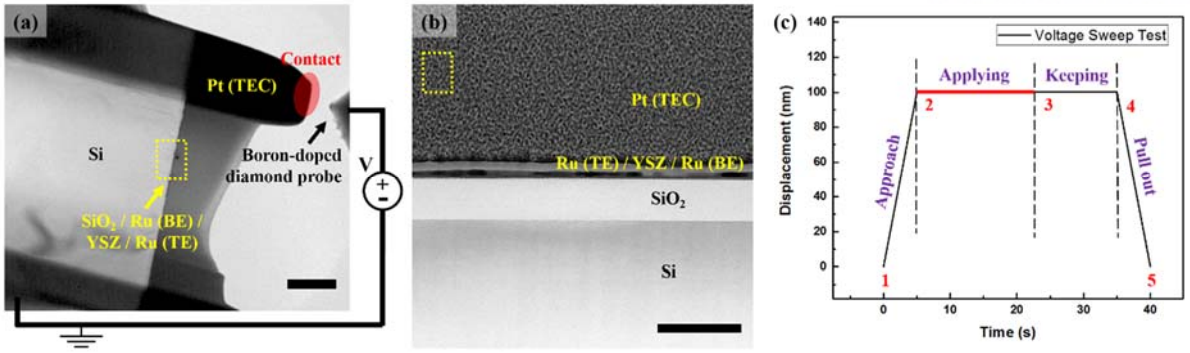

Figure 6. (a) TEM image of the MIM capacitor and a probe capable of applying a voltage. The boron-doped diamond probe makes electrical contact with the Pt top electrode contact, constructing an electrical circuit for the application of DC or sweep voltage. Si substrate is grounded through attachment to the Cu support grid. The MIM capacitor between the Si substrate and the Pt electrode is magnified with the scale bars indicating 2 μm in panel (a) and 200 nm in panel (b). (c) Graph of the displacement versus time during an in-situ TEM biasing test. The constant or sweep voltage is applied in sections 2–3.

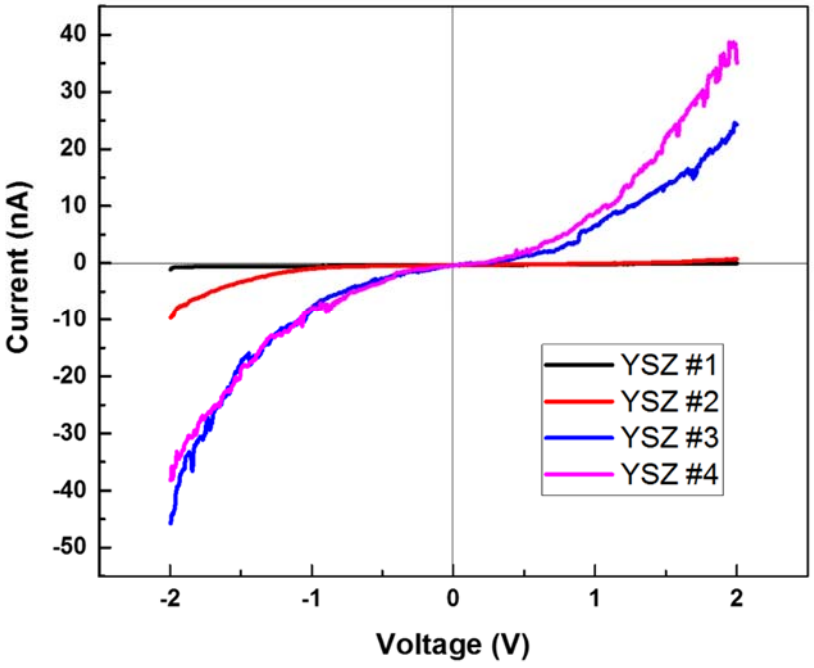

Figure 7. I–V curve of the MIM structure during the sweep test from −2 V to 2 V. The order of the numbers from #1 to #4 is the same as the experimental procedures. The number of recorded points is 1000.

Unfortunately, it was very difficult to directly observe specific changes in the YSZ thin films during the sweep test within the short time of 7 s. To observe the voltage-induced phenomena in the YSZ thin films, we applied a constant voltage of −2 V for 300 s instead of a sweep test. Figure 8 shows the results of the time versus current at a constant voltage in which the tendency of the measured current is similar to that in Figure 7. The leakage current obviously increases over time. In the YSZ thin film, while the current is increasing, a changing diffraction contrast is confirmed from Figure 8(b) to 8(g). Interestingly, it can be seen that the crystallization of the YSZ thin film took place simultaneously in several areas as indicated by the yellow arrows in Figure 8(b)–8(g) and that the crystallization did not appear to occur on the top and bottom Ru electrodes. The crystallized regions are discussed in detail below. These phenomena are not electron beam-induced crystallization as shown in Figure 9. This indicates that this is solely the result of the Joule heating caused by the current flow inside the MIM capacitor.

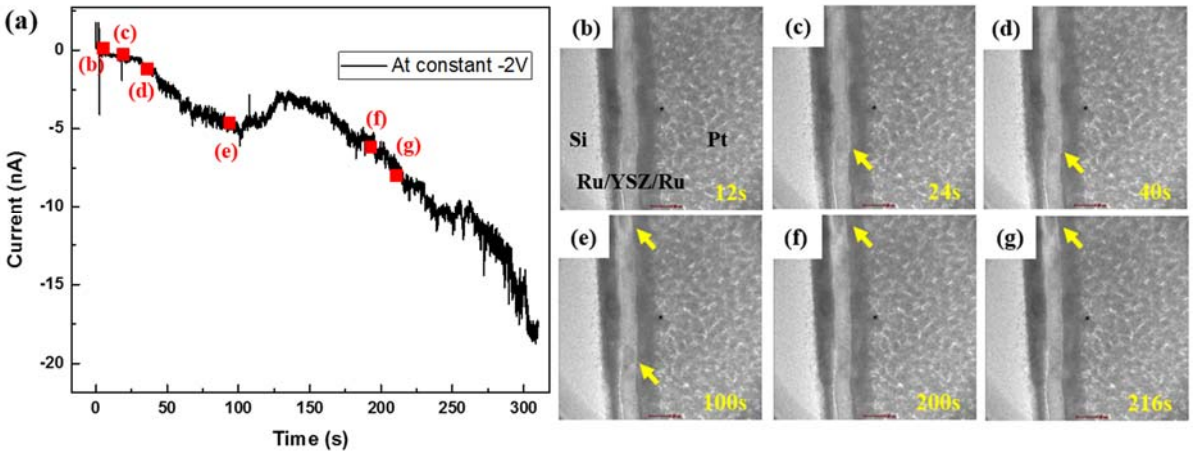

Figure 8. (a) Time versus current curve of applying a constant −2 V for 300 s. The red squares correspond to the TEM images to the right. (b)–(g) TEM series images show the change in the YSZ thin film depending on time when applying the voltage at 12 s, 24 s, 40 s, 100 s, 200 s, and 216 s, respectively.

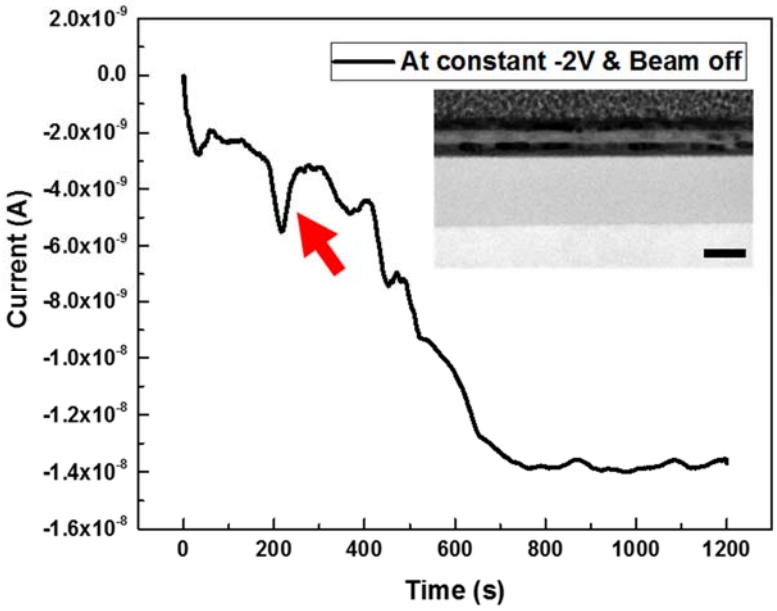

Figure 9. A time–current graph when the beam is turned off. In this case, the experimental conditions are the same as Figure 8. The inset is a TEM image after 20 min, and the scale bar is 50 nm. Crystallization occurred with the difference of contrast in YSZ thin films as inset in the Figure 9. The different times for the increasing leakage current between this and Figure 8 are caused by the size of the TEM specimen. In the case of increasing current in this figure, indicated by the red arrow, the probe moved slightly because the Pt electrode melted due to the Joule heating effect. It was confirmed that the electron beam being on or off did not influence the crystallization of the YSZ thin film.

To examine the phenomena of the voltage-induced crystallization in detail, the YSZ thin film was analyzed via HRTEM before and after the in-situ TEM experiment at the same conditions as in Figure 8. Figure 10(a) shows the HRTEM image of the YSZ thin film before applying the voltage. The dark thin films are Ru electrodes and the middle layer is the YSZ thin film. The inset of Figure 10(a) shows a Fourier transform of the image indicating the degrees of crystallinity in the YSZ thin film when comparing the intensity of the reflected spots. There may be a certain amount of crystallinity in the YSZ thin film due to the result in the inset of Figure 10(a). However, it is difficult to say that this is a completely crystallized YSZ thin film. Figure 10(b) shows the radial distribution function (RDF) of the d-spacing in the YSZ thin films prior to crystallization. The RDF describes how the degrees of crystallinity vary as a function of the d-spacing. We observed that the d-spacing of the YSZ thin film had a wide range from 2.53 Å to 2.95 Å. Figure 10(c) shows the result after applying a constant voltage of −2 V. We clearly confirmed the lattices in the HRTEM image, and the Fourier transform in the inset also identified definite reflections showing crystallization. The RDF results in Figure 10(d) show a d-spacing of 2.95 Å, which is consistent with cubic ZrO_2 (111) according to JCPDS 27-0997. This indicates that the previously reported yttrium-doped ZrO_2 transformed into a cubic form and that a fluorite-type structure, such as the YSZ thin film, structurally prefers a closely packed (111) plane.[33] After the in-situ TEM biasing test at constant voltage, we confirmed that the crystallized YSZ (111) phase correspond to 46.16 % in YSZ thin film as shown in Figure 11. It has also been reported that the leakage current should decrease with increasing dielectric constant due to changes in the cubic structure.[34] However, in our work, it was seen that the leakage current increased while the crystallization of the YSZ thin films occurred. These results show the same tendency when the voltage is applied in the form of a thin film rather than in the form of a TEM specimen as shown in Figure 12.

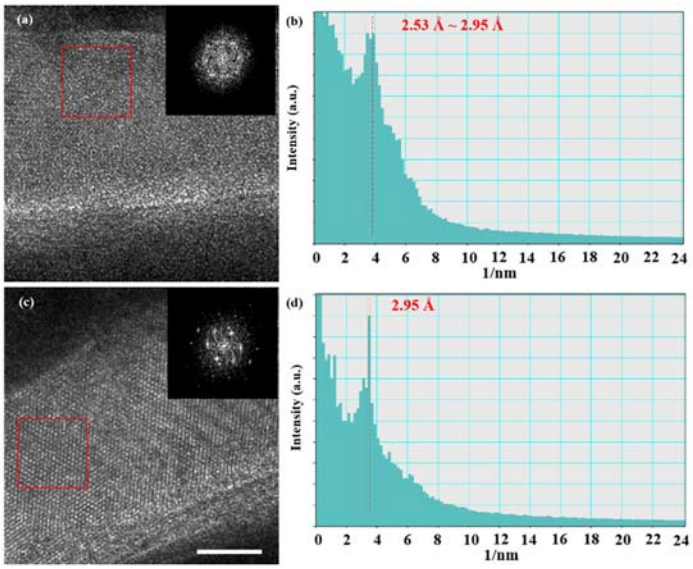

Figure 10. TEM images (a) before and (c) after applying the voltage to the YSZ thin films. The scale bar is 5 nm. The inset FFT images correspond to the red rectangles. (b) and (d) RDF results of the inset FFT images.

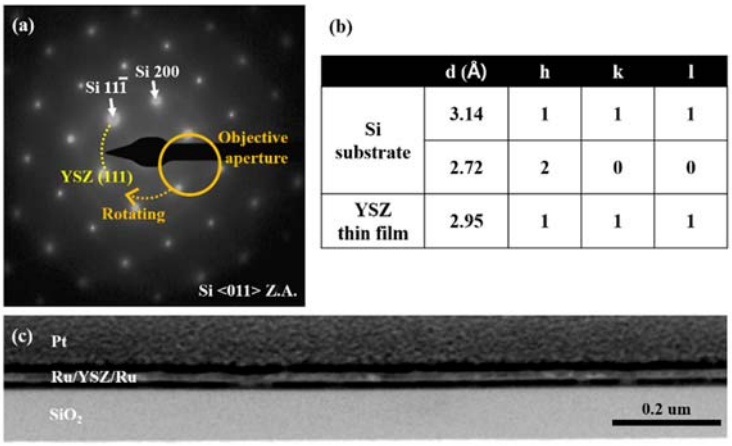

	d (Å)	h	k	l
Si substrate	3.14	1	1	1
	2.72	2	0	0
YSZ thin film	2.95	1	1	1

Figure 11. (a) It corresponds to a diffraction pattern (DP) image in the MIM capacitor along the Si <011> zone axis (Z.A.). The brightest reflections represent Si substrate indicated by a white arrow. Reflections of crystallized YSZ thin film appear very dim diffraction rings in DP because the diffractions from the nanocrystalline YSZ are very weak. But we can predict d-spacing of YSZ (111) phase through Figure 10(d). We confirm that the d-spacing of YSZ (111) phase indicated by yellow dashed line appears between the (200) and (11-1) d-spacings of Si substrate. Like the orange circle in (a), we put an objective aperture into the predicted YSZ (111) d-spacing and rotate around the central axis. (c) It is the result from the precession electron diffraction (PED), which is formed by integration over a collection of diffractions from tilted incident beams. (c) Nanocrystalline YSZ thin film, which did not appear in DP, appear here in the image. The bright regions correspond to the crystallized YSZ thin film, and ratio of the crystallized region corresponds to 46.16 % by calculation.

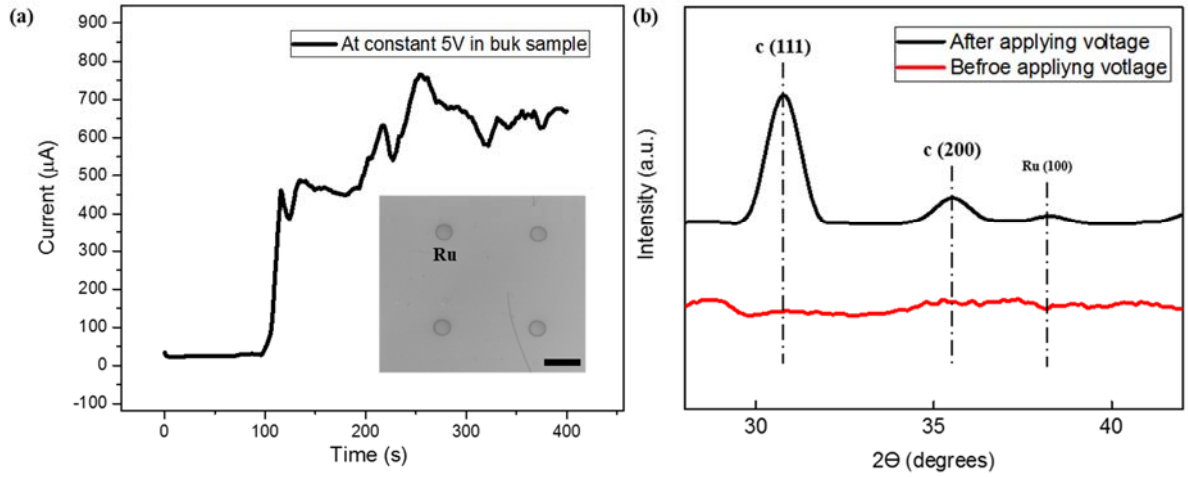

Figure 12. (a) A time–current graph of a bulk sample obtained using a four-point probe. At 100 s on the I–V curve, we can see that the measured current rapidly increases and we could speculate that there is a transformation in the YSZ thin film compared to the in-situ TEM results. Inset (a) shows the Ru top electrode deposited using a masking pattern in a round shape. Mask patterning deposition was performed at diameters of 100 μm. Panel (b) shows the XRD result before and after applying voltage to the MIM capacitor. We can clearly identify the difference between the before and after reflection peaks. After the voltage is applied, it is confirmed via the XRD and previous TEM results that the amorphous YSZ thin film is transformed to crystallized YSZ having cubic (111) and cubic (200) structures.

Up until now, we have investigated the crystallization of YSZ thin films when applying voltage via the in-situ TEM results. The thermal and electrical conductivities, the material variables above mentioned in equation for the Joule heating, are summarized in Table 1. It is known that the electrical and thermal conductivities depend on the degrees of crystallization of the YSZ thin film. The value of the electrical conductivities related to the degrees of crystallization is considered in the following equation.[35]

$$\sigma(\mathrm{f}, \sigma_a, \sigma_c) = \frac{1}{4}\left[2\sigma_p - \sigma_p' + \sqrt{\left(2\sigma_p - \sigma_p'\right)^2 + 8\sigma_a\sigma_c}\right].$$

A value of f closer to 1 indicates cubic phase crystallization. σ_a and σ_c are the electrical conductivities of the bulk amorphous and cubic ZrO_2 crystal phases, respectively.[36] σ_p and σ_p' are replaced with $\sigma p = (1 - f)\sigma_a + f\sigma_c$ and $\sigma_p' = f\sigma_a + (1 - f)\sigma_c$, respectively. Because the value of f is less than 0.4, the electrical conductivity is negligible and does not have a significant effect on the temperature, nor is the thermal conductivity affected by the degree of crystallization.

Figure 13 shows a graph of the temperature related to the degree of crystallinity in the YSZ thin film and the applied voltage. At f = 0.4, the YSZ thin film does not show a large temperature increase even if the voltage increases. However, because it is crystallized and the ratio of cubic to amorphous state is increased, the crystallization in the YSZ thin film causes the electric conductivity to increase according to the above equation. In other words, it results in a high temperature up to 1990 K in a fully crystallized YSZ thin film. In general, a post annealing process is required to create dopant activation and this causes it to be partially crystallized, which can be seen in Figure 10, which has a wide range of d-spacings in the cubic structure. The crystallization temperature for ZrO_2 is known, for the cubic phase, to be approximately 2643 K. However, a known method to depress the temperature for crystallization is Y doping (ionic radius of 0.96 Å) with a larger ionization radius than Zr (ionic radius of 0.82 Å) to cause increases in the fluorite-type crystal structure.[37] Due to these characteristics, it has been reported that the cubic phase is transformed at 1273 K in 8–9 % doped YSZ thin films.[38]

Materials	Electrical conductivity, σ ($S \cdot m^{-1}$)	Thermal conductivity, k ($W \cdot m^{-1}K^{-1}$)
Ru	**1.4×10^{7}**	**117**
YSZ (f = 0.4)	**1.4×10^{-4}**	**1.88**
YSZ (f = 0.6)	**5.6×10^{-4}**	**1.82**
YSZ (f = 0.8)	**9.8×10^{-4}**	**1.76**
YSZ (f = 1.0)	**1.4×10^{-3}**	**1.7**

Table 1. The values of thermal and electrical conductivities depend on the degrees of crystallization of the YSZ thin film. A value of f closer to 1 indicates crystallization.

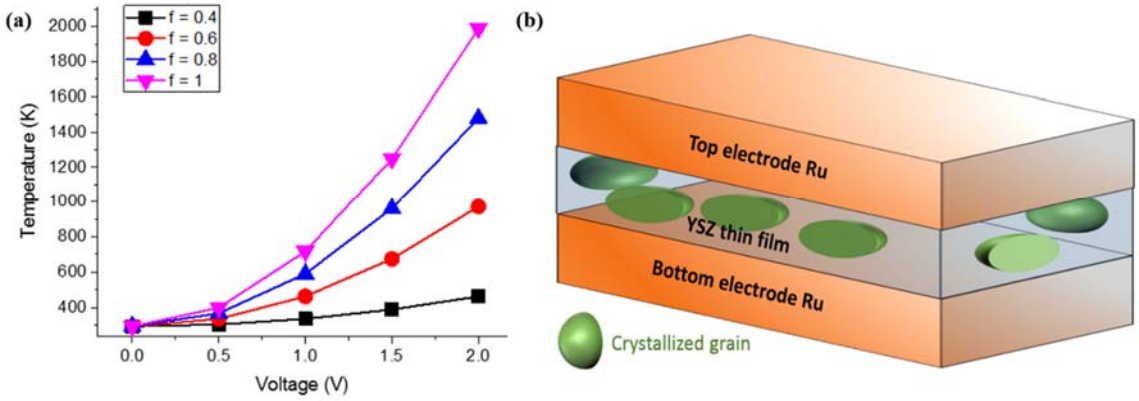

Figure 13. (a) Temperature dependence on the applied voltage and degree of crystallization of the YSZ thin films. A value of f closer to 1 indicates crystallization rather than amorphous conditions. (b) A schematic illustrating YSZ thin film biphasic crystallization. The bottom and top orange layers correspond to Ru, and the transparent middle layer corresponds to the YSZ thin film. In the YSZ thin film, the green hemispheres indicate crystallized grains.

In the case of the crystallization of an YSZ thin film corresponding to the fluorite structure, the nucleation and growth are explained via the JMAK (John–Mehl–Avrami–Kolmogorov) model.[39, 40] Crystallization progress after post annealing in YSZ thin films deposited via RF (radio frequency) sputtering, PLD (pulsed laser deposition), or ALD systems has already been reported in multiple articles based on the JMAK model.[41-43] This model includes changing the characterized Gibbs free energy relationship of the nucleation process during the corresponding induction period. In the meantime, if it exceeds the activation energy, ΔG*, for a critical size, the growth could be thermodynamically stable. The equation for this is as follows.[44, 45]

$$\Delta G^{*} = \frac{16\pi\gamma^{3}}{3(\Delta G_{C} - \varepsilon)^{2}} \cdot S(\theta_{c}),$$

Where

$$S(\theta_{c}) = \frac{(2 + cos\theta_{c})(1 - cos\theta_{c})^{2}}{4},$$

γ is the surface energy, ΔGc is the chemical potential difference between the amorphous and crystalline phase as the driving force of the transformation, ε is the elastic strain energy for the volume change, and S(θc) is the contact angle. The heterogeneous nucleation at the interface is primarily caused when the activation energy is lowered for a contact angle < 180° in above two equations. However, we can deduce that the nucleation in our case first acts on the surface of the YSZ thin film rather than at the interfacial layer, as shown in Figure 13. Note that the two cases having the same contact angle differ in their crystallization progress.

Leakage currents in YSZ thin films based on MIM capacitors have been reported in many articles. One of the phenomena in the YSZ thin films at high temperature is the finite size effect. This means that at smaller thicknesses, the YSZ thin film more easily crystallizes at the surface with an annealing temperature in a limited volume.[46] Most studies have reported the segregation behavior of yttria in YSZ thin films at high temperature.[47, 48] Even though the segregation of yttria was not observed in our study, we confirmed an increasing leakage current due to the crystallization of ZrO_2 into the cubic phase. At the grain boundaries formed by the crystallization in the YSZ thin film, the oxygen stoichiometry led to the formation of a space charge zone, which resulted in extra electron segregation. Eventually, as the concentration of extra electrons increases in the space charge zone, the probability of dielectric breakdown increases.[49] In such phenomena, oxygen vacancies act to capture the extra electrons, which become the local electron concentration. The oxygen vacancies capture the electrons via the following reaction.

$$\frac{1}{2}O_2 + \mathrm{V}_O^{\cdot\cdot} + 2e^- \rightarrow \mathrm{O}_O.$$

After electrons are caught by oxygen vacancies in the YSZ thin film, they exist in a charge state inside the band gap. If there is a charge state in the band gap, this would affect the trap-assisted tunneling and P–F conduction, which would lead to a leakage current.

3.4. Conclusion

Local crystallization of an YSZ thin film in an MIM capacitor was studied using in situ TEM biasing test. In case of the MIM capacitor including YSZ thin film as the insulator is known to transform from monoclinic phase to cubic phase by proper doping concentration control of yttrium element. During the process of making a MIM device, the PDA process carried out to get a crystallinity of the thin film in most processes, but in our case the YSZ thin film is not fully crystallized. Through Joule heating in the nanostructure to occur crystallization, we have confirmed the electrical properties of MIM capacitor with YSZ thin film using in situ TEM biasing test. However, when a voltage was applied, the currents increased due to the Joule heating in the YSZ thin film. Using a real-time analysis, we observed the crystallization of the YSZ thin film at constant and sweep voltage, which could be distinguished in the diffraction contrast in the TEM series images. Additionally, we confirmed the influence of the electron beam inside the TEM and its relation to the bulk scale. We got the same results in both case compared to the results of in situ TEM. To detailed analysis, post analysis conducted to check the quantitative and qualitative crystallized region in YSZ thin film such as results of radial distribution and PED method. In addition, the FEM results support that the crystallization with Joule heating occurred in the YSZ thin film when the voltage is applied. To explain leakage currents in crystallized YSZ thin film although improvement of dielectric constant in cubic phase, we referred the JMAK model. In this model, a leakage current was explained due to the influence of the grain boundaries caused by crystallization from the surface. Oxygen vacancies captured extra electrons. Also, this research conducted in TEM specimen having the very thin thickness. So, captured extra electrons forms space charge zone in the bandgap, and that is very easy process in limited volume site. This raises the possibility of trap-assisted tunneling and P–F conduction. In this work, I demonstrated the relationship between the crystallinity and the electrical properties of the YSZ thin film in the MIM capacitor.

(This research was published in *Nanotechnology* in 2018 and title is “Direct observation of leakage currents in a metal-insulator-metal capacitor using in situ transmission electron microscopy.”)

Chapter 4. In Situ Transmission Electron Microscopy Observation of Heteroepitaxial Growth of 3C-SiC on Si Nanomembrane

4.1. Objective and ideas

An important wide-gap semiconductor exists more than 200 poly types in structures. Among of these, silicon carbide has excellent thermal stability, high thermal conductivity, and high breakdown field.[50-52] This material is one of the suitable material for high-temperature and/or high-power devices owing to its high electron mobility up to 1000 $cm^2/V{\cdot}s$.[53] Although commercial 4H and 6H-SiC are available, 3C-SiC is the only polytype that can be grown heteroepitaxially on single crystal Si substrate due to the similarity of the crystalline structures, i.e., diamond vs. zinc-blende. Not surprisingly, the most studied substrate for growing 3C-SiC thin films is Si substrate. 3C-SiC growth on Si substrate has attracted attention of the semiconductor industrial field because of the obvious economical and technical advantages.

In nanotechnology and semiconductor fabrication, heteroepitaxy is the affordable method to get high quality crystal growth. Although high interest about heteroepitaxial growth 3C-SiC, it still has problems to high quality and large area production. It is well known that typical problems are the mismatches of lattice parameters (a_{SiC} = 0.436 nm, a_{Si} = 0.543 nm) and thermal expansion coefficients causing defects and strain at the interface.[54, 55] Additionally, the strong affinity of the Si surface to hydrocarbon gases is difficult to grow heteroepitaxy in several processes typically using volatile precursors.[56] Because of these reasons, stacking faults (SFs), double positioning grain boundaries (DPBs) and anti-phase boundaries (APBs) in 3C-SiC thin films alter its crystalline quality and limit the technological application in electronic devices.[57, 58] Although increasing layer thickness, the strain can be gradually reduced. But wafer bending gets more pronounced.[59] To overcome these problems, many improvements have been proposed as follows. Nagasawa et al. reported that off-axis oriented Si substrates reduced or even remove the regarding SFs and APBs so called planar defects.[60] Lien et al. deposited SiC buffer film to enhance adhesion to the Si substrate with significant reduction in voids.[61] Despite these efforts, there is still a lack of research on heteroepitaxial growth 3C-SiC thin films.

To fundamentally solve these problems, TEM research enabled analyzing on atomic scale should be actively conducted. Through atomic scale study, we have already demonstrated many growth mechanisms we have in doubt. In recent years, based on continuous technology development, atomic-based analysis is now possible in real-time. Therefore, it is important to reflect the results of the atomic scale research to the industry in actual bulk scale. Also, in situ TEM heating about heteroepitaxial growth 3C-SiC has not been studied much. In this work, in situ heating TEM experiments were conducted to research heteroepitaxial growth about (100) 3C-SiC on (100) Si NM. Because of the

transmittance characteristics of TEM, very thin specimens are required, so we used (100) Si NM fabricated with several nm thicknesses. Not only experimental results, but also simulation shows the heteroepitaxial growth about (100) 3C-SiC on (100) Si NM. This work is to be a way to experiment with various heteroepitaxy techniques on Si NM in in situ TEM.

4.2. Experimental procedure

The specific specimens having nanoscale thickness were prepared using conventional thermal oxidation of a (100) silicon on insulator (SOI) wafer composed of top Si 100nm / SiO_2 200 nm / Si substrate at a high temperature 1000 °C to reduce the thickness of the Si NM on the top side of the SOI wafer.[62] The thickness of the Si NM was precisely controlled by modifying oxidation time to get the electron transparency in TEM. The thickness of the Si NM was confirmed via cross-sectional TEM (Titan G2 cube, FEI) at a low operating voltage of 80 kV with a minimal beam exposure approach. The cross-sectional specimen preparation was performed by FIB (Quanta 3D, FEI). Results of electron energy loss spectroscopy (EELS) were recorded with a monochromatic beam at 80kV with a probe size of 1.5 nm and an energy resolution of 0.2 eV, as measured from the full-width-at-half-maximum of the zero-loss peak.

In situ heating TEM was conducted on a double-tilted platform (Aduro, Protochips) using thermal E-chip specimen support that provides atomic resolution at a thermal ramping rate of up to 10^6 °C·s^{-1} with highly accurate temperature control of specimen. Before every experiment, the specimen was heated to 100 °C using 5 °C·s^{-1} increments, and stayed at this temperature for 15 min to remove any possible organic residuals. For every heating experiments, the specimen was heated at a rate of 1 °C·s^{-1}. During the observations, the sample was irradiated with a focused electron beam with a current density of 324 nA measured from the fluorescent screen, and the all movies were recorded with a free software (Bandicam, Bandicam company). Because we can`t upload the move data for the system of this paper, we used the captured images from the movie. All reported temperatures are based on the Protochips calibration. It is also essential to assess that the in situ growth is a result of thermally assisted evolution or electron induced process. Therefore, we compared experiments with and without constant electron beam irradiation on the samples. The detailed results are described in the following session.

Each structural model was created using the 3D visualization program (VESTA, JP minerals). For modeling of (001) 3C-SiC on Si NM, the interfacial structure is ignored and the distance between 3C-SiC and Si NM is 1.54 Å. The diffraction pattern for the [001] zone axis was obtained and compared with the experimental results using CrystalDiffract (CrystalMaker) with the atomic model. Image simulations of HRTEM image were performed using MaCTempasX with the experimental conditions. Since the height of the heteroepitaxial grown 3C-SiC can`t be known, we simulated the defocus on Si substrate.

4.3. Results and discussion

Figure 14(a) shows the preparation method for the Si NM and the transfer process to the heating device for researching heteroepitaxial growth of 3C-SiC. Controlling the thickness of the Si NM in SOI substrate utilized the planar lateral extent of oxidation of Si.[62] In our case, we have adjusted the thickness of Si NM to 7 nm and more information is described in Figure 15. The thickness of the Si NM used in this work is 7nm, which can be confirmed by the intensity of line profile in Figure 15(b). It can also be checked that Si NM is capped in SiOx through the result of EELS in Figure 15(c). The typical Si $L_{2,3}$ edge onset at 99.7 eV indicating the presence of crystalline silicon.[63] In top and bottom SiOx, the main peaks can be found at 106 eV and 108 eV.[64] The rest of the onset in Si is considered to be on the mixed SiOx onset.[65] Then, the etching of backside of Si substrate and oxide layer capped under and above was removed by sulfurization and HF vapor etching, and the remaining Si NM was transferred to the heating device.[66] The Si NM etched through the HF vapor is shown in Figure 14(b). Even if the Si NM keep in a free-standing form, there are lots of wrinkles due to very thin thickness. The optical image of Figure 14(c) shows a heating device with gold electrodes on both sides, and the transferred Si NM corresponding to the process of V in Figure 14(a) can be seen. The active area and sample support is a conductive, ceramic membrane located at the center of the E-chip. Resistive heating occurs when electrical current is passed through the ceramic membrane. The free-standing Si NM in the hole of the observation area as indicated by a yellow dotted circle corresponds to the TEM image in Figure 14(d). A considerable amount of wrinkle in the free-standing Si NM is also confirmed, and that the diffraction pattern (DP) image also has the [001] zone axis because we used the (001) SOI substrate as shown in Figure 14(e).

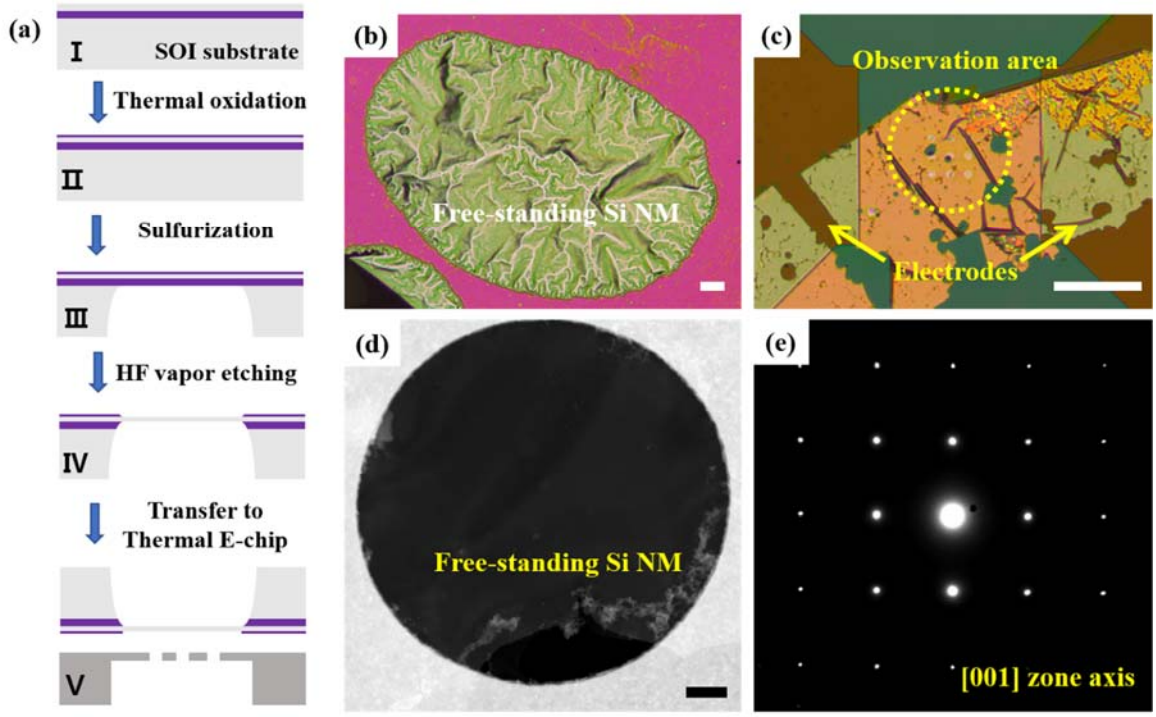

Figure 14. (a) Schematic of steps for fabricating the Si NM and transferring to the heating device. (b-c) Optical microscope images of free-standing Si NM on SOI substrate and in situ heating device. Scale bars are 100 μm. (d) TEM and (e) DP images of free-standing Si NM. Scale bar is 1 μm.

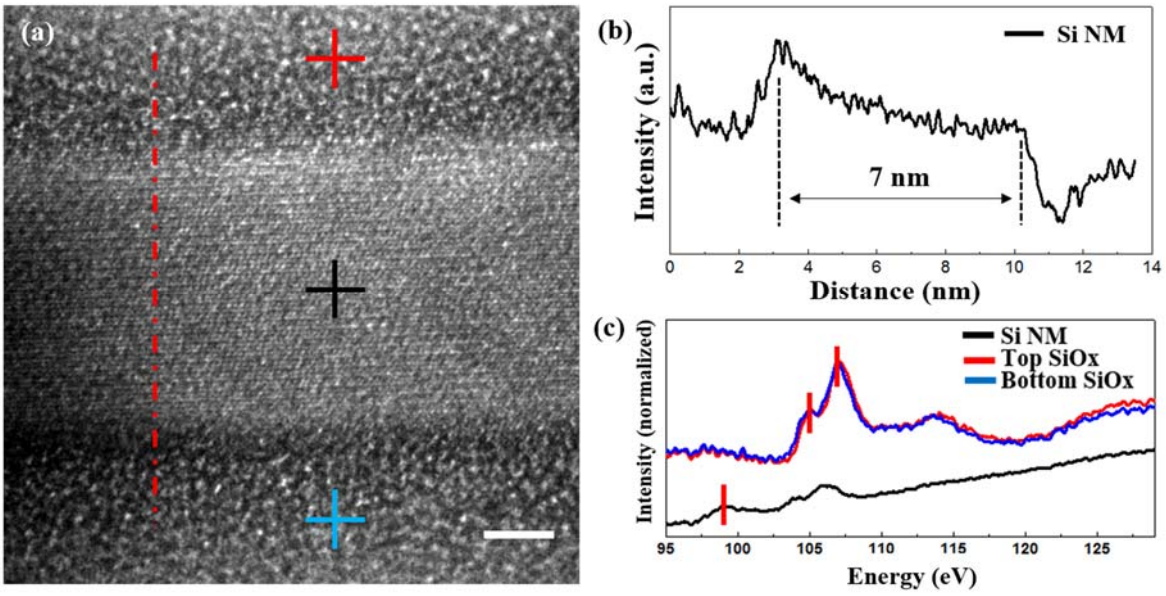

Figure 15. (a) Cross-section TEM image of Si NM capped with SiOx. The sample is before HF vapor etching and corresponds to III in Figure 14(a). Scale bar is 2 nm. (b) Intensity profile acquired from cross-section TEM image as indicated by a red dotted line in Figure 15(a). (c) EELS results obtained from Si NM and capping oxidation. Colors of graph correspond to the cross color in Figure 15(a).

Figure 16 shows time-elapsed TEM images showing the Si NM heated at 800 °C. The melting temperatures of Si and SiO_2 in known bulk states are known to be 1414 °C and 1710 °C, respectively. But the Si NM can be observed to change at much lower temperature 800 °C during in situ TEM heating. The detailed calculation about depression of melting temperature is following.

Systematic analysis is required for the transformation in Si NM at 800 °C, which is lower than the known melting temperature in bulk states. Previous studies have already been conducted and theoretical predictions based on the experimental results was reported for depression of the melting temperature. Increasing surface-to-volume ratio is the one of the reasons for depressing melting temperature of nanostructures. As the surface-to-volume ratio increases with nanostructure, the binding energy of atoms located at the surface is lower than the binding energy of atoms inside the bulk. Typically, the melting point depression described in a nanoparticle having a constant diameter, but in our case, the Si NM is the two-dimensional thin film. So, it needs to be modified into different view from the fundamental concept of considering with particle. Based on the viewpoint of the thin film, zipper model was applied to our Si NM. Below equation is the depression of melting temperature according to the zipper model as follows.[67]

$$T_m(d) = T_m\left(\infty\right)\left(1 - \frac{\gamma}{d}\right)$$

$T_m(\infty)$ corresponds to the melting temperature in bulk state, d is the thickness of the nanostructure and γ is the parameter of the material constant.

$$\gamma = \frac{\alpha\sigma_s}{\varepsilon_\infty}$$

Depressing the melting temperature can be determined as the values of the material constant and thickness given in zipper model. The value of α is considered to be the empirical value. The value of surface energy of Si thin film, σ_s, is 1240 m·J·m^{-2} and the value of ε is 8.34 x 10-20 J. Therefore, various values of γ may appear depending on the value of α, and the result is shown in Figure 17. When the reference γ values is 0.782 in the zipper model, the depression of melting temperature is not large. But, when the value of γ is extremely large to 4, the depression of melting temperature is matched in our case. This shape affect the surface to volume ratio, which affects the cohesive energy and thermal properties of a nanostructure. Previous articles reported that nanoscale Sn platelets melt within a narrow range of 10 °C of the bulk melting temperature.[68] It should be said that thin film models are different results compared to the previous reported results about surface-to-volume ratio in the nanoparticle. As mentioned above, the depression of temperature doesn`t affect in the form of nano thin film at all.[69, 70]

In a different perspective, high vacuum environment is considered as a cause of depressing sublimation

temperature. Regarding the vacuum heating, the formula in Si monatomic molecular can be defined as follows.[71]

$$\mathrm{T} = T_b \left(1 - \frac{RT_b}{\Delta H_b} ln \frac{P}{101325}\right)^{-1}$$

T_b corresponds to sublimation temperature in bulk state, R is ideal gas constant 8.31441 $J{\cdot}K^{-1}mol^{-1}$, ΔH_b is boiling heat of Si, 455000 $J{\cdot}mol^{-1}$, and P is under pressure. Figure 17(b) is the graph about the effect of high vacuum environment upon the sublimation temperature. The high vacuum in the goniometer of the TEM corresponds to $2.17x10^{-7}$ Torr, which reflects a significant depression of the sublimation temperature in Si NM.[72] The sublimation temperature of Si in the high vacuum environment of TEM is about 1150 °C, which is enough to prove our experimental result. The difference of sublimation temperature is three times larger between the atmospheric pressure and the TEM system. In most of the in situ TEM articles, the melting point of the nanostructure related to terms of the surface-to-volume, but the effect on the vacuum system should be taken into consideration as well. In our holder system, we conducted heating experiments at atmosphere and 1300°C under the optical microscope as shown in Figure 17(c). In Figure 17(d) and (e), there is no significant change in the Si NM except for the change of the heating device. Although not included in this paper, we have confirmed that the Si NM was maintained in TEM, which is a result that can support our claim that the Si NM changes under the high vacuum system.

In Figure 16, it is confirmed that the Si NM is expanded due to thermal expansion while the temperature rises. However, some folded regions are not perfectly straightened, so the strain still exists as shown in Figure 16(a). In Figure 16(b) and (c), it could be observed that hole defects are formed gradually over time, and hole defects only occur from regions with high strain applied wrinkles. In previous studies, at elevated temperature under the melting temperature, the impurity segregation or precipitation phenomena were discussed on the basis of the atomic diffusivity to the energetically favorable defects.[73-75] As shown in Figure 16(d), as the defect propagation proceeds, thickness contrast appears around the defect. This result suggests that aggregation occurs due to the diffusion of Si atoms as the defect grows.[76] As a result of checking other regions, the thickness contrast regions were easily identified around defects. Then, as the heating continues, the layers are peeled off and the amorphous carbon layer, not the vacuum, are finally left in Figure 16(e) and (f). In addition, the nanostructures with specific orientation are formed in the aggregated region, and we confirmed that this is heteroepitaxial grown 3C-SiC. It will explain in detail what is made up in the following.

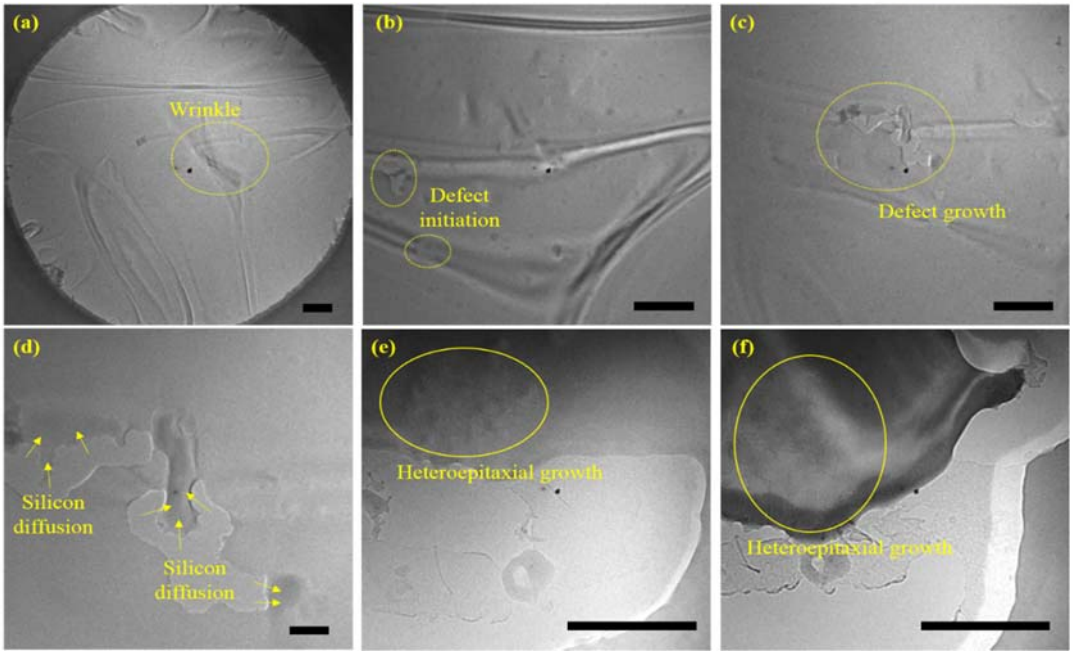

Figure 16. (a) TEM image shows the free-standing Si NM with wrinkles. Defects begin to grow around wrinkles. The scale bar is 1 μm. (d-f) As the silicon diffuses, thickness contrast appears, and it is confirmed that there is a nanostructure with specific orientation in aggregation region. The scale bars are 200 nm.

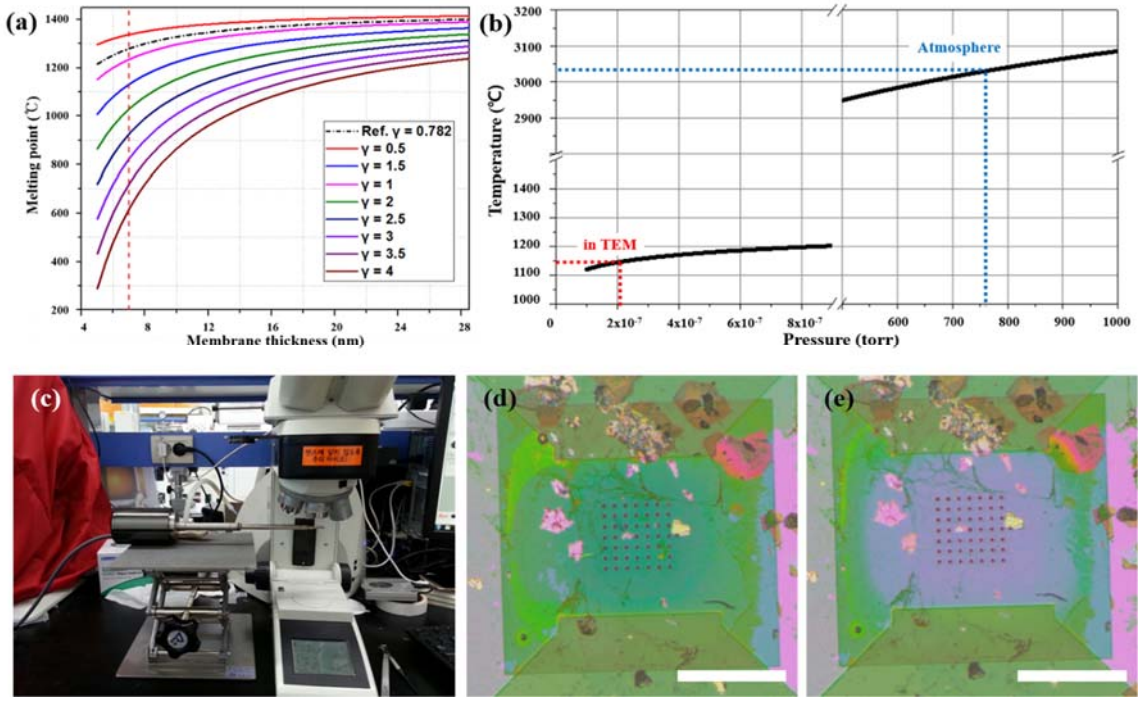

Figure 17. (a) Graph of depression for melting temperature with thickness and material constant. (b) Graph of sublimation temperature for silicon with degree of vacuum. (c-e) Ex-situ heating experiment setting under the OM. OM images of (d) before and (e) after heating Si NMs in atmosphere. The scalebar is 200μm.

To research the heteroepitaxial growth of 3C-SiC on the Si NM in more detail, the experiment was conducted at 700 °C, which is lower temperature than the previous condition of 800 °C. The growth of 3C- SiC on Si NM was confirmed again as shown in Figure 18. Unlike previous results at 800 °C, the outer layer clearly began to peel off as time passes in Figure 18(b) and (c). When the outer layer was stripped, 1D nanostructure was formed on the exposed Si NM. The outer layer is supposed to the native oxide. Interestingly, the growth direction of 1D nanostructures is <110> direction along the Si NM. The shape of the nanostructure shown in Figure 16(e) and (f) is the same. Also, the above-mentioned thickness contrast remained around the hole defect as Si was diffused. Figure 18(f) shows that the 1D structure remains in vacuum although the Si NM is evaporated.

Interestingly, the 1D structure grows in other regions not exposed to the electron beam. As shown in Figure 19(a), this 1D structure is formed along the orientation of <110>, and these structures clearly grow perpendicular to each other. The reason why hole defects forms in the regions exposed to the electron beam is presumed to be due to the further damage caused by the electron beam.[77-79] Simply heating shows that uniform 1D structure can be deposited without damaging the Si NM without hole defects. Through DP to check the orientation of crystalline of this 1D structure, we can confirm not only the result of (100) Si nanomembrane of Figure 14(e), but also additional reflection as shown in Figure 19(b). Also, these reflections are confirmed that (100) 3C-SiC is the same because of simulation shown in Figure 19(c). It can be clearly said that the (100) 3C-SiC grew on the (100) Si NM heteroepitaxially. Carbon as a source of 3C-SiC growth comes from hydrocarbons on Si NM. We also confirmed that the hydrocarbons are converted into 3C-SiC as shown in Figure 20. Contaminations composed of hydrocarbons were crystallized into 3C-SiC, and it grew when heating was conducted at 700˚C as shown in Figure 20(a) to (f). Fast fourier transform (FFT) image in the green dotted box of Figure 20(a) is corresponds to Figure 20(g), where no crystal reflections observed except for Si reflections in (100) zone axis. However, as time passes, the hydrocarbons began to crystallize and grow along the <110> direction on the Si NM, as shown in Figure 20(b) to (f). The FFT of the grown 3C-SiC is shown in Figure 20(h). It has the same reflections as (100) 3C-SiC on (100) Si NM in Figure 19(b). In addition, it is not directly verifiable, but the heteroepitaxial growth of the 3C-SiC having the <110> orientation indirectly indicates that the reconstruction of Si surface occurred. There is still debate as to whether the dimer is carbon or silicon but this orientation goes along <110> direction as shown in Figure 21. There is much suggestion of the structure of 3C-SiC on Si substrate at early growth stage. Whether Si dimers are formed on Si substrate itself, or whether other sources such as carbon or hydrocarbon induces distortion of Si lattices to form dimers of carbon. However, one thing is clear from the two proposals that the dimers grows in the direction of <110> indicating that 3C-SiC grows on the Si NM in our results. This means that reconstruction of the surface of Si substrate is an essential process for heteroepitaxial growth to occur.

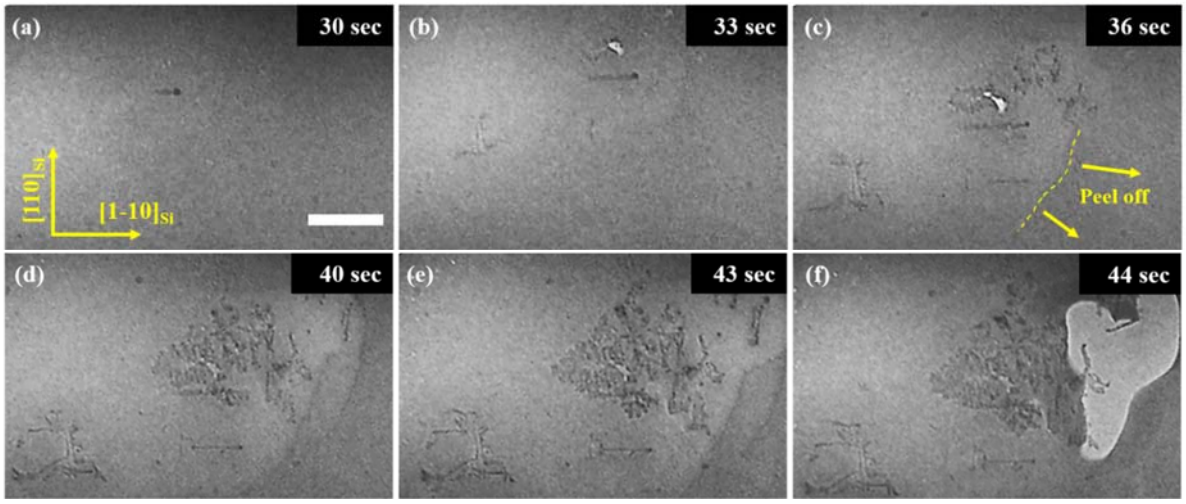

Figure 18. (a) TEM image of 100 Si NM, and the lower left direction is the same as the orientation of Si NM. (b) Defects begins to progress, and outer layer peel off. (c-e) The outer layer is getting more peeled off, and that the 1D structure also grows continuously. (f) As the hole defect grows, Si evaporates but the 1D structure remains in the vacuum. The scale bar is 200 nm.

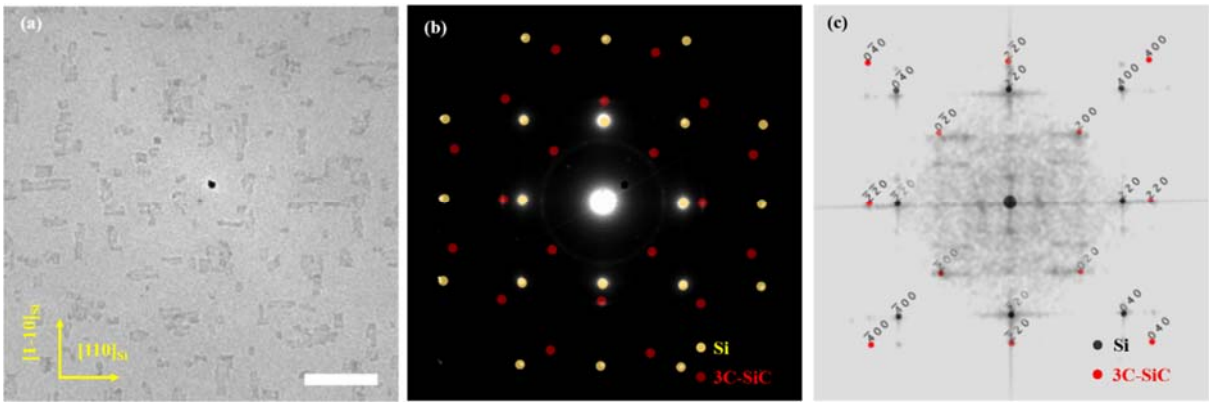

Figure 19. (a) TEM image of the region where electron beam is not irradiated at 700˚C. 3C-SiC grows perpendicular to each other. The scale bar is 200 nm. (b) DP results of 100 Si and 100 3C-SiC. The yellow circle is Si and the red circle corresponds to 3C-SiC. (c) Comparison with simulated result about 100 Si and 100 3C-SiC. The black and red circles correspond to Si and 3C-SiC, respectively.

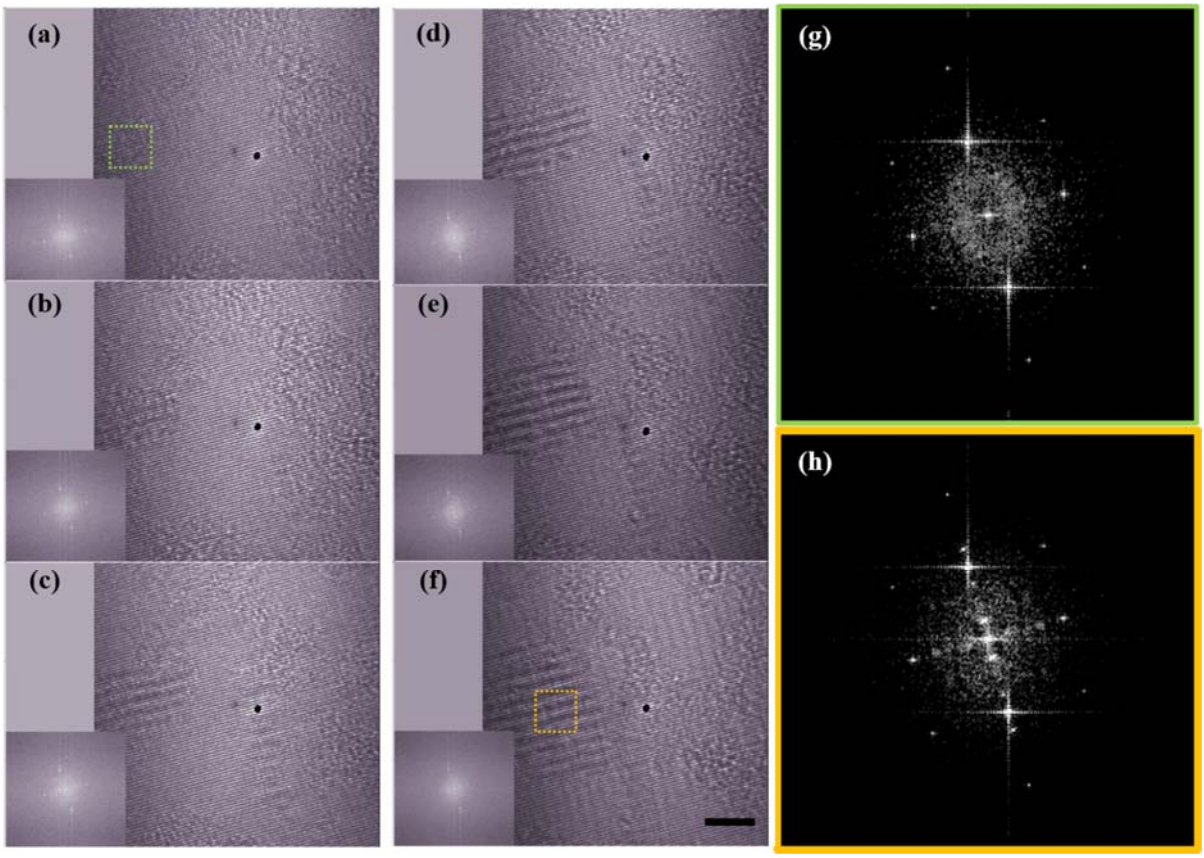

Figure 20. (a-f) Time-elapsed TEM images show that the hydrocarbons on Si NM crystallize and grow along the <110> orientation at 700˚C. The scale bar is 5nm. FFT images (g) before and (h) after hydrocarbons crystallized. The reflections of 3C-SiC on Si NM after crystallization are shown.

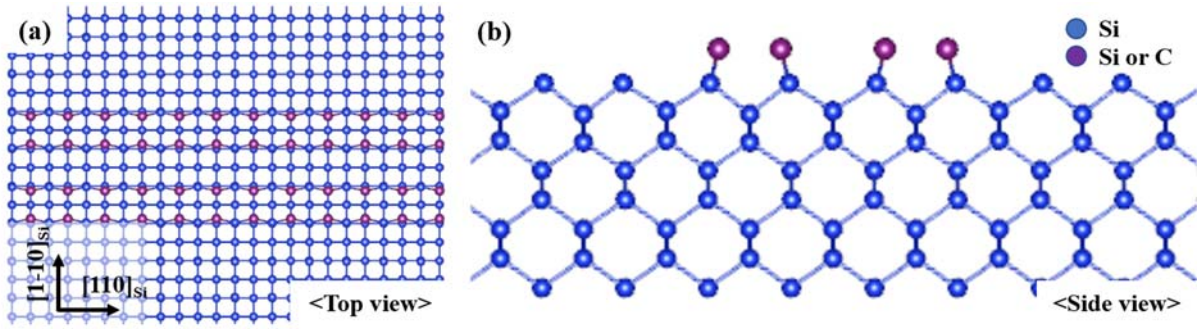

Figure 21. (a) Top view and (b) side view of modeling result when dimers are formed on the Si NM. The blue circle is Si and the purple one is Si or C.

To research how the lattices are composed of 3C-SiC which is heteroepitaxial grown on Si NM, we conducted HRTEM analysis and simulation. Figure 22(a-c) show the results for top view of models of Si, 3C-SiC and 3C-SiC on Si NM, respectively. Lattice of 3C-SiC on Si NM forms a super-lattice because it has a certain periodicity matched between Si NM and 3C-SiC as indicated by a blue dotted rectangle in Figure 22(c). Figure 22(d) is HRTEM image corresponding to Si NM and 3C-SiC on Si NM. Figure 22(e) and (f) show the FFT images which are compared with the diffraction pattern of Si NM and 3C-SiC of Figure 19(d). Figure 22(g) is the result of the simulation based on the modeling of Figure 22(c). In this result of simulation, we assumed that the thickness of 3C-SiC on Si NM was very thin, so we proceeded to defocus the Si NM. Figure 22(h) shows the combined with Figure 22(g) and cropped HRTEM images of 3C-SiC on Si NM. The lattice of 3C-SiC fits well and the trend of intensity of line profile between experimental result and simulation is also similar as shown in Figure 22(i). As mentioned earlier, in order to carry out an accurate simulation, it is necessary to include interfacial structure between Si NM and 3C-SiC. However, there is no study on the interface of heteroepitaxial growth 3C-SiC on (100) Si NM. That`s why we can only describe using simple structure with a rough approximation.

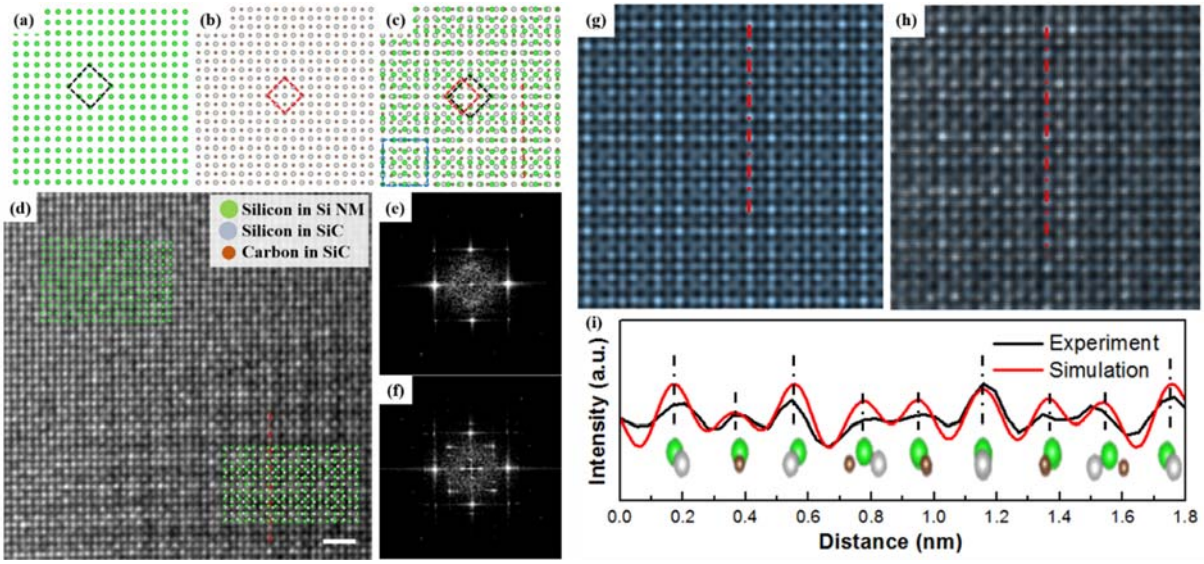

Figure 22. Comparison of experimental results and simulations for heteroepitaxial growth 3C-SiC on Si NM. (a-c) Atomic models of Si NM, 3C-SiCn and 3C-SiC on Si NM. The rhombus line represents the unit cell of each model. (d) HRTEM image of 3C-SiC on Si NM with atomic models. The scale bar is 1 nm. (e-f) FFT images of Si NM and 3C-SiC, respectively. (g) Simulation result of 3C-SiC on Si NM. (h) Combined result of cropped (d) and (g). (i) The intensity line profile of the results in (d) and (g). Compare the atomic model to the corresponding intensity.

4.4. Conclusion

Second, in situ heating TEM conducted to observe hetero epitaxial growth of (001) 3C-SiC on (001) Si NM. 3C-SiC is laterally grown and has the <110> direction on the Si NM. In addition, the growth of 3C-SiC at much lower temperature than the expected temperature in bulk state occurred. It is demonstrated by experiments and calculations resulting of a process in environment of high vacuum. We supposed that the lattice mismatch between the Si NM and 3C-SiC caused bending from initial growth. The bending resulted in large area hetero epitaxial growth of 3C-SiC without defects. We show the possibilities for other heteroepitaxial growth materials like our case in in situ heating TEM.

Chapter 5. In Situ Transmission Electron Microscopy Tensile Testing of Low Dimensional Materials

5.1. Objective and ideas

Since graphene was first prepared from graphite via mechanical exfoliation by a simple procedure involving Scotch tape in 2004, two-dimensional (2D) materials including graphene and molybdenum disulfide with a distinctive hexagonal structure has attracted intensive attention because of its extraordinary properties.[80, 81] Among them, the electrical properties of 2D materials are already known to exhibit unusual characteristics such as the formation of a Dirac point and high carrier mobility with massless particles.[82, 83] These properties indicate that graphene can feasibly be used in miniaturized electronic devices.[84, 85] The mechanical properties of graphene are also widely known to exhibit unusual characteristics, including extremely high in-plane stiffness. Therefore, graphene has been used in various industrial fields.[86-88] Expanding the applications of 2D materials in strain engineering, where these outstanding properties can be exploited, requires a detailed understanding of the relationship between the structural and mechanical properties.

Although extensive simulation studies of the relationship between the in-plane mechanical properties and structure of 2D materials have been conducted to better understand its superior mechanical behavior, atomic-level experimental evidence has been lacking. For example, the mechanical properties of graphene have not been explained in detail, and previous studies have focused only on stress and Poisson ratios against strain in the armchair or zigzag direction in graphene.[89, 90] No optimized values related to the structure for 2D materials have been deduced. Thus, studies that experimentally link structural properties with the engineering applications of 2D materials are needed. properties.

Generally, the mechanical properties of any material can be practically measured by methods such as tension, compression, and bending tests. Because of 2D geometric characteristics, the most important mechanical test for 2D materials is uniaxial tensile testing. These tests directly correspond to the reaction of forces being applied to in-plane nearest neighbors such as sp^2 carbon–carbon bonds in graphene. Uniaxial tensile testing reveals the role of three fundamental factors. The Young's modulus E, the Poisson's ratio ν and the intrinsic strength σ_{int} are terminologies of determining the phenomenological mechanical properties of 2D materials. However, the uniaxial tension testing of atomically thin 2D materials by using conventional equipment is difficult. Numerous researchers have attempted to overcome these difficulties through various approaches. In case of graphene, the mechanical properties of exfoliated graphene measured by AFM have been speculated to represent the mechanical properties of graphene.[11, 91] The Young's modulus of monolayer graphene is approximately 1 TPa, the maximum stress is 130 GPa, and the defects in graphene are known to reduce the strength

by approximately 50%.[92] Furthermore, this approach does not address the structural viewpoint. Therefore, studies to directly measure the mechanical properties of 2D materials in conjunction with their structural characteristics are needed. We proposed conducting mechanical tests through MEMS devices to address these problems.

MEMS devices, in conjunction with transmission electron microscopes, have recently been used to simultaneously characterize both the mechanical properties and structures of 2D materials. However, transferring atomically thin 2D materials onto the selective area in a MEMS device for TEM analysis is difficult. Nanomaterials are typically transferred onto MEMS devices via a FIB or by wet or dry transfer in the case of a graphene prepared by exfoliation or chemical vapor deposition.[93, 94] These processes are difficult to apply to 2D materials because of complicated problems such as unintended damage induced by the FIB and impurity problems associated with polymer dissolution. Furthermore, for the direct characterization of ideal strength, mechanical testing must be carried out on a graphene sheet exfoliated from highly ordered pyrolytic graphite, or Kish graphite, which is defect-free up to 1 mm. These problems strongly affect the reliability of expensive and sensitive MEMS devices. A process that is safer and less sensitive to MEMS devices and specimens is strongly desired.

In this work, we successfully transferred stable, clean, and free-standing exfoliated graphene to a push-to-pull (PTP) device, which is one of the MEMS devices used in uniaxial tensile testing, by using dry transfer with a gel material; we then conducted tensile testing on the exfoliated graphene. Optical microscopy and cross-sectional high-resolution transmission electron microscopy (HRTEM) images confirmed that our technique led to the successful transfer to the PTP device. HRTEM images and Raman spectra confirmed that the gel material did not influence the mechanical properties of the graphene. Furthermore, we studied the mechanical properties of exfoliated graphene via stress–strain (S–S) curves obtained by in situ TEM tensile testing. Crack propagation in graphene was also confirmed. Our developed technique enables the in situ TEM tensile testing of graphene at the atomic level.

5.2. Experimental procedure

We used natural graphite crystals (Kish graphite grade 200, Graphene Market) and MoS_2 crystals (SPI Supplies). The exfoliation process for both materials is to do the same. The materials are sonicated with isopropyl alcohol (IPA) to thin layer and weaken the interactions between the thin flakes. The materials were then heated in a box furnace (FB 1310M, ThermoFisher) for 1 h at 500 °C to evaporate the IPA.[95] We obtained the few-layer and sub-millimeter flakes by repetitive pealing by using adhesive tape as usual.

In case of graphene, the flakes transferred from the adhesive tape to a thin layer of gel material suspended on a polyethylene terephthalate (PET) film (PF film, Gel-Pak). Given that the adhesion of the PF film was far weaker than that of the Scotch tape, only few-layer graphene could be transferred onto the PF film. For few-layer exfoliated graphene transferred by PF film, it is important to distinguish the thickness that can be adequately observed by TEM. The optical contrast difference of exfoliated graphene with the PF film was determined using an optical microscope (LEICA, DM 4000M), and the number of observed layers matched the layer number determined by AFM (Veeco, MultiMode V). We also used a Raman spectrometer (Witec, Alpha 300R) equipped with the 532 nm laser to confirm the quality of the exfoliated graphene on the PTP device. Pt deposition was conducted using an FIB (FEI, Quanta 3D FIB) to ensure that the exfoliated graphene was clearly adhered to the PTP device. To avoid Ga-ion-induced beam damage while using the FIB apparatus, we conducted the deposition by using only an electron beam generated at 10 kV and 16 nA. The exfoliated graphene was not exposed to the scanning electron microscope window to avoid electron beams during deposition.

But, in case of MoS_2, oxidation process may occur in the removal process of PF film described above. So, MoS_2 is simply attached to the PDMS film and then utilized the CFA method to transfer PTP device. The transfer process to PTP device for each material is the most important process and is described in more detail below. Note that the confirming number of layers and method of deposition Pt strips are the same as graphene.

The in situ TEM tensile testing on a PTP device was performed in a Titan Double Cs corrected TEM (FEI, Titan cubed G2 60-300) at an acceleration voltage of 80 kV to reduce knock-on. The holder system used in the in situ experiments was a Bruker PI 95 TEM PicoIndenter, and the flat punch probe pushed the semi-circular part of the PTP device to perform tensile testing. Given that the PTP device itself has an identical spring with high stiffness in the lateral direction, we calibrated the S–S curve against broken target.

5.3. Results and discussion

5.3.1. In situ transmission electron microscopy tensile testing of exfoliated graphene

The PTP device capable of performing the uniaxial tensile testing of exfoliated graphene is shown in Figure 23(a). When the in situ TEM tensile testing was performed, a flat probe with a size of 100 μm pushed the hemispherical head in the PTP device. The lower area of the dashed box in Figure 23(a) was pulled by the spring at both sides into the PTP device.[96] The PTP device operates as its name suggests, and the load value is calculated on the basis of a converted value obtained from electrostatic comb drive actuators in the flat probe. Specimens for uniaxial tensile testing on the PTP device were transferred to the dashed box shown in Figure 23(a), which includes an area of interest with a 2 μm gap. A schematic of the process used to transfer the exfoliated graphene onto the PTP device is shown in Figure 23(d). When we attempted to directly transfer to the PTP device via the stamping method by using a polydimethylsiloxane or a PF film, we found that exfoliated graphene could not be transferred from the film to the interest area of the PTP device because the film was strongly adhered to the bonding material. Also, we confirmed that the PTP device could not withstand the process after several attempts to directly transfer. Thus, we were compelled to develop a new method to transfer the exfoliated graphene to the PTP device.

We developed the following method for transferring specimens to sensitive MEMS devices. First, the exfoliated graphene peeled off by a PF film was adhered to 300 nm SiO_2 on an Si substrate for the measurement of the thickness of the exfoliated graphene via optical contrast difference between the substrate and exfoliated graphene with different layer numbers.[97] Considering that the engineering stress was calculated according to the thickness of the exfoliated graphene, it provided a sensitive value for determining the film's mechanical properties. The difference in measured optical contrast was used to determine thickness matching in combination with AFM as shown in Figure 24. The exfoliated graphene on the PF film was then placed on our homemade position aligner with a hot chuck and manually controlled micromanipulators, which were used to align the specimen into the correct position as shown in Figure 25. After the sample was placed in the dashed box shown in Figure 23(a), it was heated in the hot chuck at 180 °C for approximately 1 h. The gel material in the PF film liquefied and permeated into the gap between the PTP device and exfoliated graphene.[98] When we placed the sample on an Al_2O_3 plate that was subsequently heated to 500 °C to remove the PET film for a few seconds, which was a component of the PF film, the PET film not melted but bent in response to the heat. The PET film was blown using air blow as it bent, leaving only exfoliated graphene and the gel material on the PTP device. The remaining gel material was annealed in a box furnace at 500 °C for 10 min. Only the exfoliated graphene remained on the PTP device after the annealing process.

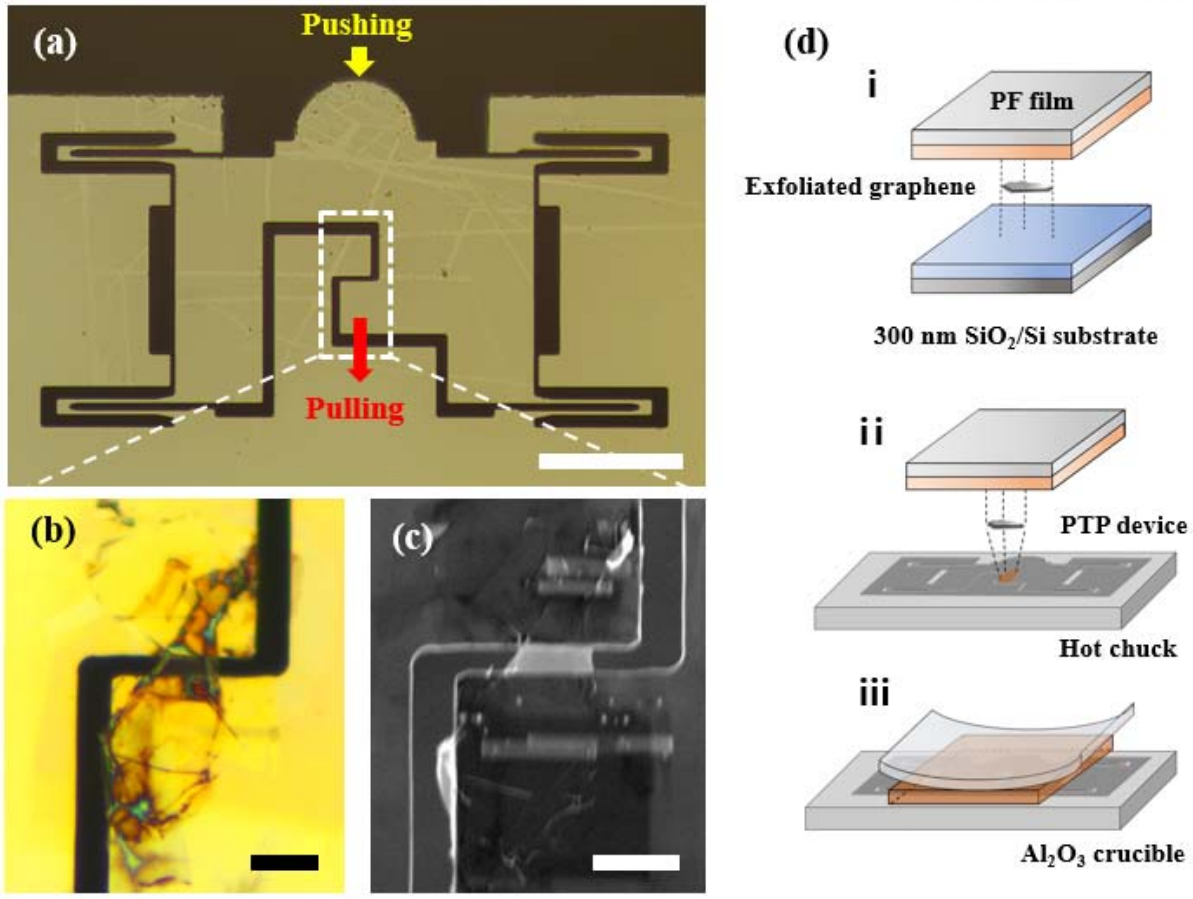

Figure 23. (a) Optical image of the PTP device. The scale bar is 100 μm. (b–c) Optical microscope and SEM images of the exfoliated graphene on the PTP device after annealing and deposition of Pt grips, respectively. The scale bar is 5 μm. (d) Schematic showing the transfer exfoliated graphene to the PTP device.

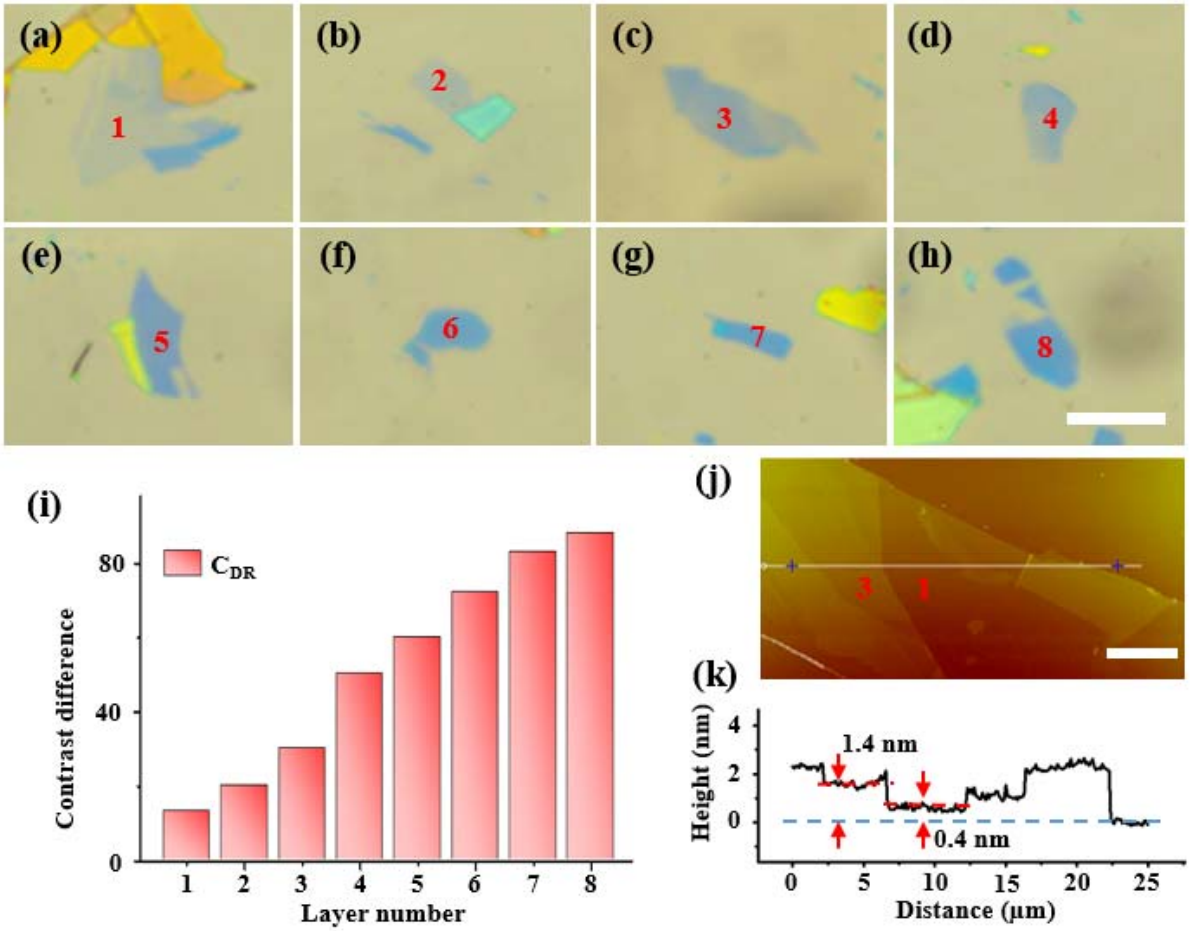

Figure 24. Optical contrast difference method to determine thickness of exfoliated graphene. (a-h) Optical images of 1L to 8L exfoliated graphene with a PF film on 300-nm SiO2/Si. The scale bars shown in (a–h) are 10 μm. (i) Graph of optical contrast difference in the number of layers in exfoliated graphene. (j) Optical image for three-layer exfoliated graphene. The scale bar is 5 μm. (k) Height profile obtained from the solid line shown in (j).

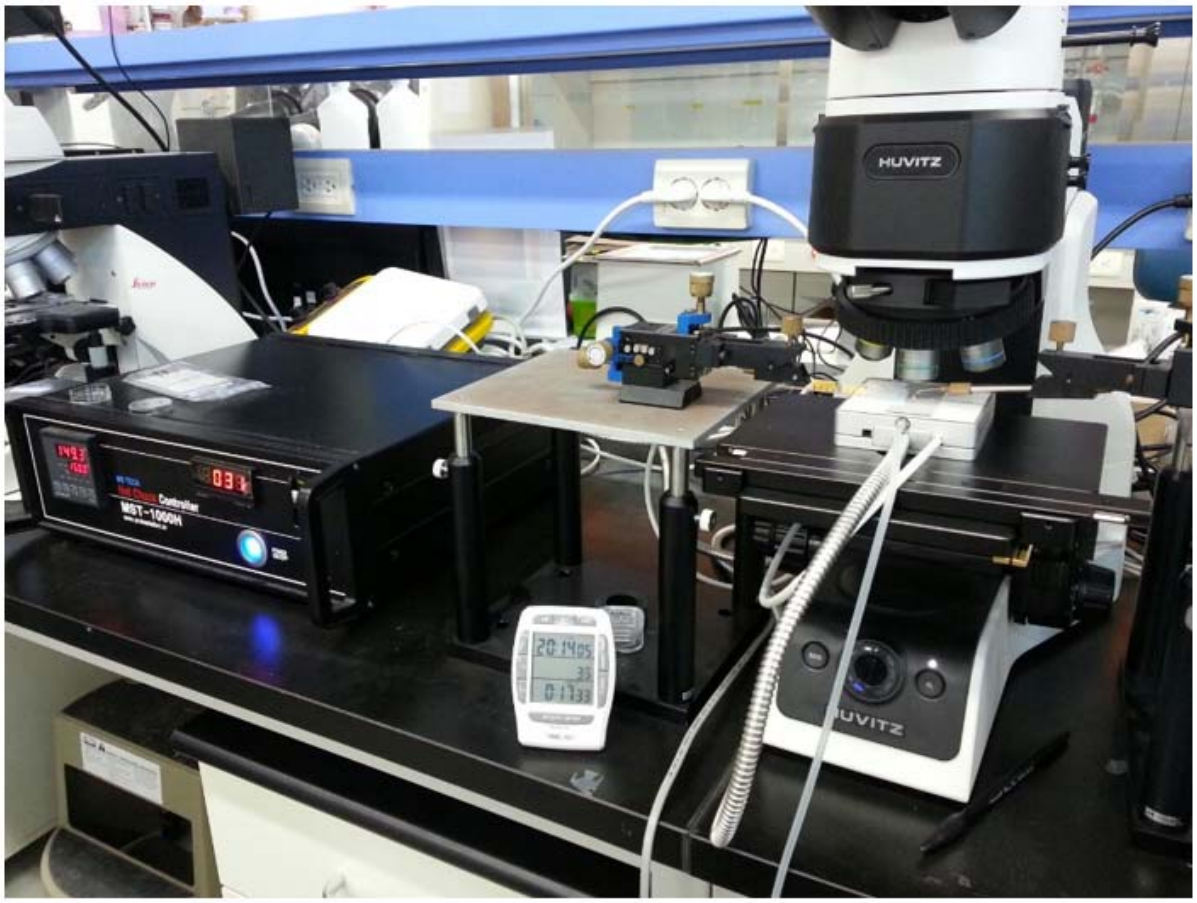

Figure 25. The homemade position aligner used to transfer exfoliated graphene onto the region of interest in the PTP device.

In our case, the sp^2 bonding of the exfoliated graphene is stable to 500 °C without forming additional defects.[99] The in situ heating Raman analysis confirmed that the gel material was evaporated when the PTP device was heated to 300 °C. Furthermore, the intensity ratio between the D and G peaks was approximately 0.09, thus indicating a low concentration of defects as shown in Figure 26.[100-102] In conclusion, we confirmed that defects were not introduced during the whole transfer process. The exfoliated graphene on the PTP device is shown in Figure 23(b). The ends of the exfoliated graphene in the free-standing area contrast because of the folded edge during this process, thus suggesting that some gel material may remain. The electron beam in the FIB apparatus was subsequently used to deposit two Pt grips to affix the exfoliated graphene to the PTP device for tensile testing. We considered the two Pt grips as the initial displacement when calculating the strain.[103]

To further study how the exfoliated graphene was transferred from the PF film to the PTP device, the above-mentioned method was conducted on a Si substrate, which is the same material as the PTP device. Figure 23(a) is an optical image of the exfoliated graphene on the Si substrate. This figure shows that the PET film was removed, and the gel remained on or under the exfoliated graphene. In these images, the gel with different colors is the portion of gel remaining on the exfoliated graphene, whereas the gel with translucent colors is the portion that penetrated under the exfoliated graphene. To identify the gel material that penetrated under the exfoliated graphene, cross-sectional TEM analysis of the exfoliated graphene was conducted. As predicted, the gel material remained under the exfoliated graphene in the HRTEM image in Figure 23(b), which was confirmed by the energy-dispersive spectroscopy results as shown in Figure 28. No significant deterioration in the quality of exfoliated graphene was observed even after the gel was removed via an annealing process at 500 °C for 10 min as shown in Figure 29.

Figure 30(a) shows a TEM image of the exfoliated graphene deposited onto a PTP device using our proposed method. We confirmed five layers of exfoliated graphene on the basis of differences in optical contrast. Unfortunately, even for the device prepared with our method, folded edges were observed in the TEM image. These folded edges could be induced by exfoliation or by an annealing process.[104, 105] The hexagonal structure of the transferred graphene was confirmed through the HRTEM image and SADP in Figure 30(b) and (c). The gel material remained partially on the exfoliated graphene in some results. To confirm the amount of gel material that remained on the exfoliated graphene, Figure 31 shows that image processing is performed to remove the periodic components of the graphene reflections from the FFT image in the inset of Figure 30(c).[106] Entirely avoiding gel-material residues is difficult, even for the established transfer method with a further annealing process, and more than 65% of the clean surface of the exfoliated graphene was covered with residue. Soft polymers, such as the gel material, are not expected to adversely affect the mechanical properties of strong and brittle exfoliated graphene.[107] Therefore, we proceeded with the uniaxial tensile testing of the exfoliated graphene in PTP devices despite the remaining residue.

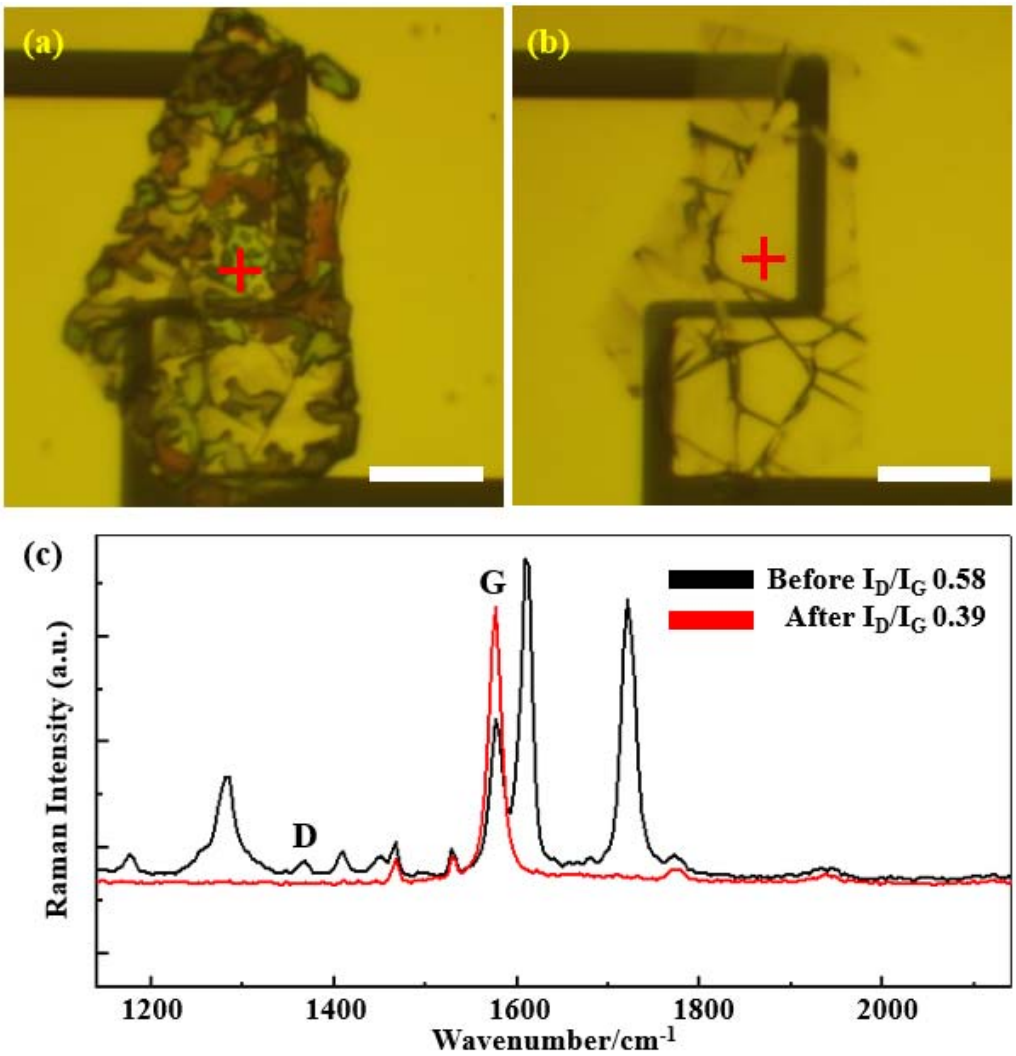

Figure 26. Optical images for exfoliated graphene on a PTP device (a) before and (b) after the in situ heating Raman experiment. The scale bars are 20 μm. The red crosses indicate the area analyzed by Raman spectroscopy. (c) The Raman spectra before and after the sample was heated at 300°C. The intensity ratios between the D and G peaks are 0.58 and 0.39, respectively. The remaining peaks shown in the "before" heating result correspond to the peaks from the gel material, which is a proprietary product, so details are omitted.

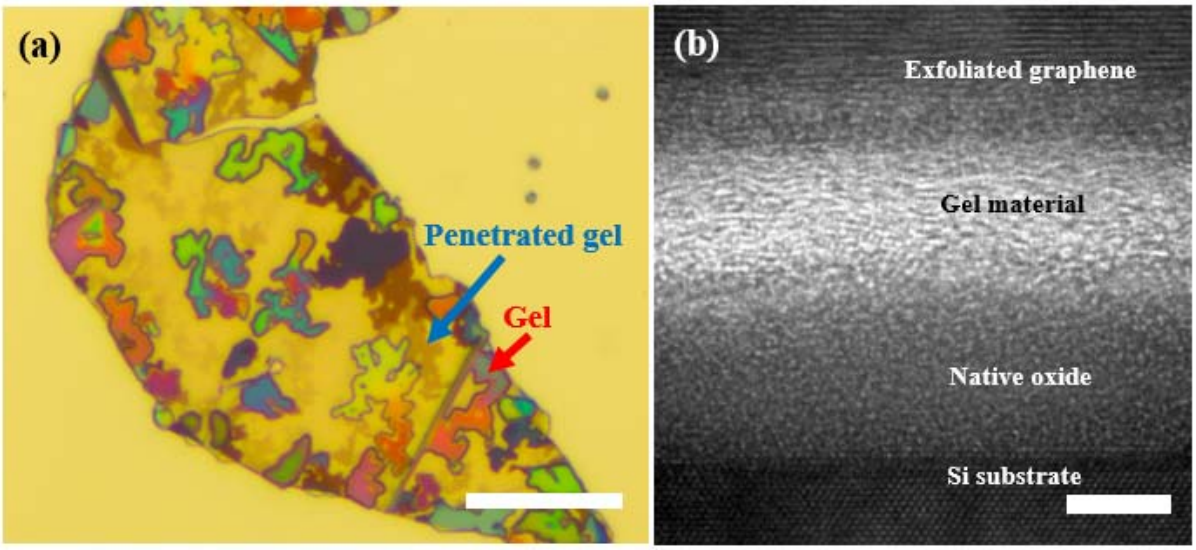

Figure 27. (a) Optical image of liquefied gel material. The remaining gel is on the exfoliated graphene, whereas the rest of the gel penetrated under the exfoliated graphene. The scale bar is 20 μm. (b) Cross-sectional HRTEM image of gel material that penetrated under the exfoliated graphene. The scale bar is 5 nm.

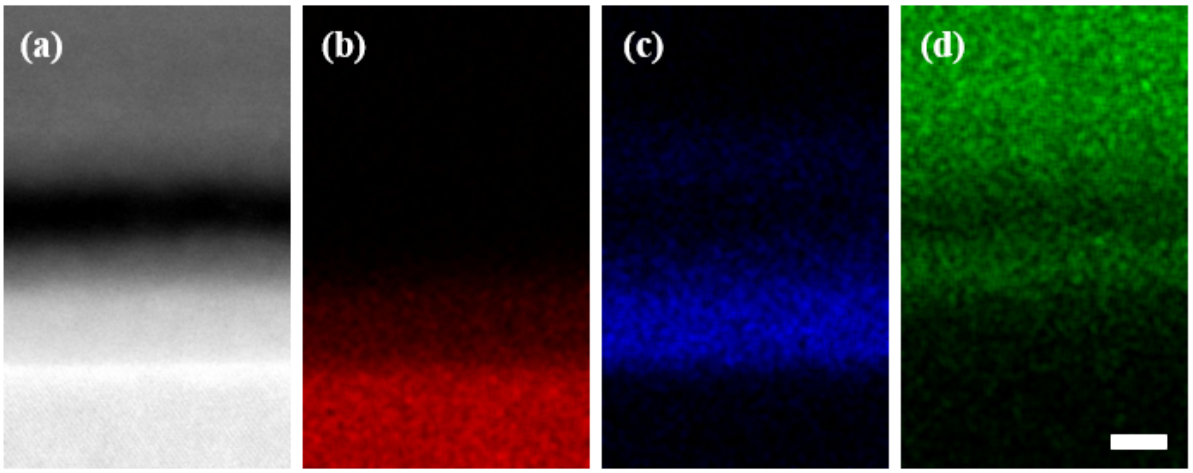

Figure 28. (a) High-angle annular dark field scanning transmission electron microscopy image of the penetrated gel materials under the exfoliated graphene. (b–d) Energy-dispersive X-ray spectroscopy elemental maps of (b) Si, (c) O, and (d) C. The scale bar is 4 nm.

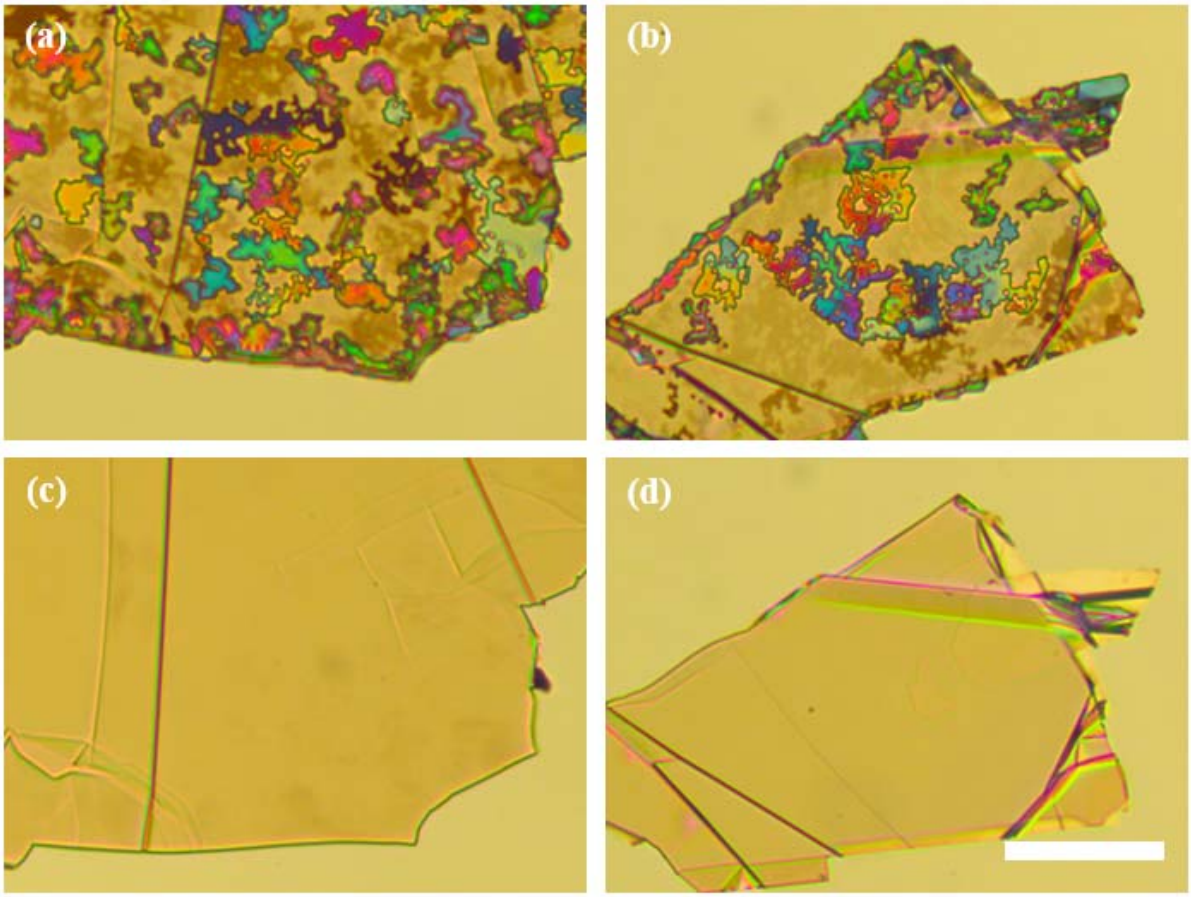

Figure 29. (a–b) Optical images of the gel materials on or under the exfoliated graphene on an Si substrate. (c–d) Optical images after the gel materials were annealed at 500 °C for 5 min. The scale bar is 50 μm, respectively.

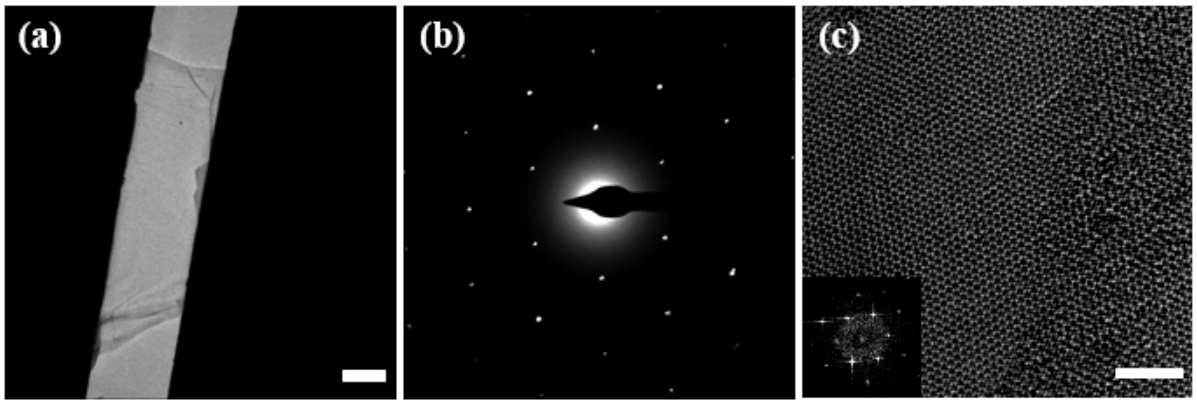

Figure 30. (a) TEM image of the exfoliated graphene on a PTP device. The scale bar is 2 μm. (b) SADP image of the exfoliated graphene. (c) HRTEM image of exfoliated graphene. The right side in (c) is the remaining gel material. The inset of (c) is the FFT of the exfoliated graphene, which is the matched SADP of the exfoliated graphene. The scale bar is 2 nm.

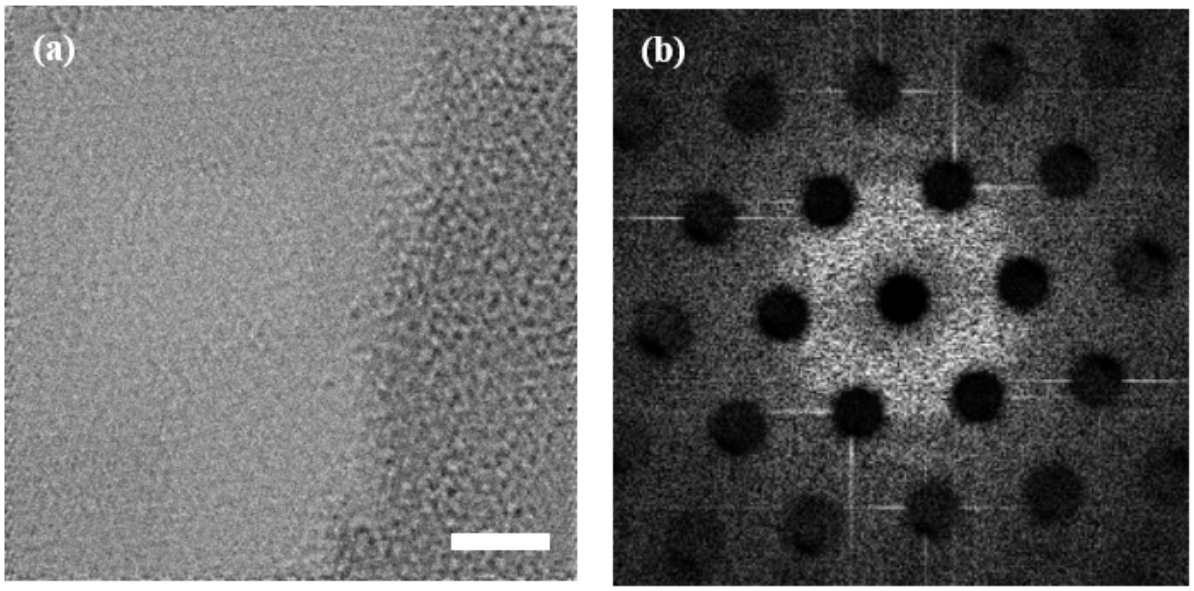

Figure 31. (a) The result of image processing after the lattice of graphene and the background were removed using software to enhance the gel material. The scale bar is 2 nm. (b) FFT image with the graphene lattice removed by mask filtering.

Figure 32 show that the result of in situ TEM tensile tests of the exfoliated graphene in the PTP device. The flat probe pushed the hemispherical head of the PTP device at a slow rate of approximately 1 nm/s. Although we could not match the rate at which cracks propagate in the exfoliated graphene, the mechanical properties and structural characteristics of the exfoliated graphene were observed via the tensile tests. The S–S curve was not continuous. The discontinuous curve represents the case where partially discontinuous mechanical behavior occurs during tensile testing. Each independent graph represents the brittle mechanical properties of graphene. The results show that the crack propagation direction along the characteristic edge of the exfoliated graphene may change. This tendency was observed not only in the sample shown in Figure 32 but also in other exfoliated graphene samples. Thus, the Young's modulus of our material exhibits a wide range. Specifically, the Young's modulus ranged from 89 to 371 GPa, and the maximum stress was 22.3 GPa. These values for exfoliated graphene are smaller than the Young's modulus of 1 TPa and maximum stress of 130 GPa obtained from AFM indentation experiments and other authors.[11] This result is consistent with previous reports that fractured graphene exhibits diminished mechanical properties. We are conducting further research into the S–S curve interpretation of few-layer exfoliated graphene, as well as into the possibility of achieving wrinkle-free exfoliated graphene on the PTP device or enabling the transfer of exfoliated graphene in a monolayer or bilayer.

We also observed the propagation of a series of cracks that originated from the folded area from Figure 32(b) to (g). We did not confirm existence of pre-cracks in the exfoliated graphene on the PTP device. However, it was natural that the crack propagated from the folded area, which is a known structural defect.[107] Furthermore, spontaneous self-tearing and peeling have been observed in pre-cracked graphene.[108] The tearing direction of the exfoliated graphene varied by 30 degrees as the angles of the armchair and zigzag edges during tensile testing. Crack formation in graphene has been theoretically and experimentally reported to predominantly occur in the direction of the armchair or zigzag edge related to the hexagonal lattice symmetry of graphene as shown in Figure 33.[109]

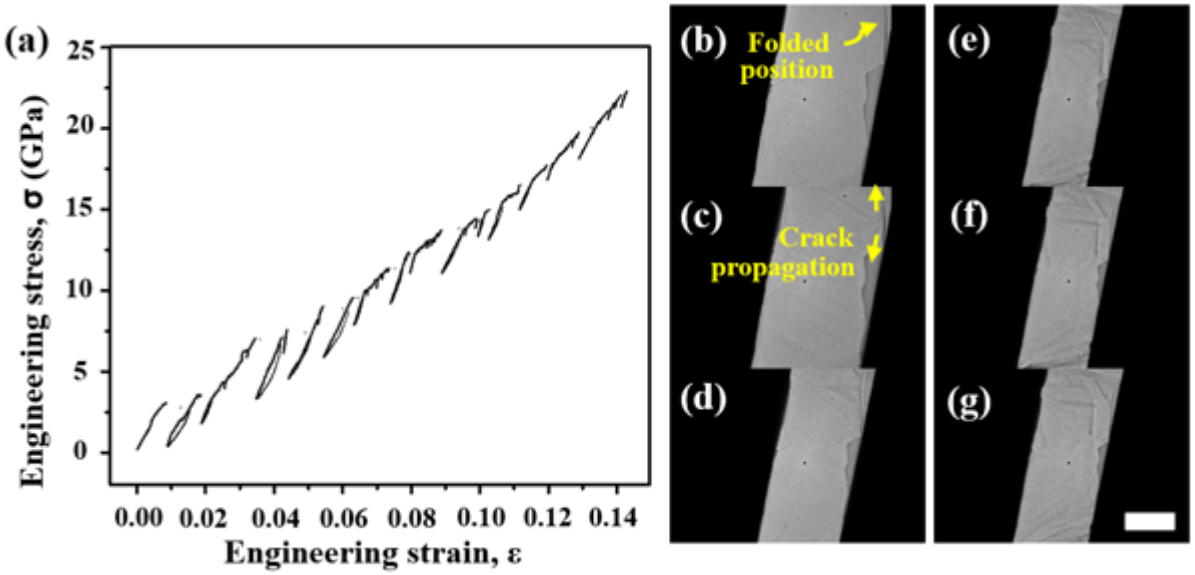

Figure 32. (a) The stress–strain curve obtained via in situ TEM tensile testing of five-layer exfoliated graphene in a PTP device. (b–g) Image series of exfoliated graphene with crack propagation. The scale bar is 1 μm.

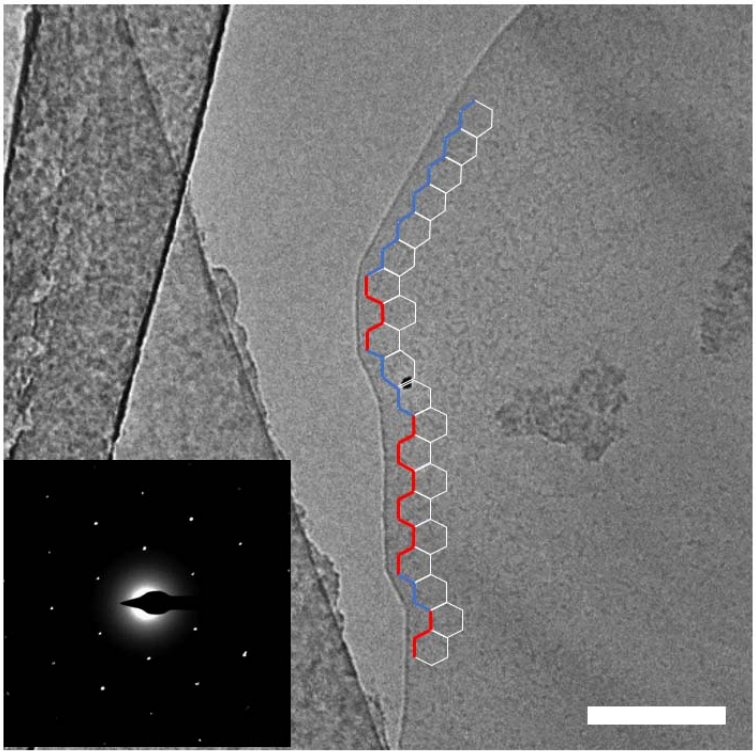

Figure 33. TEM image of exfoliated graphene after in situ TEM tensile testing. We matched the orientation of the crack propagation and graphene armchair or zigzag edges through the inset figure SADP. The scale bar is 200 nm.

5.3.2. In situ transmission electron microscopy tensile testing of bending MoS_2

Uniaxial tensile testing at the nanoscale in TEM was carried out by using the PTP device, one of the MEMS device, to verify the mechanical properties of exfoliated MoS_2 depending on degree of bending.[96] The PTP device is a push-to-pull type system where one part of the observation area is fixed and the other part is pulled out when the head is pushed by a 100 μm punch transducer as shown in Figure 34(a). Figure 34(b) shows capillary force assist (CFA) trnasfer, which is guaranteed very clean quality of exfoliated MoS_2 on the PTP device. Because of using supported water layer as an instant yet temporary glue in CFA method, the adhesion energy between PDMS and exfoliated samples can be significantly increased during the peeling off process and restored shortly to facilitate the releasing process.[110] The OM image shown in Figure 34(c) corresponds to the PTP device. When we utilized CFA method and home-made micrometer controller, it is possible to control the tensile direction of the transferred specimen along the direction of structure as shown in Figure 35. The appropriate size of specimen for transfer to the PTP device is 60 μm x 20 μm. We used the exfoliated MoS_2 with the thin thickness having the transmission in TEM through optical contrast in the OM. In the case of exfoliation for MoS_2, it has long and elongated shapes because the zigzag edge energy has a stable structure against the armchair direction as shown in Figure 36.[111] Figures 34(d) and (e) show the OM image and the DP result of the TEM for the aligned MoS_2 along the zigzag direction, respectively. In this research, all the transferred MoS_2 aligned to the zigzag direction. Additionally, the clean MoS2 is confirmed by HRTEM image as shown in Figure 34(f). Additional HRTEM images of Figure 37 shows the result of clean transfer process using CFA method.

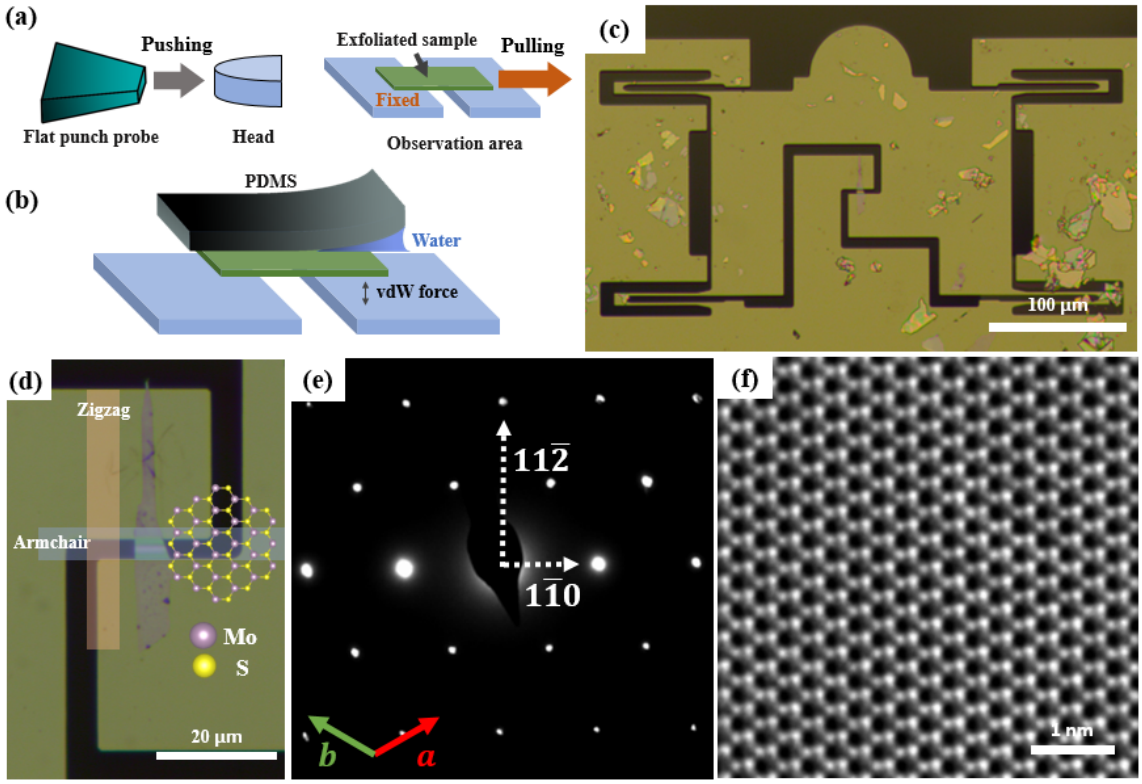

Figure 34. (a-b) Schematic diagrams of process for tensile test into the PTP device and CFA method to transfer exfoliated MoS_2. (c) OM image of the PTP device. Scale bar is 100 μm. (d) OM image of transferred MoS_2 onto the PTP device. Scale bar is 20 μm. (e) DP image of MoS_2 on the PTP device. (f) HRTEM image of MoS_2. Scale bar is 1 nm. (d-f) are all aligned in the same direction.

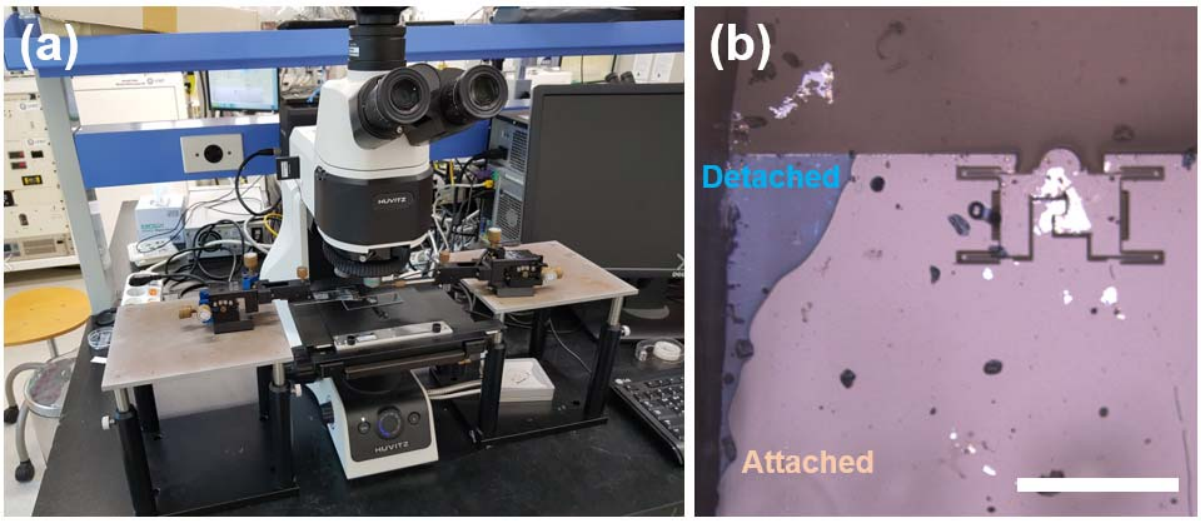

Figure 35. (a) Home-made position aligner system. It can control the TEM specimen direction (b) OM image for transferring exfoliated MoS_2 using CFA method. Scale bar is 100 μm.

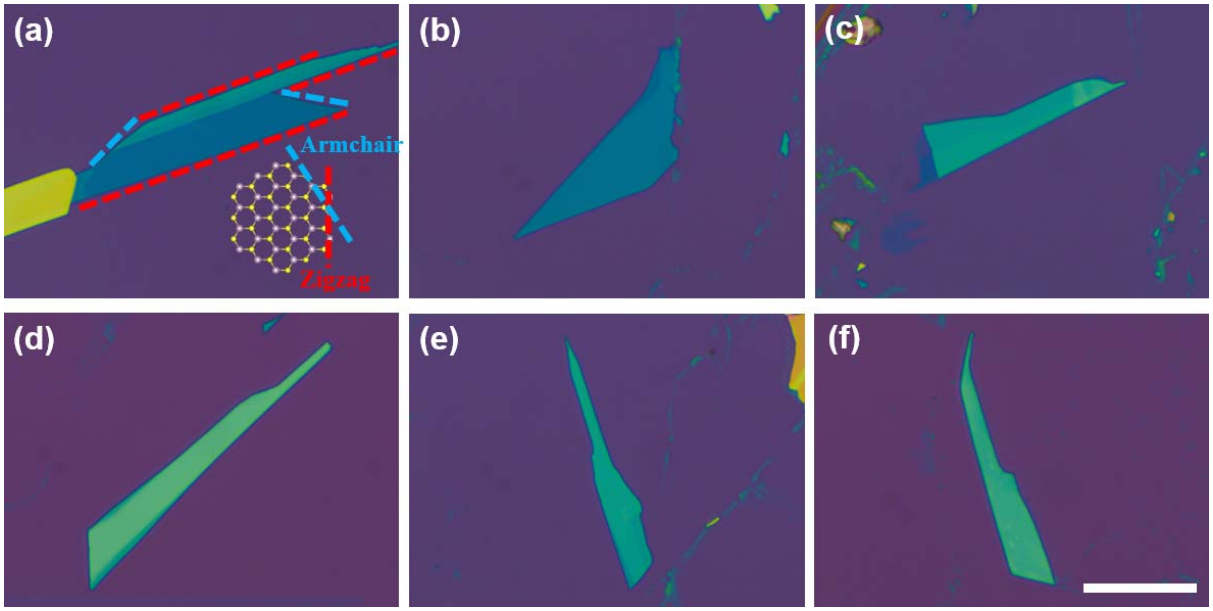

Figure 36. (a-f) Preferred edge orientations of the mechanically exfoliated MoS_2. The scale bar is 20 μm.

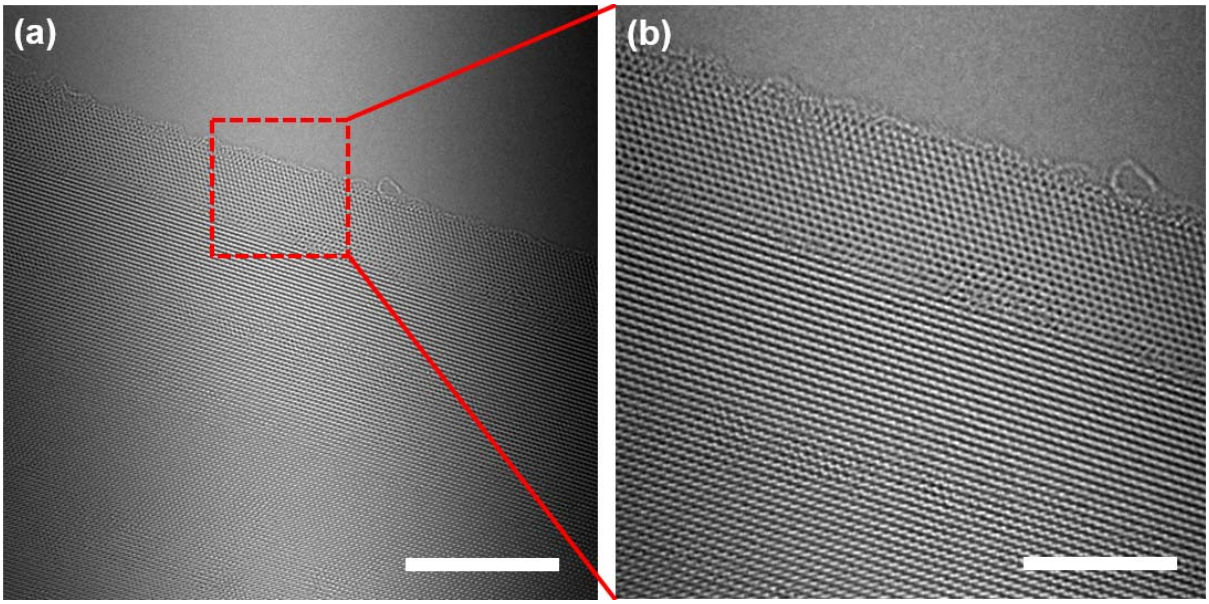

Figure 37. (a-b) Raw TEM images of exfoliated MoS2 on the PTP device. The scale bars are 10 nm and 5 nm, respectively.

Figure 38(a) shows TEM images of exfoliated MoS_2 on the PTP device by using CFA method before tensile testing. Because the transferred MoS_2 is very thin, there are some wrinkles in the observation area naturally. After tensile test is carried out in TEM, it can be confirmed that aligned wrinkles present along the armchair direction as shown in Figure 38(b). DP result of aligned wrinkles is Figure 38(c). The DP result shows that the additional reflections in the zigzag direction is estimated to be changed shape of MoS_2. In addition, the SEM images shown in the inset of Figure 38(c) can directly confirm that the MoS_2 is bent after tensile test. When we compared the DP and modeling result for bending MoS_2, we can confirm that it matches well as shown in Figure 39. Figure 38(d) corresponds to the load-displacement result obtained in the process of making the bending shape. There were 3 steps to create bending shape. First, as mentioned above, some wrinkles presented in the transferred MoS_2 or previously made of the bending shape were flatted. We supposed that the second step corresponds directly to the mechanical properties of exfoliated MoS_2. The third step was sliding due to weak adhesion between the PTP device and MoS_2. In the orange box in Figure 38(d), at the incremental step between second and third step, the detaching process was occurred and measured value for load was instantaneously drop. These three steps can be confirmed in the TEM images as shown in Figure 40. The result of the sliding can be also confirmed through the AFM image of Figure 38(e) and corresponds to the yellow box of the SEM image in Figure 38(c) inset. The thickness of the MoS_2 and displacement for sliding on the PTP device through AFM result was 9 nm and 1.19 um, respectively. This is consistent with the result of 1200 nm displacement of the load-displacement graph in Figure 38(d), which clearly shows that the sliding occurred during the pulling process of the PTP device.

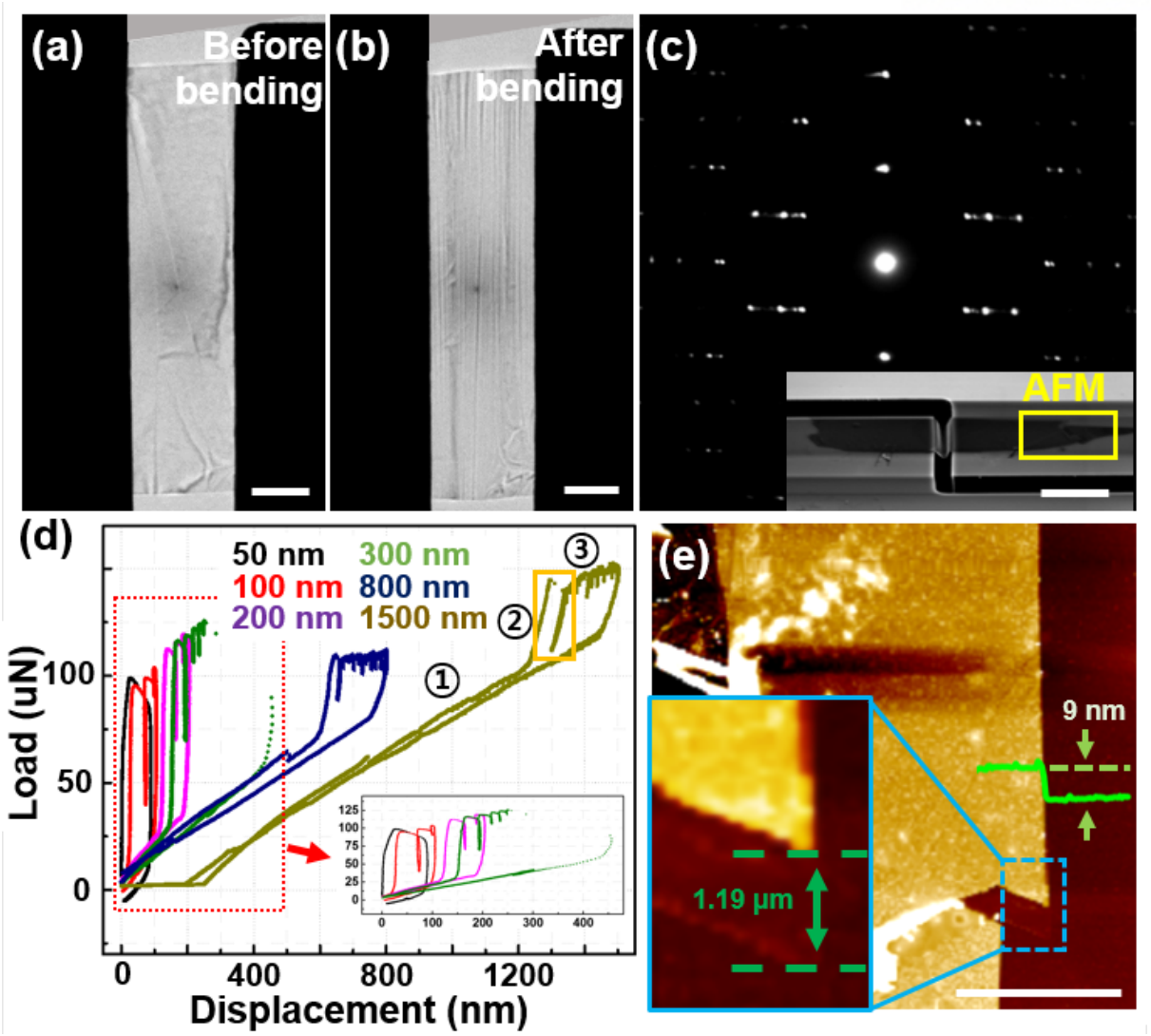

Figure 38. (a-b) TEM images of before and after bending of MoS_2 on the PTP device. Scale bar is 2 μm. (c) DP image of bending MoS_2. Inset correspond to the SEM image of bending MoS_2. Scale bar is 10 μm. (d) Results of load-displacement on the bending process. Total of 3 steps; 1. straightens, 2. tension and 3. sliding. This result is slipped to 1200 nm. (e) AFM image of the result slipped. This corresponds to inset of (c).

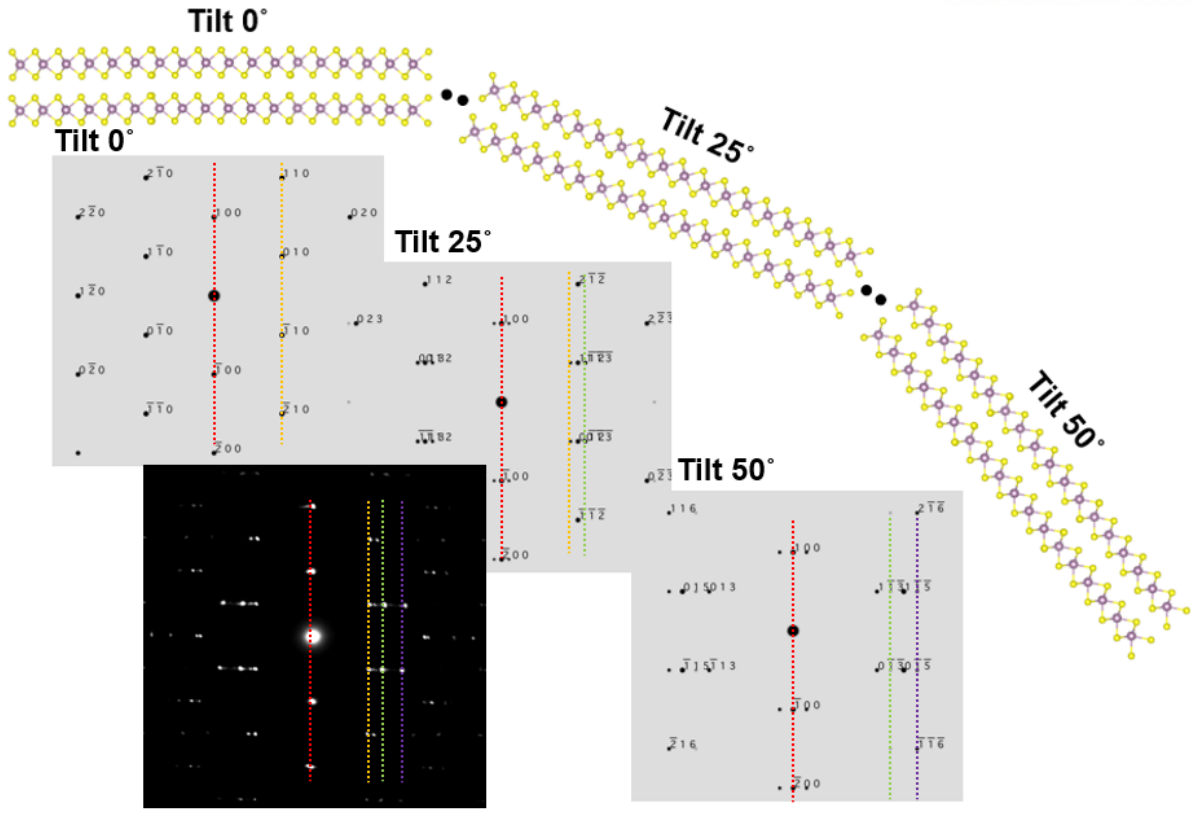

Figure 39. DP and modeling results for bending MoS_2. These results are similar to Figure 38(c).

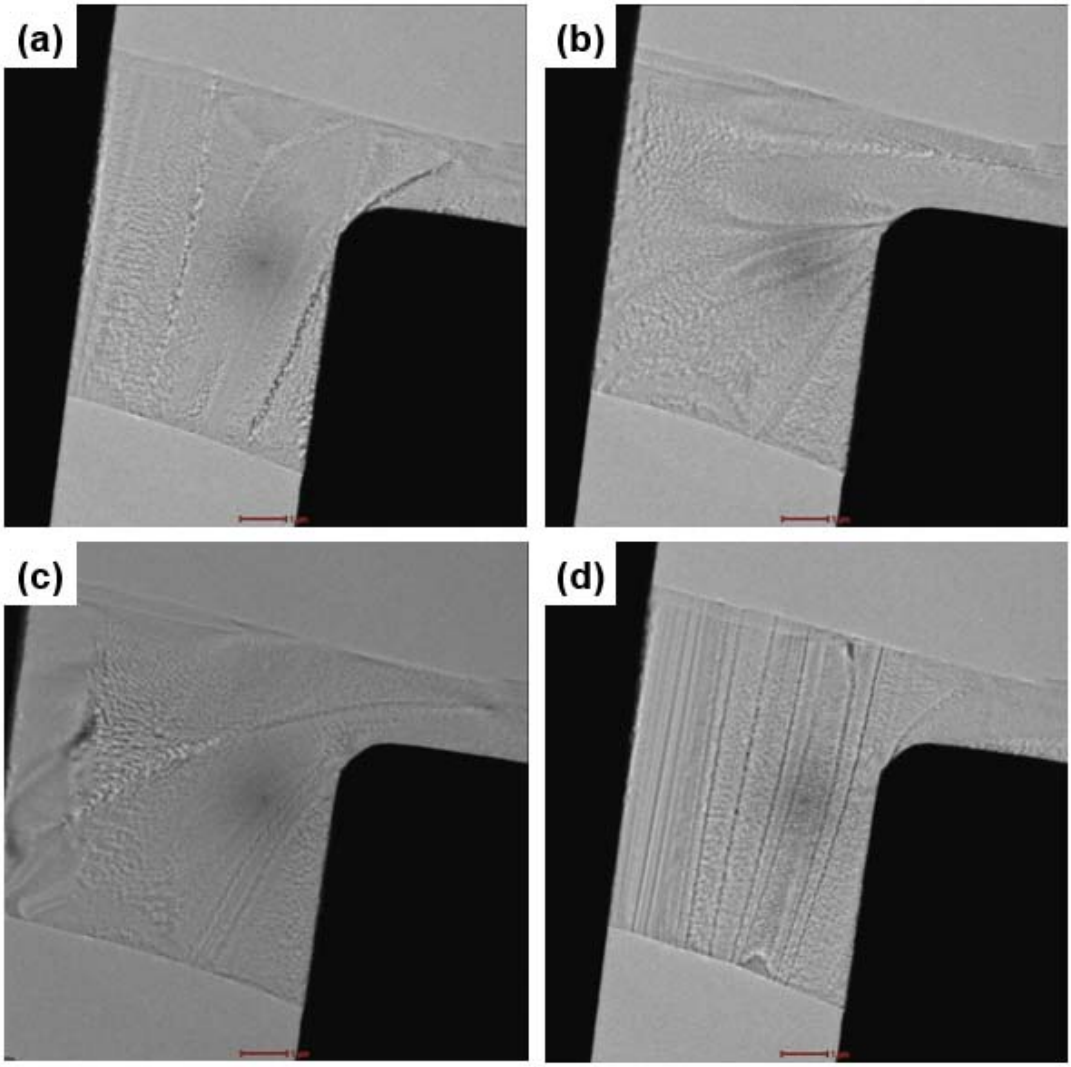

Figure 40. (a-d) Three steps to create bending shape of MoS_2. Flatten, sliding and bending process occurred in TEM images. In Figure 40(c), it is possible to confirm that the surface which was not exposed due to sliding is visible.

We deliberately utilized tensile test along the zigzag direction to form bending shape in MoS_2, and structural characterization can be confirmed as shown in Figure 41(a). There were wrinkles parallel to the direction of the armchair. Several distorted areas between the wrinkles were also formed. Figure 41(b) shows that crumpled structure has lattice distortion. In the bending state, the crumpled area was wide and it can be also observed that the crumpled structures were very unstable in the irradiation of the electron beam. The Pt strips deposited to prevent sliding of MoS_2 on the PTP device through FIB. When the tensile test was carried out in fixed state, mechanical properties for brittle material appeared as shown in Figure 41(c). Figure 41(d) shows the structure of the fractured edges as an HRTEM image. As mentioned above, since the difference in edge energy between armchair and zigzag is not large, the armchair edge is dominant for the uniaxial tensile test along the zigzag direction of our experimental condition. The results of the mechanical properties for the bending structure can be compared with the previously results to confirm the lowered values. This is considered to be due to deterioration from the crumpled structures. The results of strain mapping are Figure 41(e) and (f)d. These mechanical weaknesses can be confirmed experimentally as the repetitive uniaxial tensile test conducted as shown in Figure 42.

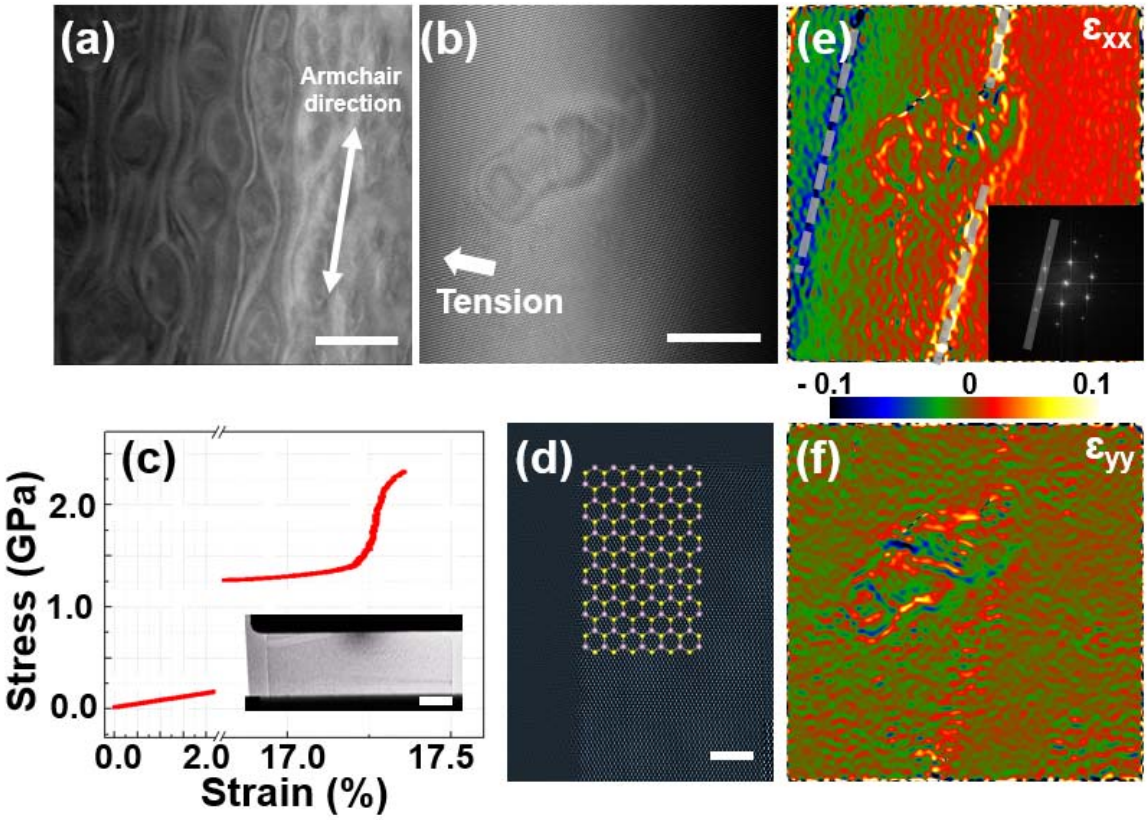

Figure 41. (a) TEM image into the bending MoS_2. Scale bar is 200 nm. (b) HRTEM image for wrinkles and locally distorted structure. Scale bar is 10 nm. (c) Stress-strain result for bending MoS_2. Brittle fracture occurred in strain 17.2 ~ 17.3 %. Inset is the TEM image of the fracture MoS_2 after tensile test. Scale bar is 2 μm. (d) HRTEM image of the edge of fractured MoS_2. Scale bar is 5 nm. (e-f) Strain mapping results for (b) through GPA method. These resulting image is taken from (b).

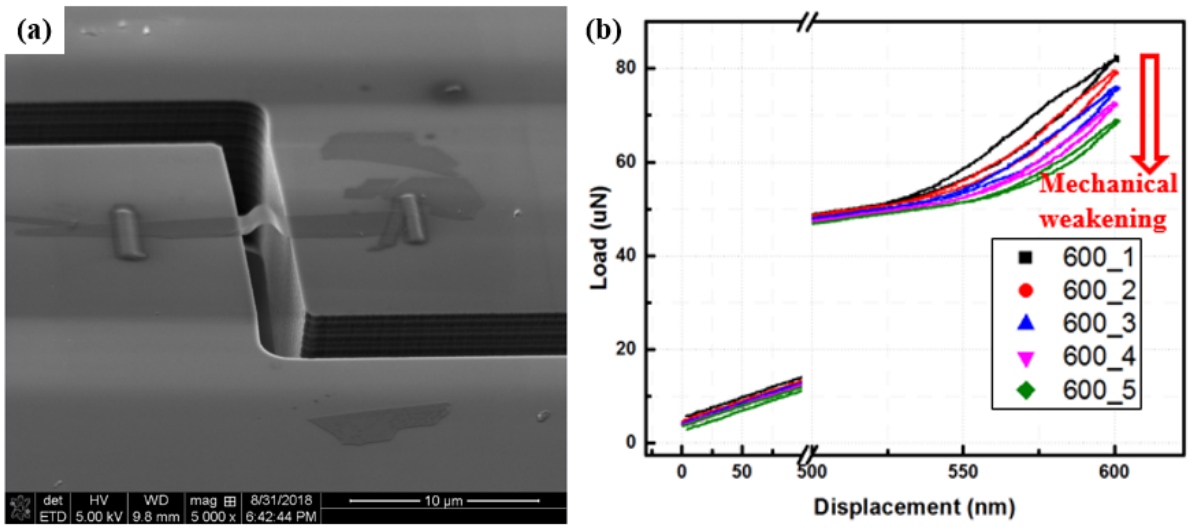

Figure 42. (a) SEM image of bending MoS_2 for Repetitive uniaxial testing. Controlled displacement is 600 nm. (b) The result of load-displacement for repetitive uniaxial testing. Mechanical weakening is observed as the tensile testing conducted continuously.

5.4. Conclusion

2D materials were successfully transferred to a PTP MEMS device for in situ TEM tensile testing. The gel material used for transfer was liquefied and penetrated under the exfoliated graphene. Through results of optical imaging, Raman spectroscopy, and HRTEM imaging, we confirmed that the gel material did not affect the mechanical properties of the exfoliated graphene. Finally, we conducted in situ TEM uniaxial tensile testing, which revealed crack propagation from the folded area in experiments where the S–S curve was obtained simultaneously. Values for the Young's modulus and maximum stress were also obtained from the S–S curve, and the results were compared with previously reported results. We expect that our technique will lead to enhanced understanding of the mechanical behavior of 2D materials at the atomic level. Furthermore, because the displacement for sliding in PTP device can be controlled, the bending shape was deliberately formed in MoS_2. The wrinkles and locally distorted structures in bent MoS_2 sheets were unveiled. The quantitative mechanical properties and strain mapping were measured through the experiments. We propose the mechanical properties of two-dimensional materials having the wrinkled and locally distorted structure caused by bending. In this way, we can control the displacement to artificially make the degree of bending of the MoS_2. We have studied the mechanical properties depending on the wrinkled and distorted structure.

Chapter 6. Summary

I conducted the crystallization, growth of thin film and mechanical strength measurements using in situ TEM holders. First, local crystallization of an YSZ thin film in an MIM capacitor was studied using in-situ TEM biasing tests. When a voltage was applied, the currents increased due to the Joule heating in the YSZ thin film. Using a real-time analysis, we observed the crystallization of the YSZ thin film, which could be distinguished in the diffraction contrast in the TEM series images. In addition, the FEM results support that the crystallization with Joule heating occurred in the YSZ thin film when the voltage is applied. Based on the JMAK model, a leakage current occurs due to the influence of the grain boundaries caused by crystallization from the surface. This has the effect of forming defect charge states in the bandgap and rises the possibility of trap-assisted tunneling and P–F conduction. We demonstrated the relationship between the crystallinity and the electrical properties of the YSZ thin film in the MIM capacitor. (This research was published in *Nanotechnology* in 2018 and title is "Direct observation of leakage currents in a metal-insulator-metal capacitor using in situ transmission electron microscopy.")

Second, in situ heating TEM conducted to observe hetero epitaxial growth of (001) 3C-SiC on (001) Si NM. 3C-SiC is laterally grown and has the <110> direction on the Si NM. In addition, the growth of 3C-SiC at much lower temperature than the expected temperature in bulk state occurred. It is demonstrated by experiments and calculations resulting of a process in environment of high vacuum. We supposed that the lattice mismatch between the Si NM and 3C-SiC caused bending from initial growth. The bending resulted in large area hetero epitaxial growth of 3C-SiC without defects. We show the possibilities for other heteroepitaxial growth materials like our case in in situ heating TEM.

Finally, 2D materials were successfully transferred to a PTP MEMS device for in situ TEM tensile testing. The gel material used for transfer was liquefied and penetrated under the exfoliated graphene. Through results of optical imaging, Raman spectroscopy, and HRTEM imaging, we confirmed that the gel material did not affect the mechanical properties of the exfoliated graphene. Finally, we conducted in situ TEM uniaxial tensile testing, which revealed crack propagation from the folded area in experiments where the S–S curve was obtained simultaneously. Values for the Young's modulus and maximum stress were also obtained from the S–S curve, and the results were compared with previously reported results. We expect that our technique will lead to enhanced understanding of the mechanical behavior of 2D materials at the atomic level. Furthermore, because the displacement for sliding in PTP device can be controlled, the bending shape was deliberately formed in MoS_2. The wrinkles and locally distorted structures in bent MoS_2 sheets were unveiled. The quantitative mechanical properties and strain mapping were measured through the experiments. We propose the mechanical properties of two-dimensional materials having the wrinkled and locally distorted structure caused by bending. In this way, we can control the displacement to artificially make the degree of bending of the MoS_2. We have studied the mechanical properties depending on the wrinkled and distorted structure.

References

[1] K. Jungjohann and C. Carter, "Transmission Electron Microscopy: Diffraction Imaging and Spectrometry," ed: Springer International Publishing, 2016, p. 518.

[2] C. R. Winkler, A. R. Damodaran, J. Karthik, L. W. Martin, and M. L. Taheri, "Direct observation of ferroelectric domain switching in varying electric field regimes using in situ TEM," *Micron,* vol. 43, no. 11, pp. 1121-1126, Nov 2012.

[3] Z. Y. Wang *et al.*, "In Situ STEM-EELS Observation of Nanoscale Interfacial Phenomena in All-Solid-State Batteries," *Nano Letters,* vol. 16, no. 6, pp. 3760-3767, Jun 2016.

[4] K. Pey, R. Thamankar, M. Sen, M. Bosman, N. Raghavan, and K. Shubhakar, "Understanding the switching mechanism in RRAM using in-situ TEM," in *Silicon Nanoelectronics Workshop (SNW), 2016 IEEE*, 2016, pp. 36-37: IEEE.

[5] S. Sohn, Y. Jung, Y. J. Xie, C. Osuji, J. Schroers, and J. J. Cha, "Nanoscale size effects in crystallization of metallic glass nanorods," *Nature Communications,* vol. 6, Sep 2015.

[6] Y. L. Shen, "Local Joule heating and overall resistance increase in void-containing aluminum interconnects," *Journal of Electronic Materials,* vol. 30, no. 4, pp. 367-371, Apr 2001.

[7] W. E. Hong and J. S. Ro, "Polycrystalline silicon thin-film transistors fabricated by Joule-heating-induced crystallization," *Solid-State Electronics,* vol. 103, pp. 178-183, Jan 2015.

[8] W. E. Hong and J. S. Ro, "Millisecond crystallization of amorphous silicon films by Joule-heating induced crystallization using a conductive layer," *Thin Solid Films,* vol. 515, no. 13, pp. 5357-5361, May 7 2007.

[9] S. Helveg *et al.*, "Atomic-scale imaging of carbon nanofibre growth," *Nature,* vol. 427, no. 6973, pp. 426-429, Jan 29 2004.

[10] H. K. Hong *et al.*, "Atomic Scale Study on Growth and Heteroepitaxy of ZnO Monolayer on Graphene," *Nano Letters,* vol. 17, no. 1, pp. 120-127, Jan 2017.

[11] C. Lee, X. D. Wei, J. W. Kysar, and J. Hone, "Measurement of the elastic properties and intrinsic strength of monolayer graphene," *Science,* vol. 321, no. 5887, pp. 385-388, Jul 18 2008.

[12] S. Bertolazzi, J. Brivio, and A. Kis, "Stretching and Breaking of Ultrathin MoS2," *Acs Nano,* vol. 5, no. 12, pp. 9703-9709, Dec 2011.

[13] J. Han, N. M. Pugno, and S. Ryu, "Nanoindentation cannot accurately predict the tensile strength of graphene or other 2D materials," *Nanoscale,* vol. 7, no. 38, pp. 15672-15679, 2015.

[14] S. Meister, D. T. Schoen, M. A. Topinka, A. M. Minor, and Y. Cui, "Void Formation Induced Electrical Switching in Phase-Change Nanowires," *Nano Letters,* vol. 8, no. 12, pp. 4562-4567, Dec 2008.

[15] L. F. Allard, S. H. Overbury, W. C. Bigelow, M. B. Katz, D. P. Nackashi, and J. Damiano, "Novel MEMS-Based Gas-Cell/Heating Specimen Holder Provides Advanced Imaging Capabilities for In Situ Reaction Studies," *Microscopy and Microanalysis,* vol. 18, no. 4, pp. 656-666, Aug 2012.

[16] K. Kim, J. H. Kim, B. E. Park, H. Kim, and Z. Lee, "Direct observation of leakage currents in a

metal-insulator-metal capacitor using in situ transmission electron microscopy," *Nanotechnology,* vol. 29, no. 43, Oct 26 2018.

[17] S. Sinha *et al.*, "In Situ Atomic-Level Studies of Gd Atom Release and Migration on Graphene from a Metallofullerene Precursor," *Acs Nano,* vol. 12, no. 10, pp. 10439-10451, Oct 2018.

[18] W. J. Qi, R. Nieh, B. H. Lee, L. G. Kang, Y. Jeon, and J. C. Lee, "Electrical and reliability characteristics of ZrO2 deposited directly on Si for gate dielectric application," *Applied Physics Letters,* vol. 77, no. 20, pp. 3269-3271, Nov 13 2000.

[19] Y. H. Wu, C. C. Lin, L. L. Chen, Y. C. Hu, J. R. Wu, and M. L. Wu, "High-performance metal-insulator-metal capacitor with Ge-stabilized tetragonal ZrO2/amorphous La-doped ZrO2 dielectric," *Applied Physics Letters,* vol. 98, no. 1, Jan 3 2011.

[20] Y. J. Huang, Y. Huang, S. J. Ding, W. Zhang, and L. Ran, "Electrical characterization of metal-insulator-metal capacitors with atomic-layer-deposited HfO2 dielectrics for radio frequency integrated circuit application," *Chinese Physics Letters,* vol. 24, no. 10, pp. 2942-2944, Oct 2007.

[21] F. C. Chiu, "A Review on Conduction Mechanisms in Dielectric Films," *Advances in Materials Science and Engineering,* 2014.

[22] S. Heiroth *et al.*, "Yttria-stabilized zirconia thin films by pulsed laser deposition: Microstructural and compositional control," *Journal of the European Ceramic Society,* vol. 30, no. 2, pp. 489-495, Jan 2010.

[23] S. Heiroth *et al.*, "Crystallization and grain growth characteristics of yttria-stabilized zirconia thin films grown by pulsed laser deposition," *Solid State Ionics,* vol. 191, no. 1, pp. 12-23, Jun 2 2011.

[24] B. E. Park *et al.*, "Atomic layer deposition of Y-stabilized ZrO2 for advanced DRAM capacitors," *Journal of Alloys and Compounds,* vol. 722, pp. 307-312, Oct 25 2017.

[25] K. Baek *et al.*, "Microstructure-dependent DC set switching behaviors of Ge-Sb-Te-based phase-change random access memory devices accessed by in situ TEM," *Npg Asia Materials,* vol. 7, Jun 2015.

[26] K. J. Chen, F. Y. Hung, T. S. Lui, S. J. Chang, and Z. S. Hu, "The Low-Temperature Crystallization and Interface Characteristics of ZnInSnO/In Films Using a Bias-Crystallization Mechanism," *Journal of Nanomaterials,* 2012.

[27] J. H. Jeong *et al.*, "Current induced polycrystallineto-crystalline transformation in vanadium dioxide nanowires," *Scientific Reports,* vol. 6, Nov 28 2016.

[28] C. T. Nelson *et al.*, "Domain Dynamics During Ferroelectric Switching," *Science,* vol. 334, no. 6058, pp. 968-971, Nov 18 2011.

[29] J. P. Oviedo *et al.*, "In Situ TEM Characterization of Shear-Stress-Induced Interlayer Sliding in the Cross Section View of Molybdenum Disulfide," *Acs Nano,* vol. 9, no. 2, pp. 1543-1551, Feb 2015.

[30] S. Saha and S. B. Krupanidhi, "Impact of microstructure on the electrical stress induced effects of pulsed laser ablated (Ba, Sr)TiO3 thin films," *Journal of Applied Physics,* vol. 87,

no. 6, pp. 3056-3062, Mar 15 2000.

[31] E. Harari, "Dielectric-Breakdown in Electrically Stressed Thin-Films of Thermal Sio2," *Journal of Applied Physics,* vol. 49, no. 4, pp. 2478-2489, 1978.

[32] S. Lombardo, J. H. Stathis, B. P. Linder, K. L. Pey, F. Palumbo, and C. H. Tung, "Dielectric breakdown mechanisms in gate oxides," *Journal of Applied Physics,* vol. 98, no. 12, Dec 15 2005.

[33] G. Beck *et al.*, "Epitaxial Pt(111) thin film electrodes on YSZ(111) and YSZ(100) - Preparation and characterisation," *Solid State Ionics,* vol. 178, no. 5-6, pp. 327-337, Mar 2007.

[34] S. J. Jun, Y. S. Kim, J. Lee, and Y. W. Kim, "Dielectric properties of strained (Ba, Sr)TiO3 thin films epitaxially grown on Si with thin yttria-stabilized zirconia buffer layer," *Applied Physics Letters,* vol. 78, no. 17, pp. 2542-2544, Apr 23 2001.

[35] D. H. Kim, F. Merget, M. Forst, and H. Kurz, "Three-dimensional simulation model of switching dynamics in phase change random access memory cells," *Journal of Applied Physics,* vol. 101, no. 6, Mar 15 2007.

[36] K. W. Schlichting, N. P. Padture, and P. G. Klemens, "Thermal conductivity of dense and porous yttria-stabilized zirconia," *Journal of Materials Science,* vol. 36, no. 12, pp. 3003-3010, 2001.

[37] X. J. Chou, J. W. Zhai, H. T. Jiang, and X. Yao, "Dielectric properties and relaxor behavior of rare-earth (La, Sm, Eu, Dy, Y) substituted barium zirconium titanate ceramics," *Journal of Applied Physics,* vol. 102, no. 8, Oct 15 2007.

[38] P. K. Schelling, S. R. Phillpot, and D. Wolf, "Mechanism of the cubic-to-tetragonal phase transition in zirconia and yttria-stabilized zirconia by molecular-dynamics simulation," *Journal of the American Ceramic Society,* vol. 84, no. 7, pp. 1609-1619, Jul 2001.

[39] D. Molnar, C. Niedermeier, A. Mora, P. Binkele, and S. Schmauder, "Activation energies for nucleation and growth and critical cluster size dependence in JMAK analyses of kinetic Monte-Carlo simulations of precipitation," *Continuum Mechanics and Thermodynamics,* vol. 24, no. 4-6, pp. 607-617, Nov 2012.

[40] L. Mooij and B. Dam, "Nucleation and growth mechanisms of nano magnesium hydride from the hydrogen sorption kinetics," *Physical Chemistry Chemical Physics,* vol. 15, no. 27, pp. 11501-11510, 2013.

[41] A. Infortuna, A. S. Harvey, and L. J. Gauckler, "Microstructures of CGO and YSZ thin films by pulsed laser deposition," *Advanced Functional Materials,* vol. 18, no. 1, pp. 127-135, Jan 11 2008.

[42] S. Ji, G. Y. Cho, W. Yu, P. C. Su, M. H. Lee, and S. W. Cha, "Plasma-Enhanced Atomic Layer Deposition of Nanoscale Yttria-Stabilized Zirconia Electrolyte for Solid Oxide Fuel Cells with Porous Substrate (vol 7, pg 2998, 2015)," *Acs Applied Materials & Interfaces,* vol. 7, no. 25, pp. 14163-14163, Jul 1 2015.

[43] A. A. Solovyev, A. V. Shipilova, I. V. Ionov, A. N. Kovalchuk, S. V. Rabotkin, and V. O. Oskirko, "Magnetron-Sputtered YSZ and CGO Electrolytes for SOFC," *Journal of Electronic Materials,*

vol. 45, no. 8, pp. 3921-3928, Aug 2016.

[44] I. N. Vol'nov, "The use of Kolmogorov's kinetic equation for the description of crystallization of alloys," *Metal Science and Heat Treatment,* vol. 42, no. 5-6, pp. 207-210, May-Jun 2000.

[45] C. W. Price, "Use of Kolmogorov-Johnson-Mehl-Avrami Kinetics in Recrystallization of Metals and Crystallization of Metallic Glasses," *Acta Metallurgica Et Materialia,* vol. 38, no. 5, pp. 727-738, May 1990.

[46] A. E. Hughes, "Segregation in Single-Crystal Fully Stabilized Yttria-Zirconia," *Journal of the American Ceramic Society,* vol. 78, no. 2, pp. 369-378, Feb 1995.

[47] K. M. Subramaniam, L. L. R. Rao, and N. Jampana, "Investigation of Annealing Induced Yttria Segregation in Sputtered Yttria-Stabilized Zirconia Thin Films," *Journal of the American Ceramic Society,* vol. 98, no. 10, pp. 3389-3397, Oct 2015.

[48] A. Bernasik, K. Kowalski, and A. Sadowski, "Surface segregation in yttria-stabilized zirconia by means of angle resolved X-ray photoelectron spectroscopy," *Journal of Physics and Chemistry of Solids,* vol. 63, no. 2, pp. 233-239, Feb 2002.

[49] Z. Suo, "Models for Breakdown-Resistant Dielectric and Ferroelectric Ceramics," *Journal of the Mechanics and Physics of Solids,* vol. 41, no. 7, pp. 1155-1176, Jul 1993.

[50] M. Bhatnagar and B. J. Baliga, "Comparison of 6h-Sic, 3c-Sic, and Si for Power Devices," *Ieee Transactions on Electron Devices,* vol. 40, no. 3, pp. 645-655, Mar 1993.

[51] H. Morkoc, S. Strite, G. B. Gao, M. E. Lin, B. Sverdlov, and M. Burns, "Large-Band-Gap Sic, Iii-V Nitride, and Ii-Vi Znse-Based Semiconductor-Device Technologies," *Journal of Applied Physics,* vol. 76, no. 3, pp. 1363-1398, Aug 1 1994.

[52] M. Ghezzo *et al.*, "Nitrogen-Implanted Sic Diodes Using High-Temperature Implantation," *Ieee Electron Device Letters,* vol. 13, no. 12, pp. 639-641, Dec 1992.

[53] R. J. Trew, J. B. Yan, and P. M. Mock, "The Potential of Diamond and Sic Electronic Devices for Microwave and Millimeter-Wave Power Applications," *Proceedings of the Ieee,* vol. 79, no. 5, pp. 598-620, May 1991.

[54] S. Rohmfeld, M. Hundhausen, L. Ley, C. A. Zorman, and M. Mehregany, "Quantitative evaluation of biaxial strain in epitaxial 3 C-SiC layers on Si(100) substrates by Raman spectroscopy," *Journal of Applied Physics,* vol. 91, no. 3, pp. 1113-1117, Feb 1 2002.

[55] Z. C. Feng, A. J. Mascarenhas, W. J. Choyke, and J. A. Powell, "Raman-Scattering Studies of Chemical-Vapor-Deposited Cubic Sic Films of (100) Si," *Journal of Applied Physics,* vol. 64, no. 6, pp. 3176-3186, Sep 15 1988.

[56] T. Yoshinobu, H. Mitsui, Y. Tarui, T. Fuyuki, and H. Matsunami, "Heteroepitaxial Growth of Single Crystalline 3c-Sic on Si Substrates by Gas Source Molecular-Beam Epitaxy," *Journal of Applied Physics,* vol. 72, no. 5, pp. 2006-2013, Sep 1 1992.

[57] Q. Wahab, L. Hultman, I. P. Ivanov, M. Willander, and J. E. Sundgren, "Growth and Characterization of 3c-Sic Films on Si Substrates by Reactive Magnetron Sputtering - Effects of Ch4 Partial-Pressure on the Crystalline Quality, Structure and Stoichiometry," *Thin Solid Films,* vol. 261, no. 1-2, pp. 317-321, Jun 1 1995.

[58] V. Jokubavicius *et al.*, "Single Domain 3C-SiC Growth on Off-Oriented 4H-SiC Substrates," *Crystal Growth & Design,* vol. 15, no. 6, pp. 2940-2947, Jun 2015.

[59] T. Chassagne *et al.*, "Control of 3C-SiC/Si wafer bending by the "checker-board" carbonization method," *Physica Status Solidi a-Applications and Materials Science,* vol. 202, no. 4, pp. 524-530, Mar 2005.

[60] H. Nagasawa and K. Yagi, "3C-SiC single-crystal films grown on 6-inch Si substrates," *Physica Status Solidi B-Basic Research,* vol. 202, no. 1, pp. 335-358, Jul 1997.

[61] W. C. Lien, N. Ferralis, C. Carraro, and R. Maboudian, "Growth of Epitaxial 3C-SiC Films on Si(100) via Low Temperature SiC Buffer Layer," *Crystal Growth & Design,* vol. 10, no. 1, pp. 36-39, Jan 2010.

[62] B. E. Deal and A. S. Grove, "General Relationship for Thermal Oxidation of Silicon," *Journal of Applied Physics,* vol. 36, no. 12, pp. 3770-&, 1965.

[63] P. E. Batson, "Simultaneous Stem Imaging and Electron-Energy-Loss Spectroscopy with Atomic-Column Sensitivity," *Nature,* vol. 366, no. 6457, pp. 727-728, Dec 23 1993.

[64] N. Bonnet, N. Brun, and C. Colliex, "Extracting information from sequences of spatially resolved EELS spectra using multivariate statistical analysis," *Ultramicroscopy,* vol. 77, no. 3-4, pp. 97-112, Jul 1999.

[65] W. Windl, T. Liang, S. Lopatin, and G. Duscher, "Modeling and characterization of atomically sharp "perfect" Ge/SiO2 interfaces," *Materials Science and Engineering B-Solid State Materials for Advanced Technology,* vol. 114, pp. 156-161, Dec 15 2004.

[66] D. M. Knotter, "Etching mechanism of vitreous silicon dioxide in HF-based solutions," *Journal of the American Chemical Society,* vol. 122, no. 18, pp. 4345-4351, May 10 2000.

[67] M. Abdullah, S. Khairunnisa, and F. Akbar, "Zipper model for the melting of thin films," *European Journal of Physics,* vol. 37, no. 1, Jan 2016.

[68] G. L. Allen, R. A. Bayles, W. W. Gile, and W. A. Jesser, "Small Particle Melting of Pure Metals," *Thin Solid Films,* vol. 144, no. 2, pp. 297-308, Nov 15 1986.

[69] S. L. Lai, J. Y. Guo, V. Petrova, G. Ramanath, and L. H. Allen, "Size-dependent melting properties of small tin particles: Nanocalorimetric measurements," *Physical Review Letters,* vol. 77, no. 1, pp. 99-102, Jul 1 1996.

[70] K. K. Nanda, S. N. Sahu, and S. N. Behera, "Liquid-drop model for the size-dependent melting of low-dimensional systems," *Physical Review A,* vol. 66, no. 1, Jul 2002.

[71] V. Malyshev, N. Bekturganov, A. Turdukozhayeva, M. Z. Tolymbekov, and S. Kim, "Evaporation of silicon as the basis for its sublimation purification," in *The thirteenth international ferroalloys congress*, 2013.

[72] H. Antes Jr, "Critical Melting Points and Reference Data for Vacuum Heat Treating," 2010.

[73] T. Buonassisi, A. A. Istratov, M. D. Pickett, M. A. Marcus, T. F. Ciszek, and E. R. Weber, "Metal precipitation at grain boundaries in silicon: Dependence on grain boundary character and dislocation decoration," *Applied Physics Letters,* vol. 89, no. 4, Jul 24 2006.

[74] T. Buonassisi *et al.*, "Transition metal co-precipitation mechanisms in silicon," *Acta Materialia,*

vol. 55, no. 18, pp. 6119-6126, Oct 2007.

[75] B. Chen, J. Chen, T. Sekiguchi, M. Saito, and K. Kimoto, "Structural characterization and iron detection at Sigma 3 grain boundaries in multicrystalline silicon," *Journal of Applied Physics,* vol. 105, no. 11, Jun 1 2009.

[76] A. Bakenfelder, I. Fromm, L. Reimer, and R. Rennekamp, "Contrast in the Electron Spectroscopic Imaging Mode of a Tem .3. Bragg Contrast of Crystalline Specimens," *Journal of Microscopy-Oxford,* vol. 159, pp. 161-177, Aug 1990.

[77] G. F. Schneider *et al.*, "DNA Translocation through Graphene Nanopores," *Nano Letters,* vol. 10, no. 8, pp. 3163-3167, Aug 2010.

[78] S. Garaj, W. Hubbard, A. Reina, J. Kong, D. Branton, and J. A. Golovchenko, "Graphene as a subnanometre trans-electrode membrane," *Nature,* vol. 467, no. 7312, pp. 190-U73, Sep 9 2010.

[79] S. Garaj, S. Liu, J. A. Golovchenko, and D. Branton, "Molecule-hugging graphene nanopores," *Proceedings of the National Academy of Sciences of the United States of America,* vol. 110, no. 30, pp. 12192-12196, Jul 23 2013.

[80] K. S. Novoselov *et al.*, "Electric field effect in atomically thin carbon films," *science,* vol. 306, no. 5696, pp. 666-669, 2004.

[81] A. K. Geim and K. S. Novoselov, "The rise of graphene," *Nature Materials,* vol. 6, no. 3, pp. 183-191, Mar 2007.

[82] Y. B. Zhang, Y. W. Tan, H. L. Stormer, and P. Kim, "Experimental observation of the quantum Hall effect and Berry's phase in graphene," *Nature,* vol. 438, no. 7065, pp. 201-204, Nov 10 2005.

[83] K. S. Novoselov *et al.*, "Two-dimensional gas of massless Dirac fermions in graphene," *Nature,* vol. 438, no. 7065, pp. 197-200, Nov 10 2005.

[84] N. A. Kyerematen, T. Brousse, and D. Pech, "Microsupercapacitors as miniaturized energy-storage components for on-chip electronics," *Nature Nanotechnology,* vol. 12, no. 1, pp. 7-15, Jan 2017.

[85] M. F. El-Kady and R. B. Kaner, "Scalable fabrication of high-power graphene micro-supercapacitors for flexible and on-chip energy storage," *Nature Communications,* vol. 4, Feb 2013.

[86] H. Chen, M. B. Muller, K. J. Gilmore, G. G. Wallace, and D. Li, "Mechanically strong, electrically conductive, and biocompatible graphene paper," *Advanced Materials,* vol. 20, no. 18, pp. 3557-+, Sep 17 2008.

[87] X. Zhao, Q. H. Zhang, D. J. Chen, and P. Lu, "Enhanced Mechanical Properties of Graphene-Based Poly(vinyl alcohol) Composites," *Macromolecules,* vol. 43, no. 5, pp. 2357-2363, Mar 9 2010.

[88] M. A. Rafiee, J. Rafiee, Z. Wang, H. H. Song, Z. Z. Yu, and N. Koratkar, "Enhanced Mechanical Properties of Nanocomposites at Low Graphene Content," *Acs Nano,* vol. 3, no. 12, pp. 3884-3890, Dec 2009.

[89] F. Liu, P. M. Ming, and J. Li, "Ab initio calculation of ideal strength and phonon instability of graphene under tension," *Physical Review B,* vol. 76, no. 6, Aug 2007.

[90] Q. X. Pei, Y. W. Zhang, and V. B. Shenoy, "A molecular dynamics study of the mechanical properties of hydrogen functionalized graphene," *Carbon,* vol. 48, no. 3, pp. 898-904, Mar 2010.

[91] G. H. Lee *et al.*, "High-Strength Chemical-Vapor Deposited Graphene and Grain Boundaries," *Science,* vol. 340, no. 6136, pp. 1073-1076, May 31 2013.

[92] B. Mortazavi and G. Cuniberti, "Atomistic modeling of mechanical properties of polycrystalline graphene," *Nanotechnology,* vol. 25, no. 21, May 30 2014.

[93] C. Gammer, J. Kacher, C. Czarnik, O. L. Warren, J. Ciston, and A. M. Minor, "Local and transient nanoscale strain mapping during in situ deformation," *Applied Physics Letters,* vol. 109, no. 8, Aug 22 2016.

[94] X. G. Wang *et al.*, "Growth Conditions Control the Elastic and Electrical Properties of ZnO Nanowires," *Nano Letters,* vol. 15, no. 12, pp. 7886-7892, Dec 2015.

[95] A. E. Mag-isa, J. H. Kim, H. J. Lee, and C. S. Oh, "A systematic exfoliation technique for isolating large and pristine samples of 2D materials," *2d Materials,* vol. 2, no. 3, Sep 2015.

[96] Y. Oh, E. Cyrankowski, Z. Shan, and S. A. S. Asif, "Micro/nano-mechanical test system employing tensile test holder with push-to-pull transformer," ed: Google Patents, 2013.

[97] H. Li *et al.*, "Rapid and Reliable Thickness Identification of Two-Dimensional Nanosheets Using Optical Microscopy," *Acs Nano,* vol. 7, no. 11, pp. 10344-10353, Nov 2013.

[98] F. Pizzocchero *et al.*, "The hot pick-up technique for batch assembly of van der Waals heterostructures," *Nature Communications,* vol. 7, Jun 2016.

[99] H. Y. Nan, Z. H. Ni, J. Wang, Z. Zafar, Z. X. Shi, and Y. Y. Wang, "The thermal stability of graphene in air investigated by Raman spectroscopy," *Journal of Raman Spectroscopy,* vol. 44, no. 7, pp. 1018-1021, Jul 2013.

[100] P. Venezuela, M. Lazzeri, and F. Mauri, "Theory of double-resonant Raman spectra in graphene: Intensity and line shape of defect-induced and two-phonon bands," *Physical Review B,* vol. 84, no. 3, Jul 25 2011.

[101] M. M. Lucchese *et al.*, "Quantifying ion-induced defects and Raman relaxation length in graphene," *Carbon,* vol. 48, no. 5, pp. 1592-1597, Apr 2010.

[102] L. G. Cancado *et al.*, "Quantifying Defects in Graphene via Raman Spectroscopy at Different Excitation Energies," *Nano Letters,* vol. 11, no. 8, pp. 3190-3196, Aug 2011.

[103] L. Y. Chen, M. R. He, J. Shin, G. Richter, and D. S. Gianola, "Measuring surface dislocation nucleation in defect-scarce nanostructures," *Nature Materials,* vol. 14, no. 7, pp. 707-+, Jul 2015.

[104] K. Kim *et al.*, "Multiply folded graphene," *Physical Review B,* vol. 83, no. 24, Jun 27 2011.

[105] X. M. Chen, L. Y. Zhang, Y. D. Zhao, X. Q. Wang, and C. H. Ke, "Graphene folding on flat substrates," *Journal of Applied Physics,* vol. 116, no. 16, Oct 28 2014.

[106] J. C. Meyer *et al.*, "Experimental analysis of charge redistribution due to chemical bonding

by high-resolution transmission electron microscopy," *Nature Materials,* vol. 10, no. 3, pp. 209-215, Mar 2011.

[107] P. Zhang *et al.*, "Fracture toughness of graphene," *Nature Communications,* vol. 5, Apr 2014.

[108] J. Annett and G. L. W. Cross, "Self-assembly of graphene ribbons by spontaneous self-tearing and peeling from a substrate," *Nature,* vol. 535, no. 7611, pp. 271-+, Jul 14 2016.

[109] K. Kim *et al.*, "Ripping Graphene: Preferred Directions," *Nano Letters,* vol. 12, no. 1, pp. 293-297, Jan 2012.

[110] X. Z. Ma *et al.*, "Capillary-Force-Assisted Clean-Stamp Transfer of Two-Dimensional Materials," *Nano Letters,* vol. 17, no. 11, pp. 6961-6967, Nov 2017.

[111] M. Tinoco, L. Maduro, M. Masaki, E. Okunishi, and S. Conesa-Boj, "Strain-Dependent Edge Structures in MoS2 Layers," *Nano Letters,* vol. 17, no. 11, pp. 7021-7026, Nov 2017.